Spin-Orbit Torque and Field-Free Magnetization Switching by Topological Insulators

Che, Xiaoyu

2020

UNIVERSITY OF CALIFORNIA

Los Angeles

Spin-Orbit Torque and Field-Free Magnetization Switching by Topological Insulators

A dissertation submitted in partial satisfaction of the
requirements for the degree Doctor of Philosophy in
Electrical Engineering

by

Xiaoyu Che

2020

ABSTRACT OF THE DISSERTATION

Spin-Orbit Torque and Field-Free Magnetization Switching by Topological Insulators

by

Xiaoyu Che

Doctor of Philosophy in Electrical Engineering

University of California, Los Angeles, 2020

Professor Kang Lung Wang, Chair

Spin accumulation originating from relativistic spin-orbit interaction can exert spin-orbit torque (SOT) on adjacent magnetization and switch the direction of the magnetization. Such current-driven magnetization switching holds promise for miniaturized magnetic memory devices with high speed, low power consumption, and non-volatility. One of the promising material candidates is topological insulator (TI). TI is a novel quantum state of matter with gapped bulk bands and gapless surface states protected by topology. The spin and momentum of the carriers from the surface states are locked, and the spin-momentum locked carriers can drive giant SOT on neighboring magnetization. However, there are still several issues in the study of SOT from TIs. First, there have been large discrepancies in the reported values of SOT from TIs. Second, the magnetization switching by TIs requires the assistance of an external magnetic field, which results in limited applicability.

In this dissertation, I systematically investigate magnetically doped TI thin films and determine the SOT via both transport and optic approaches, collaborating with other group members. Large SOT generated by the topological surface states with consistent results is observed. The experimental results reveal a strong dependence of SOT on temperature and surface state carrier concentration. The SOT decreases drastically as temperature increases and can be manipulated by tuning the surface state carrier concentration. A competition between the top surface and bottom surface in contributing to SOT is also observed. The above phenomena could account for the large discrepancies in the reported SOT values. Utilizing the SOT from surface states, I am able to achieve current-driven magnetization switching in magnetically doped TIs. I also investigate TI/antiferromagnetic material heterostructures and demonstrate the realization of field-free magnetization switching in this material system. Accomplished by symmetry breaking with interfacial exchange-bias, the field-free switching can be driven by pulsed current with ultra-low current density. The study in this dissertation advances the understanding of SOT from TI as well as the implementation of practical and energy-efficient magnetic random-access memory.

The dissertation of Xiaoyu Che is approved.

Chee Wei Wong

Benjamin S. Williams

Gregory P. Carman

Kang Lung Wang, Committee Chair

University of California, Los Angeles

2020

This dissertation is dedicated to my parents

for their unconditional love and support

TABLE OF CONTENTS

LIST OF FIGURES

ACKNOWLEDGMENTS

It has been an incredibly wonderful journey in Device Research Laboratory at UCLA for the past six years. First of all, I would like to express my gratitude to my advisor, Prof. Kang L. Wang, for his guidance and continuous support throughout my Ph.D. study. Prof. Wang's advice not only sheds light on the path of our research work but also helps our personal development in many aspects. We constantly remind ourselves of his lessons on being creative, bold, and self-disciplined to make breakthroughs. His visionary mind is what every DRL member learns from, and his wisdom will keep offering us lifelong benefits.

I also gratefully acknowledge Prof. Chee Wei Wong, Prof. Benjamin S. Williams, Prof. Gregory P. Carman, and Prof. Ya-Hong Xie for their precious time to serve as my doctoral committee members. Their insightful advice guided me in my Ph.D. study toward a more comprehensive and deeper-level understanding. I also received tremendous help from our collaborators during my Ph.D. work, who supplied fantastic materials and carried out characterization experiments that are essential to the research work in this dissertation. Specifically, I would like to thank Prof. Lei Bi, Prof. Qing-Hui Yang, Prof. Huaiwu Zhang, Dr. Bo Ma at University of Electronic Science and Technology of China and Dr. Junxue Li, Prof. Jing Shi at UC Riverside for the growth of high-quality magnetic insulators, Prof. Xiaodong Han, Dr. Bin Zhang at Beijing University of Technology for capturing fantastic TEM images, Dr. Dongxia Qu at Lawrence Livermore National Lab for optical measurements, and Dr. Alex Grutter at NIST for investigating antiferromagnetic materials using PNR.

While research can be sometimes challenging, I always feel grateful that we have fantastic DRL members working together to tackle problems and supporting each other. I would like to give special thanks to Prof. Faxian Xiu, who served as my advisor in my undergraduate study and also had been an outstanding DRL member, for offering the invaluable opportunity to join the DRL family. I also would like to express my gratitude to Dr. Murong Lang and Prof. Jianshi Tang who passed their cleanroom expertise to me at the very beginning and provided crucial support in my career in seeking industrial positions, and Dr. Lei Pan, Dr. Peng Deng, Mr. Peng Zhang, Prof. Qing Lin He, Dr. Koichi Murata, Mr. Lixuan Tai for the MBE growth of excellent materials, Dr. Yabin Fan, Prof. Qiming Shao, Prof. Guoqiang Yu, Dr. Hao Wu, Yuxiang Liu, Armin Razavi for the wonderful discussions on spintronics topics, Prof. Liang He, Prof. Xufeng Kou, Prof. Gen Yin, Prof. Sidong Lei, Ms. Yingying Wu, Prof. Tianxiao Nie, Dr. Xiang Li, and Dr. Shin-Hung Tsai for sharing precious knowledge of condensed-matters. In addition, I would like to thank our staff members, Eileen Panguito, Wendy Sanchez, and Katie Christensen, who have offered great assistance in administrative supports and logistics.

I would like to give special thanks to the financial support for this work, including the Army Research Office (ARO) Multidisciplinary University Research Initiative (MURI) accomplished under Grant Number W911NF-16-1-0472 and W911NF-15-1-10561, the Spins and Heat in Nanoscale Electronic Systems (SHINES), an Energy Frontier Research Center funded by the US Department of Energy (DOE), Office of Science, Basic Energy Sciences (BES) under award #S000686, the National Science Foundation (DMR-1411085), and the Function Accelerated nanoMaterial Engineering (FAME) Center, one of six centers of STARnet, a Semiconductor Research Corporation (SRC) program sponsored by Microelectronics Advanced Research Corporation (MARCO) and Defense Advanced Research Projects Agency (DARPA).

Last but not least, I would like to express my deepest gratitude to my parents for their unconditional love, encouragement and support.

VITA

Education

2014 – 2017	*M.S.* in Electrical Engineering University of California, Los Angeles
2011 – 2014	*B.S.* in Electrical Engineering (*Summa Cum Laude*) Iowa State University
2009 – 2014	*B.Eng.* in Electrical Engineering University of Electronic Science and Technology of China

Employment

2014 – 2020	Graduate Student Researcher University of California, Los Angeles
2019	RAMP Device Engineer Intern Western Digital

Publications

[1] **X. Che**, Q. Pan, B. Vareskic, J. Zou, L. Pan, P. Zhang, G. Yin, H. Wu, Q. Shao, P. Deng, K. L. Wang, "Strongly Surface State Carrier-Dependent Spin-Orbit Torque in Magnetic Topological Insulators". *Advanced Materials*, e1907661 (2020).

[2] **X. Che**, K. Murata, L. Pan, Q. L. He, G. Yu, Q. Shao, G. Yin, P. Deng, Y. Fan, B. Ma, X. Liang, B. Zhang, X. Han, L. Bi, Q. H. Yang, H. Zhang, K. L. Wang, "Proximity-Induced Magnetic Order in a Transferred Topological Insulator Thin Film on a Magnetic Insulator". *ACS Nano* **12**, 5042-5050 (2018).

[3] **X. Che**, L. Pan, P. Zhang, Q. Pan, H. Wu, B. Zhang, P. Deng, Q. Shao, X. Han, K. L. Wang, " Spin-Orbit Torque and Field-Free Magnetization Switching in Topological Insulator/Antiferromagnet Heterostructures". *Ready for submission.*

[4] Y. Fan, X. Kou, P. Upadhyaya, Q. Shao, L. Pan, M. Lang, **X. Che**, J. Tang, M. Montazeri, K. Murata, L. T. Chang, M. Akyol, G. Yu, T. Nie, K. L. Wong, J. Liu, Y. Wang, Y. Tserkovnyak, K. L. Wang, "Electric-Field Control of Spin-Orbit Torque in a Magnetically Doped Topological Insulator". *Nature Nanotechnology* **11**, 352-359 (2016).

[5] H. Wu, P. Zhang, P. Deng, Q. Lan, Q. Pan, S. A. Razavi, **X. Che**, L. Huang, B. Dai, K. Wong, X. Han, K. L. Wang, "Room-Temperature Spin-Orbit Torque from Topological Surface States". *Physical Review Letters* **123**, 207205 (2019).

[6] Q. M. Shao, H. Wu, Q. J. Pan, P. Zhang, L. Pan, K. Wong, **X. Che**, K. L. Wang, "Room Temperature Highly Efficient Topological Insulator/Mo/CoFeB Spin-Orbit Torque Memory with Perpendicular Magnetic Anisotropy". *2018 IEEE International Electron Devices Meeting (IEDM),* 36.33.31-36.33.34 (2018).

[7] Q. L. He, L. Pan, A. L. Stern, E. C. Burks, **X. Che**, G. Yin, J. Wang, B. Lian, Q. Zhou, E. S. Choi, K. Murata, X. Kou, Z. Chen, T. Nie, Q. Shao, Y. Fan, S. C. Zhang, K. Liu, J. Xia, K. L. Wang, "Chiral Majorana Fermion Modes in a Quantum Anomalous Hall Insulator-Superconductor Structure". *Science* **357**, 294-299 (2017).

[8] Q. L. He, X. Kou, A. J. Grutter, G. Yin, L. Pan, **X. Che**, Y. Liu, T. Nie, B. Zhang, S. M. Disseler, B. J. Kirby, W. Ratcliff Ii, Q. Shao, K. Murata, X. Zhu, G. Yu, Y. Fan, M. Montazeri, X. Han, J. A. Borchers, K. L. Wang, "Tailoring Exchange Couplings in Magnetic

Topological-Insulator/Antiferromagnet Heterostructures". *Nature Materials* **16**, 94-100 (2017).

[9] Q. L. He, G. Yin, A. J. Grutter, L. Pan, **X. Che**, G. Yu, D. A. Gilbert, S. M. Disseler, Y. Liu, P. Shafer, B. Zhang, Y. Wu, B. J. Kirby, E. Arenholz, R. K. Lake, X. Han, K. L. Wang, "Exchange-Biasing Topological Charges by Antiferromagnetism". *Nature Communications* **9**, 2767 (2018).

[10] Q. L. He, G. Yin, L. Yu, A. J. Grutter, L. Pan, C. Z. Chen, **X. Che**, G. Yu, B. Zhang, Q. Shao, A. L. Stern, B. Casas, J. Xia, X. Han, B. J. Kirby, R. K. Lake, K. T. Law, K. L. Wang, "Topological Transitions Induced by Antiferromagnetism in a Thin-Film Topological Insulator". *Physical Review Letters* **121**, 096802 (2018).

[11] Q. Shao, Y. Liu, G. Yu, S. K. Kim, **X. Che**, C. Tang, Q. L. He, Y. Tserkovnyak, J. Shi, K. L. Wang, "Topological Hall Effect at above Room Temperature in Heterostructures Composed of a Magnetic Insulator and a Heavy Metal". *Nature Electronics* **2**, 182-186 (2019).

[12] D. X. Qu, **X. Che**, X. Kou, L. Pan, J. Crowhurst, M. R. Armstrong, J. Dubois, K. L. Wang, G. F. Chapline, "Anomalous Helicity-Dependent Photocurrent in the Topological Insulator $(Bi_{0.5}Sb_{0.5})_2Te_3$ on a GaAs Substrate". *Physical Review B* **97**, (2018).

[13] Q. Shao, A. Grutter, Y. Liu, G. Yu, C.-Y. Yang, D. A. Gilbert, E. Arenholz, P. Shafer, **X. Che**, C. Tang, M. Aldosary, A. Navabi, Q. L. He, B. J. Kirby, J. Shi, K. L. Wang, "Exploring Interfacial Exchange Coupling and Sublattice Effect in Heavy Metal/Ferrimagnetic Insulator Heterostructures Using Hall Measurements, X-ray Magnetic Circular Dichroism, and Neutron Reflectometry". *Physical Review B* **99**, (2019).

[14] Q. M. Shao, G. Q. Yu, L. Pan, **X. Che**, Y. Fan, K. Murata, Q. L. He, T. X. Nie, X. F. Kou, K. L. Wang, "Large Room Temperature Charge-to-Spin Conversion Efficiency in Topological Insulator/CoFeB bilayers". *2018 76th Device Research Conference (DRC),* 1-2 (2018).

[15] Y. Fan, Q. Shao, L. Pan, **X. Che**, Q. He, G. Yin, C. Zheng, G. Yu, T. Nie, M. R. Masir, A. H. MacDonald, K. L. Wang, "Unidirectional Magneto-Resistance in Modulation-Doped Magnetic Topological Insulators". *Nano Letters* **19**, 692-698 (2019).

[16] K. Wang, Y. Liu, W. Wang, N. Meyer, L. H. Bao, L. He, M. R. Lang, Z. G. Chen, **X. Che**, K. Post, J. Zou, D. N. Basov, K. L. Wang, F. Xiu, "High-Quality Bi_2Te_3 Thin Films Grown on Mica Substrates for Potential Optoelectronic Applications". *Applied Physics Letters* **103**, 031605 (2013).

[17] S. H. Tsai, S. Lei, X. Zhu, S. P. Tsai, G. Yin, **X. Che**, P. Deng, J. Ng, X. Zhang, W. H. Lin, Z. Jin, H. Qasem, Z. Zhou, R. Vajtai, N. C. Yeh, P. Ajayan, Y. H. Xie, K. L. Wang, "Interfacial States and Fano-Feshbach Resonance in Graphene-Silicon Vertical Junction". *Nano Letters* **19**, 6765-6771 (2019).

[18] K. Wang, **X. Che**, H. Wu, Q. Shao, "Topological Spintronics and Majorana Fermions". *SPIE Proceedings* **10982**, (2019).

Chapter 1

Introduction

1.1. Spin-Orbit Torque

Flowing electrons generate current. In almost all current semiconductor chips, charge current induced by electrons is the most fundamental building block for all logic and memory units. But apart from charge, electrons also possess a spin degree-of-freedom that has yet been fully exploited. When encountering a spin current, a ferromagnetic layer can manifest distinct resistivity states depending on whether the spins and the magnetization are parallel or antiparallel, due to its different spin density-of-states in the conduction band. On the other hand, the spin of an electron can transfer angular momentum to an adjacent magnetic moment, causing the reorientation of that magnetic moment. Such phenomena open up a new area of spintronics, and spintronics devices have become promising candidates for next-generation logic and memory devices with potentially higher speed, higher density, and better reliability.[*1, 2*] A well-known example is the discovery of giant magnetoresistance (GMR) by A. Fert *et al.*, for which the Nobel Prize in Physics 2007 was awarded and it has become the core of the state-of-the-art magnetic sensor technology in hard disk drives.[*3, 4*]

Another phenomenon that has attracted intensive research effort in spintronics is spin-transfer torque (STT).[*2, 5*] Figure 1-1(a) schematically shows an example of a magnetic tunnel junction (MTJ) structure composed of a ferromagnetic metal/insulator/ferromagnetic metal trilayer stack. When a charge current passes through the bottom ferromagnet layer (fixed layer), the electrons first become spin-polarized by the ferromagnetism inside this layer, and the spin-angular momenta will be transferred to the top ferromagnet layer (free layer) after tunneling through the tunneling barrier. The transfer of spin-angular momenta will induce the precessional motion of the magnetization as shown in Figure 1-1(b), and such magnetization dynamics can be analytically described by the Landau–Lifshitz–Gilbert–Slonczewski equation as

$$\frac{\partial \boldsymbol{m}}{\partial t} = -\gamma \boldsymbol{m} \times \boldsymbol{H_{eff}} + \alpha \boldsymbol{m} \times \frac{\partial \boldsymbol{m}}{\partial t} + \boldsymbol{\tau} \qquad (1-1)$$

where $\boldsymbol{m}$ is a unit vector along the magnetization direction, $\gamma = g\mu_B/\hbar$ is the gyromagnetic ratio (μ_B is the Bohr magneton and g is the Lande g-factor), $\boldsymbol{H_{eff}}$ denotes the effective magnetic field, α is the Gilbert damping constant, and $\boldsymbol{\tau}$ represents the current-induced STT.[*6-8*] If a sufficiently large current is applied, the STT exerted on the magnetization can lead to the switching of its direction in its final state after it returns to equilibrium. Consequently, this results in two distinct states of the magnetization after switching: ‘up’ state and ‘down’ state, which resemble ‘0’ and ‘1’ in logic operations and can be harnessed to store information. The read-out operation in this structure can be realized by utilizing a phenomenon similar to GMR called tunneling magnetoresistance (TMR). In this phenomenon, if a spin-polarized current in an MTJ tunnels through the tunneling barrier and encounters the ferromagnet layer, the MTJ will manifest different resistance depending on how the spin-polarization aligns with the magnetization due to the spin density-of-states. Therefore, the different magnetization states can be distinguished by the TMR after passing through a small current in this structure as described by $TMR = \frac{R_{AP}-R_P}{R_P}$, where TMR is the relative resistance change, R_{AP} is the electrical resistance in the anti-parallel state, R_P is the electrical resistance in the parallel state.

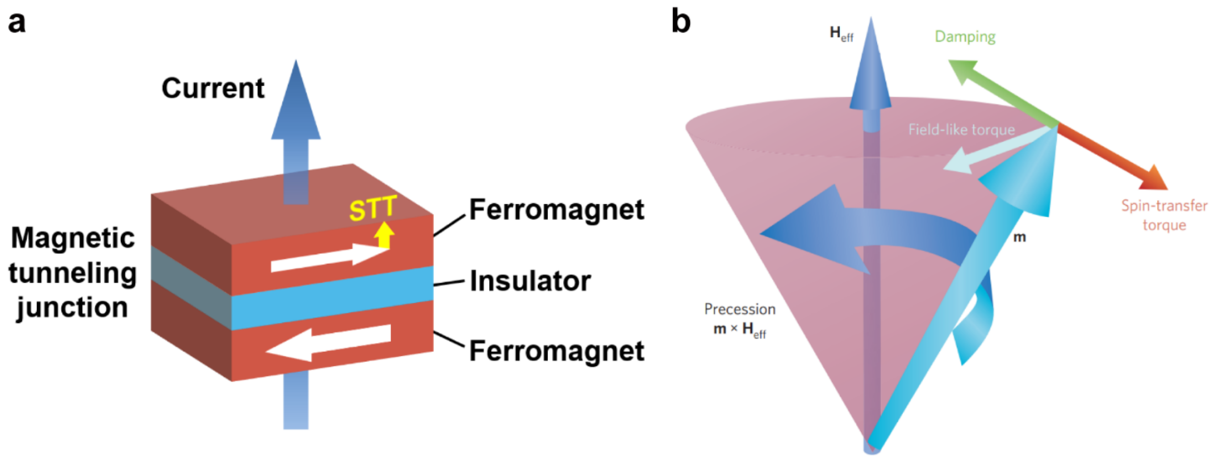

Figure 1-1. Spin-transfer torque and the precession of magnetization upon experiencing torques. (a) Schematic illustration of a magnetic tunneling junction (MTJ) consisting of a ferromagnet/insulator/ferromagnetic sandwiched structure. When a current is vertically applied on the MTJ, spins polarized by the bottom ferromagnet layer will transfer angular momenta and exert torques on the magnetization in the top ferromagnet layer, named as spin-transfer torque. (b) The precession of magnetization around its equilibrium state, driving by a field-like torque, a damping-like torque, and a spin-transfer torque. The magnetization dynamics can be analytically described by the Landau–Lifshitz–Gilbert–Slonczewski equation. Figure adapted from Ref. [*6*]

Through this approach, such a system can be implemented as a fundamental unit in memory devices, and the random access memory based on this structure is called spin-transfer torque magnetic random access memory (STT-MRAM). The structure of a basic memory cell of the STT-MRAM is schematically illustrated in Figure 1-2. A transistor with its source connected to the source line has its drain linked to an MTJ. The 'write' operation is achieved via the 'on' and 'off' states of the transistor manipulating the tunneling current, which is controlled by the gate voltage from the word line. The 'read' operation can be fulfilled by measuring the voltage on the read bit line from the TMR across the MTJ. Compared to the conventional hard disk drive and flash memory, STT-MRAM has already demonstrated a number of advantages, such as higher speed (<10 ns) thanks to the fast dynamics of ferromagnetism, and theoretically almost unlimited endurance (>10^{16}) owing to the stability of the magnetization states over a long period of time.[*2*, *9*, *10*] It also possesses the advantage of non-volatility when compared to dynamic random access memory. Recently, the conversion of STT-MRAM from in-lab prototypes to mass production is considered in the roadmap of many enterprises, and pioneer STT-MRAM products have been successfully manufactured by Everspin® and Samsung®.

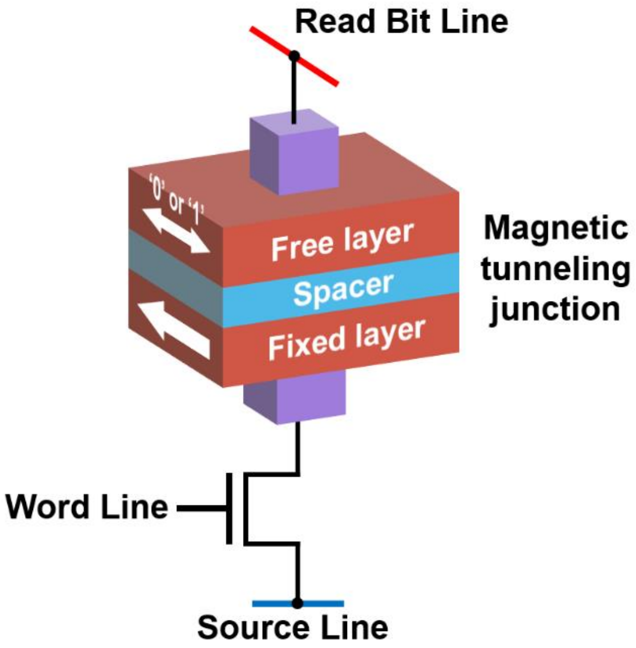

Figure 1-2. Schematic of a memory cell in STT-MRAM. Information is stored in the magnetization of the free layer in the MTJ, which can be switched between '0' and '1' states after passing a vertical current

from the source line. ‘Write’ operation is controlled by the transistor connected to the word line, while ‘read’ operation is fulfilled by determining the tunneling magnetoresistance from the read bit line.

However, due to the fact that STT-MRAM relies on the tunneling of spin current, reliability issues arise as a result of the deterioration of the tunneling barrier, owing to dielectric breakdown after certain read/write cycles. It also suffers from high power dissipation due to the highly resistive tunneling barrier. To circumvent these issues, another spin-torque mechanism to manipulate the magnetization without a tunneling barrier has become attractive and is currently under wide investigation, which is called spin-orbit torque (SOT). In special relativity, the orbital motion of an electron under the electric field $\boldsymbol{E}$ from the nucleus experiences an equivalent magnetic field of $\boldsymbol{B} = -\frac{\boldsymbol{v}\times\boldsymbol{E}}{c^2}$ that interacts with its spin. The Hamiltonian of such interaction can be expressed as[*11*]

$$\Delta H_{SO} = \frac{\boldsymbol{\mu_B}}{\hbar m_e e c^2}\frac{1}{r}\frac{\partial U(r)}{\partial r}\boldsymbol{L}\cdot\boldsymbol{S} \qquad (1-2)$$

where m_e is the electron mass, r is the orbit radius, U is the potential in the atom, and the interaction between spin and orbit is called spin-orbit interaction or spin-orbit coupling (SOC). Such SOC can give rise to an anomalous group velocity of the electrons and thus the conversion between charge current and spin current via the spin Hall effect, where the spins of opposite directions accumulate in opposite sides of a material transverse to the applied current direction as shown in Figure 1-3(a).[*12-14*] Spin Hall effect is more pronounced in heavy elements that have stronger SOC, and it was experimentally observed for the first time in a GaAs device by Kerr rotation microscopy (Figure 1-3(b)).[*14*] In this figure, when a longitudinal current passes through the GaAs devices, lateral spin accumulation on both edges of the device owing to the spin Hall effect can be observed under Kerr rotation microscopy indicated by red color (spin-up) and blue color (spin-down).

Another origin of spin accumulation is the Rashba effect, which is caused by the strong electric field at the interface of two different material layers due to the breaking of inversion symmetry.[*15, 16*] As displayed in Figure 1-3(c), the inversion symmetry breaking can induce Rashba spin-splitting of two spin-subbands of the band structure and result in spin-polarization transverse to its momentum on the Fermi circles in *k*-space. Once generated by a charge current flow, the spin accumulation from either spin Hall effect or Rashba effect can exert SOT on the adjacent magnetic moment as schematically demonstrated in Figure 1-3(d).[*17, 18*] If the SOT is sufficiently strong, it can also switch the direction of the magnetization similar to STT but with lower power dissipation due to the absence of a tunneling barrier. Such SOT-driven magnetization switching can be a desirable approach in realizing miniaturized spintronic memory devices with high efficiency. Compared to STT-MRAM, magnetic memory devices utilizing SOT offer the advantages of lower power consumption, higher endurance, and better scalability.

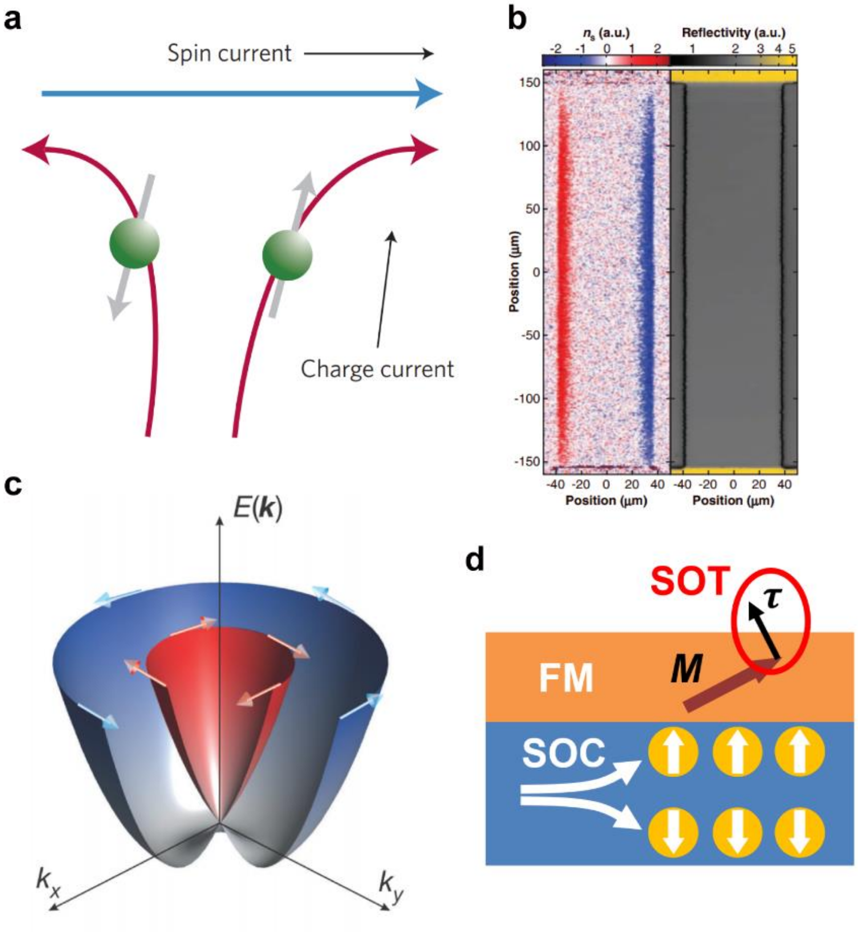

Figure 1-3. Spin accumulation and SOT arising from spin Hall effect or Rashba effect. (a) A sketch of spin Hall effect. In this phenomenon, a charge current can induce a transverse spin current as a result of SOC. Figure adapted from Ref. [*19*]. (b) Observation of spin accumulation due to spin Hall effect by Kerr rotation microscopy. The red color and blue color regions indicate spin-up and spin-down, respectively. Figure adapted from Ref. [*14*]. (c) Illustration of a band structure with Rashba spin-splitting. A spin on the Fermi circles is polarized and perpendicular to its momentum in *k*-space. Figure adapted from Ref. [*20*]. (d) SOT driven by spin accumulation on an adjacent ferromagnetic layer. The SOT can cause reorientation and even switching of the magnetization, which can be implemented as the 'write' operation in magnetic memory devices.

1.2. Spin-Orbit Torque-Driven Magnetization Switching

At an early stage, SOT by spin-orbit coupling and spin Hall effect was demonstrated by Buhrman *et al.* in a heavy metal/ferromagnet (HM/FM) bilayer structure.[*21*] Figure 1-4(a) shows the material structure composed of a Pt layer and a permalloy (Py) layer for SOT measurement. When an AC current with a frequency that is close to the ferromagnetic resonance (FMR) frequency of the Py layer (typically a few GHz) is fed into the heterostructure device, the current-induced SOT can drive the precession of the magnetization at its resonance frequency. The precession subsequently causes the oscillation of the anisotropic magnetoresistance of Py, which can be further detected by measuring the DC voltage signal V_{mix} generated across the sample from the mixing of the radiofrequency current and the oscillating resistance (Figure 1-4(b)). By fitting to V_{mix} and separating its symmetric and asymmetric components, the strength of the SOT effective field H_{eff}, as well as the ratio of spin current density J_s over charge current density J_c, can be extracted. Here, the ratio of J_s over J_c is defined as the spin Hall angle θ_{SH} described by

$$\theta_{SH} = \frac{J_s}{J_c} \qquad (1-3)$$

and it is a crucial term that quantitatively describes the capability of a material in converting charge current to spin current. Here in the Pt/Py system, a spin Hall angle of $\theta_{SH} = 0.05 \sim 0.06$ was demonstrated. Almost at the same time, the observation of SOT was also reported by Gambardella *et al.* in Co/Pt nanostructures as displayed in Figure 1-4(c).[*18*] In this material structure, inversion symmetry is broken at the interface between Co and Pt such that spin accumulation is induced by the strong Rashba effect at the interface. After applying current pulses with an adequate amplitude, it can be observed under differential Kerr microscopy that the magnetic domains inside the nanostructures expand or contract depending on the direction of the current. The observation of the effective field provides a visualized experimental signature that a SOT effective field H_{eff} is established on the magnetization by current-induced SOT.

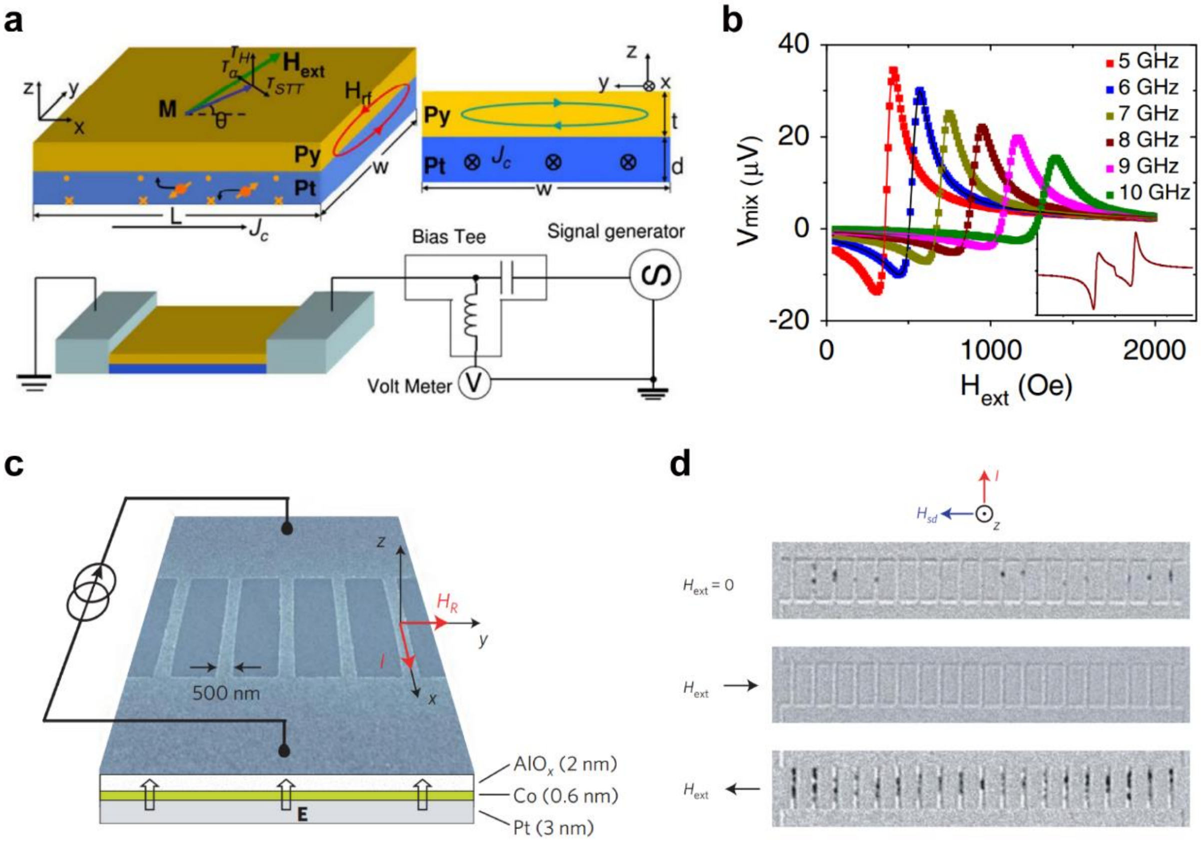

Figure 1-4. Magnetization dynamics and effective field induced by SOT. (a) Precession of magnetization by SOT in a Py/Pt bilayer structure after feeding in an AC current at radiofrequency. (b) Detected voltage across the Py/Pt device owing to the mixing of its anisotropic magnetoresistance under ferromagnetic resonance and the radiofrequency current. Figure (a) and (b) adapted from Ref. [*21*].(c) AlO_x/Co/Pt structure with fabricated nano-devices. (d) Domain formation in the AlO_x/Co/Pt nano-devices driven by Rashba effect-induced SOT. The input of a pulse current can generate a SOT effective field and

lead to the expansion or contraction of the domains similar to an external magnetic field. Figure (c) and (d) adapted from Ref. [*18*].

Soon after, switching of perpendicular magnetization driven by SOT was achieved in HM/FM structures by L. Liu *et al.* and I Miron *et al.*[*17, 22*] Among those research efforts, Gambardella *et al.* investigated a thin film stack comprising Co/Pt and an AlO_x capping layer as schematically shown in Figure 1-5(a).[*22*] The Co layer is perpendicularly magnetized, and the Rashba interaction induced by the asymmetric platinum and AlO_x interface layers generates the spin accumulation as well as SOT to switch the magnetization. An image of the prototypical reconfigurable ferromagnetic switch based on this structure is demonstrated in Figure 1-5(b). After passing pulsed current through the device in the x-direction, the magnetization along the z-direction is able to switch between 'up' state and 'down' state, depending on the current direction (Figure 1-5(c)). The magnetization switching is robust and repeatable after multiple switching cycles.

In the meantime, L. Liu *et al.* took another approach of utilizing Ta/CoFeB and Pt/CoFeB heterostructures, where the CoFeB layer possesses magnetization with perpendicular anisotropy and the heavy metal (Ta and Pt) layers provides spin current via spin Hall effect (Figure 1-5(d)).[*17*] When an in-plane magnetic field of $B_{ext} = \pm 10\, mT$ is applied to break symmetry, the perpendicular magnetization can be switched by DC current and detected by anomalous Hall effect as displayed in Figure 1-5(e). The detected magnetization can be either in 'up' state or 'down' state inferred from the anomalous Hall resistance, while the switching loops exhibit certain coercivity during switching owing to the magnetic hysteresis of CoFeB itself. These device prototypes are simple, scalable and also compatible with present-day magnetic recording technology. Besides, the perpendicular magnetization in these devices is also amenable to miniaturization for further scaling of memory devices.

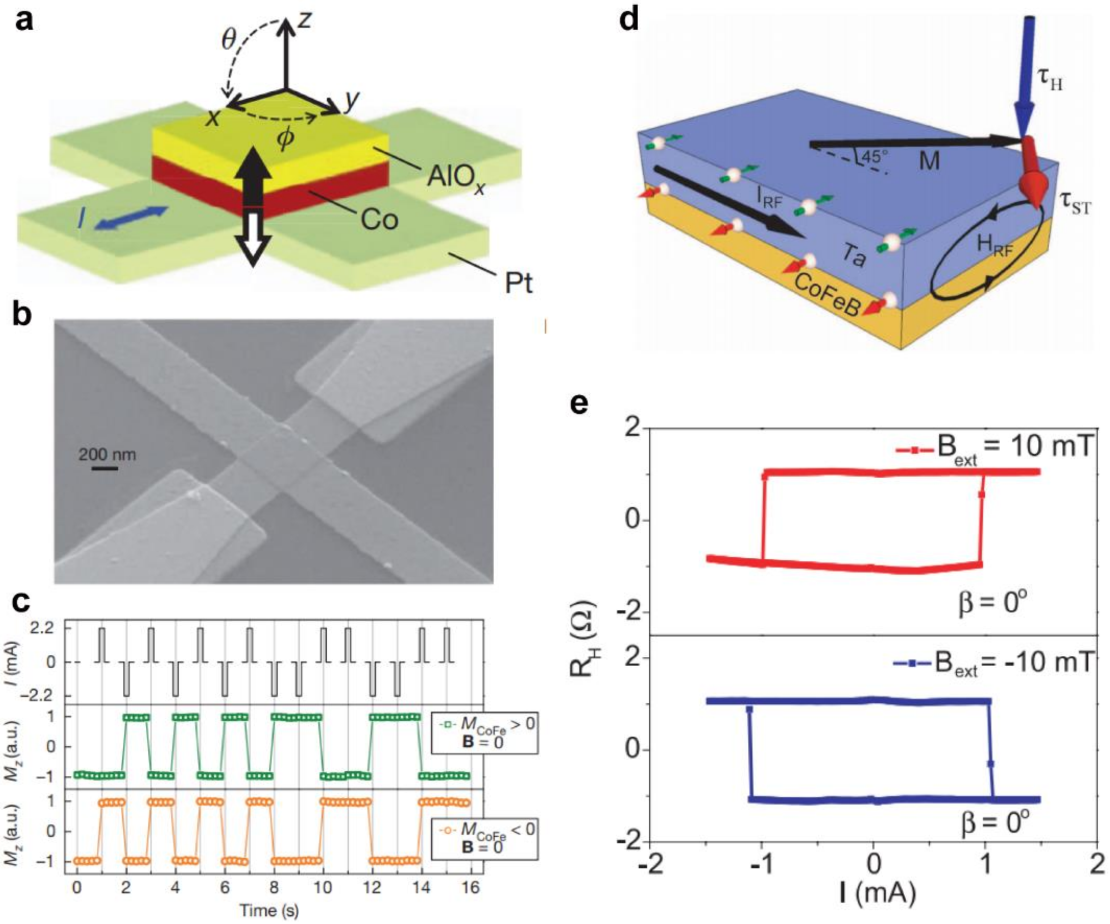

Figure 1-5. Switching of perpendicular magnetization by SOT. (a) AlO_x/Co/Pt structure with Rashba effect due to inversion symmetry breaking. (b) Scanning electron microscope image of the device for magnetization switching. (c) Switching of perpendicular magnetization in the AlO_x/Co/Pt device by pulsed current. The magnetization can be switched between ‘up’ and ‘down’ states repeatedly by reversing the current direction for multiple cycles. Figure (a), (b) and (c) adapted from Ref. [*22*]. (d) Ta/CoFeB structure

and SOT on the CoFeB magnetization by spin Hall effect. (e) SOT-driven perpendicular magnetization switching in CoFeB after applying a DC current. The magnetization has opposite final state depending on the current direction and is detected by measuring anomalous Hall resistance. Figure (d) and (e) adapted from Ref. [*17*].

1.3. From Quantum Hall Effect to 3D Topological Insulators

In 1980, von Klitzing *et al.* unexpectedly discovered that in silicon-based MOSFET devices with high-mobility electrons, the Hall conductance can be quantized under a high magnetic field.[*23*] This quantum mechanical phenomenon of an electronic system is later known as the quantum Hall effect (Figure 1-6(a)).[*24-26*] The discovery of the quantum Hall effect was awarded the 1985 Nobel Prize in Physics and opened up a new era of exploring condensed-matter systems from a topological point-of-view. Consider a free-electron system where electrons circularly move under an external magnetic field at a certain cyclotron frequency ω_c. When the magnetic field is sufficiently high, the circular orbits of electrons can be quantized and lead to discretized Landau levels in its band structure with energy $E_m = \hbar\omega_c(m + 1/2)$ $(m = 0, 1, 2, \ldots)$ as shown in Figure 1-6(b) and 1-6(c). If the Fermi level resides between two Landau levels with *N* Landau levels filled by electrons, the interior of the systems can be considered as an insulator and is topologically non-trivial compared to a normal band insulator. Consequently, on the edge of the system, the band structure with discretized Landau levels cannot be continuously deformed without closing its energy gap. This gives rise to the dissipationless transport of the electrons at the edge, *i.e.*, chiral edge states, and a quantized Hall conductivity of $\sigma_{xy} = Ne^2/h$.

The above scenario serves as the most fundamental toy model in topological band theory. More specifically, electrons can be characterized in terms of the Berry phase given by the line integral of $A_m = i\langle u_m|\nabla_k|u'_m\rangle$ (Berry connection), where $|u_m(\boldsymbol{k})\rangle$ is the Bloch wave functions. The surface integral of the total Berry flux in the Brillouin zone gives rise to a topological invariant

$$N_m = \frac{1}{2\pi}\int d^2\boldsymbol{k}\, \nabla \times A_m \qquad (1-4)$$

which is called the Chern number and topologically classifies condensed-matter systems gapped band structures.[*11*] In quantum Hall systems, the Berry phase is generally introduced by an external magnetic field. However, besides magnetic field it can also be induced by SOC, which leads to spin Hall effect and ultimately quantized version of spin Hall effect called quantum spin Hall effect, if the SOC is sufficiently strong. Such a new phase was theoretically proposed by F.D.M Haldane and then developed by C. Kane and E. Mele in graphene systems with strong SOC.[*27-29*] The quantum spin Hall phase is time-reversal invariant, and instead of the Chern number as in quantum Hall effect it is classified by a $\mathbb{Z}_2$ topological invariant. Moreover, unlike spin-less quantum Hall effect, up-spins and down-spins on the edge of the quantum spin Hall system propagate toward opposite directions known as helical transport and are protected by time-reversal symmetry (Figure 1-6(d)). This time-reversal symmetry leads to the destructive interference of the forward and backward paths such that backscattering by non-magnetic impurities is strictly prohibited.

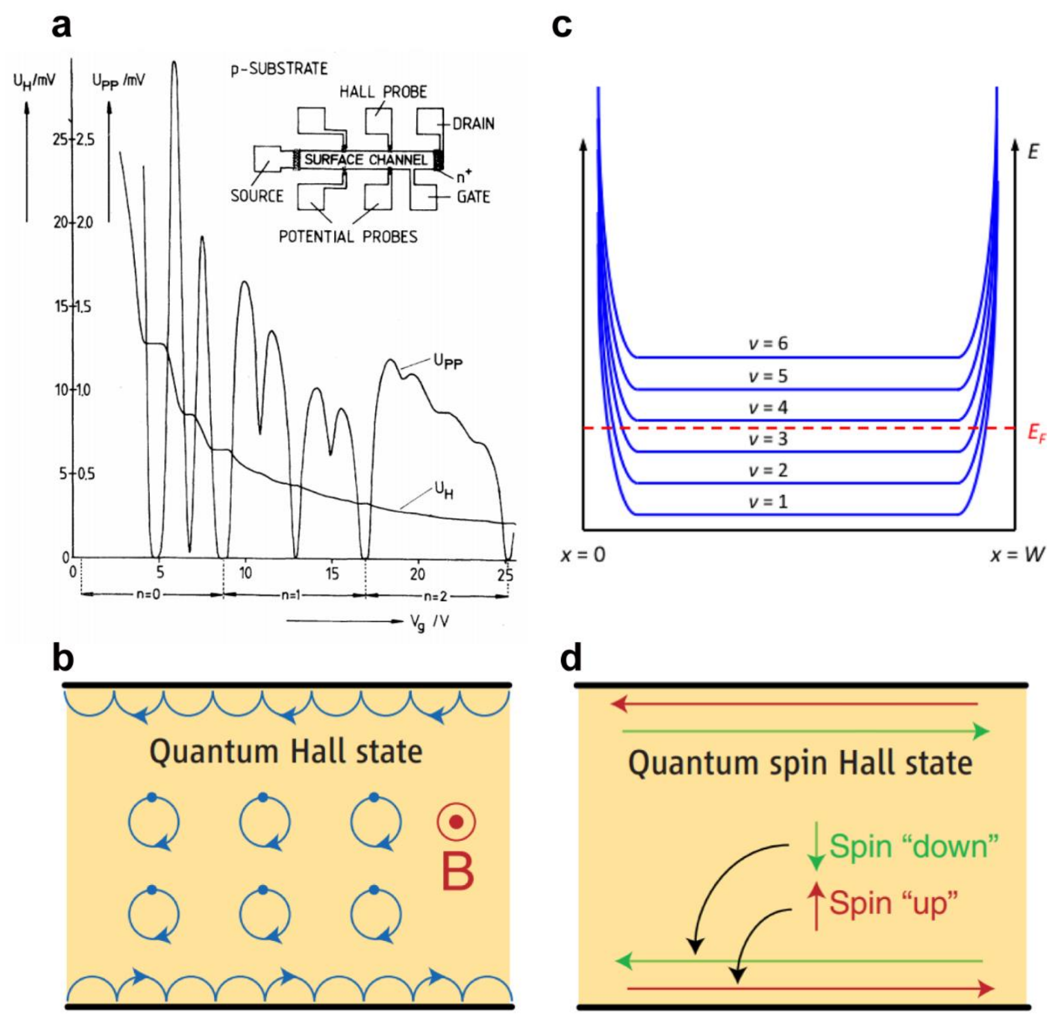

Figure 1-6. Quantum Hall effect and quantum spin Hall effect. (a) The discovery of the quantum Hall effect in a Si-based MOSFET device, where the Hall resistance becomes quantized under a high magnetic field and the longitudinal resistance vanishes to zero. Figure adapted from Ref. [*23*]. (b) Discretized Landau levels in the band structure due to the circular motion of electrons under a high magnetic field. (c) Cyclotron motion of electrons with quantized energies and orbits in the quantum Hall state, causing an insulating state in the interior of the material. On the edge of the material, the chiral ballistic transport of electrons gives rise to the chiral edge state that is dissipationless. Figure adapted from Ref. [*25*]. (d) The motion of electrons can also be altered by SOC instead of an external magnetic field, which in some cases leads to the quantized version of the spin Hall effect or quantum spin Hall effect. In the quantum spin Hall state, electrons with

opposite spin direction propagate in opposite directions and are protected by time-reversal symmetry. Figure (b) and (d) adapted from Ref. [*30*].

Although the quantum spin Hall phase was first proposed in graphene systems, the SOC in graphene is too weak to introduce a large Berry phase. Later, it was predicted by B. A. Bernevig and X. Qi *et al*. that the quantum spin Hall effect could exist in a CdTe/HgTe/CdTe quantum well structure, where the SOC is strong enough to invert the HgTe band structure as displayed in Figure 1-7(a).[*31, 32*] Specifically, in Figure 1-7(b) the Γ_6 subband in the conduction bands in HgTe becomes valence band, while the Γ_8 subband in the valence bands is lifted to be above the Γ_6. Since the inverted bands in HgTe are topologically nontrivial compared to the trivial bandgap in CdTe, the band structure cannot continuously deform without closing the bandgap at the interfaces, and the valence and conduction bands must cross with each other at the interface of the sandwiched structure. This leads to the quantum spin Hall phase in the system with metallic edge states and gapped bulk bands, where the dissipationless edge states are protected by time-reversal symmetry. Following the theoretical prediction, the experimental signature of the quantum spin Hall effect was demonstrated by B. A. Bernevig, *et al.* in the CdTe/HgTe/CdTe quantum well structure, which manifests as a quantized longitudinal conductance of $\sigma_{xx} = 2e^2/h$ since there are two channels for opposite spin directions.[*33*] The quantum spin Hall phase in this system vanishes and becomes the quantum Hall phase when a large external magnetic field is applied to break the time-reversal symmetry.

The condensed-matter system with quantum spin Hall phase is called quantum spin Hall insulator, and later given the name as 2D topological insulator (TI). L. Fu and C. Kane further expanded this phase from 2D scenarios to 3D scenarios as 3D topological insulator, where the 1D topologically protected helical edge states evolve to 2D surface states that exist on the entire material surface in certain materials with inversion symmetry.[*34*-*36*] In 2010 H. Zhang *et al*. theoretically demonstrated by *ab-initio* calculation that chalcogenide compounds Bi_2Se_3, Bi_2Te_3 and Sb_2Te_3 are 3D topological insulators.[*37*] As shown in Figure 1-7(c), these chalcogenide compounds share the same hexagonal crystalline structure comprised of quintuple layers, where one quintuple layer is a five-layer stack of different atoms. Taking Bi_2Se_3 as an example, the $P1_z^+$ energy level of Bi element and $P2_z^-$ energy level of Se element are inverted at the Γ point, resulting in band inversion and topological surface states inside the inverted bandgap in Bi_2Se_3 from *ab-initio* calculation in Figure 1-7(d). Later the technique of angle-resolved photoemission spectroscopy (ARPES) was adopted to investigate the bandstructure of Bi_2Se_3 and Bi_2Te_3. An example of this characterization approach revealed Dirac cone-like surface states in the bulk band gap (Figure 1-7(e)) similar to the surface states band structure from *ab-initio* calculation, and experimentally demonstrated the 3D topological insulator phase in these chalcogenide compound materials.[*38*-*40*]

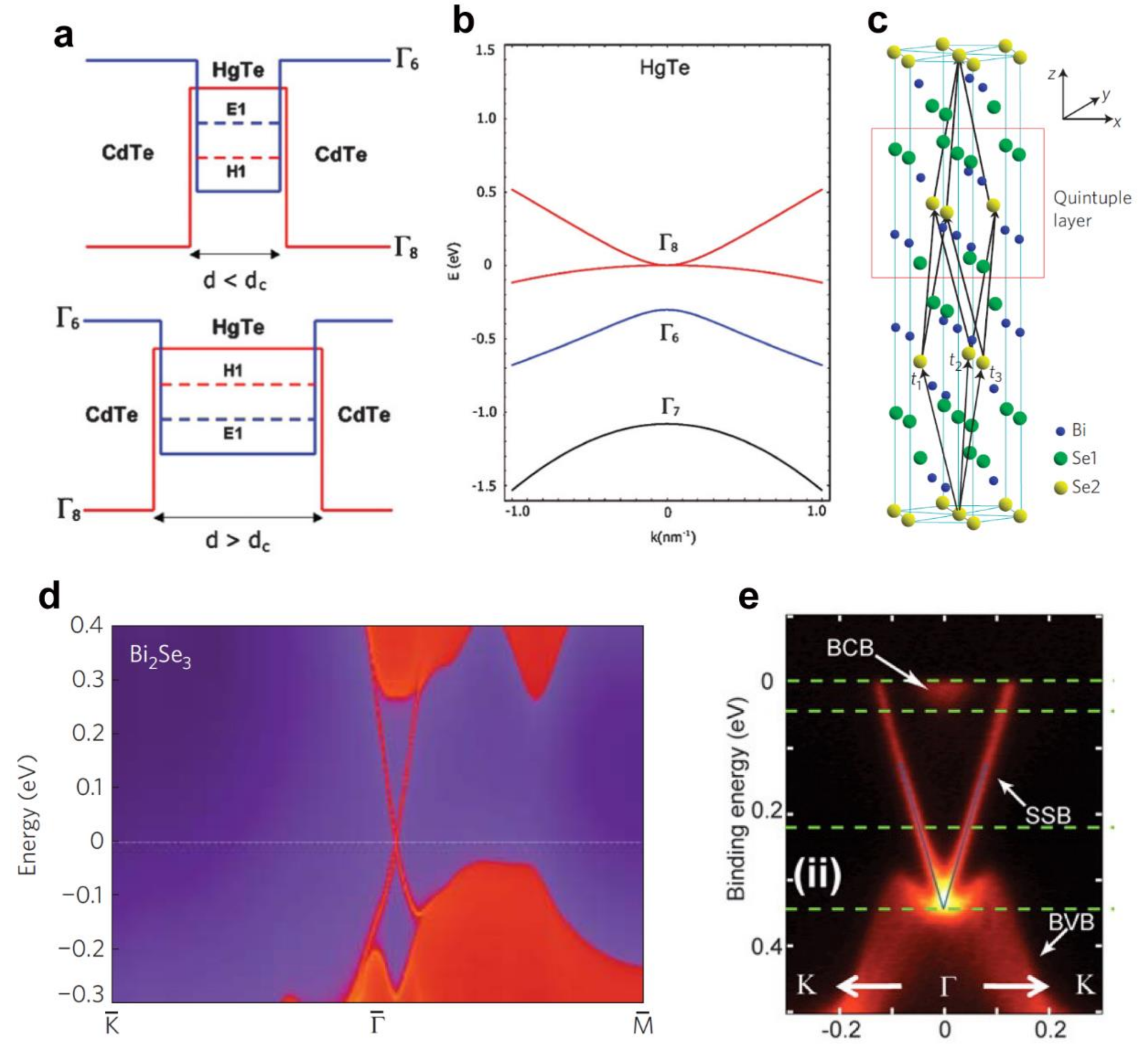

Figure 1-7. Discovery of 2D and 3D topological insulators. (a) CdTe/HgTe/CdTe quantum well structure as a 2D topological insulator. (b) Band inversion in HgTe, where the the Γ_6 subband in the conduction bands becomes a valence band and the Γ_8 subband in the valence bands becomes a conduction band. Figure (a) and (b) adapted from Ref. [*32*]. (c) Crystalline structure of Bi_2Se_3, which is one of the predicted 3D topological insulators. Inside the hexagonal-structure unit cell, five layers of atoms form a quintuple layer and the quintuple layers are bonded by van der Waals force. (d) Band structure of Bi_2Se_3 by *ab-initio* calculation. A Dirac cone-shaped surface state band emerges between the bulk conduction bands and valence bands. Figure (c) and (d) adapted from Ref. [*37*]. (e) Experimental observation of the surface state Dirac cone in Bi_2Te_3 by ARPES. Figure adapted from Ref. [*38*].

1.4. Spin-Orbit Torque from Topological Insulators

As discussed in Chapter 1.3, in 2D topological insulators with quantum spin Hall phase, up-spins and down-spins propagate in the opposite directions on the material edge, forming a 1D helical edge states that are protected from backscattering by time-reversal symmetry. When it comes to 3D topological insulators, the spins on the topological surface states (TSS) are perpendicular to their momenta in *k*-space as shown in Figure 1-8(a). Such a correlation between spin and momentum is called spin-momentum locking.[*31*] In real-space, spin-momentum locking manifests as transverse spins to their propagation directions. Spin-momentum locking in TIs was theoretically predicted before the terminology of TI appears in literatures, and it was first experimentally detected using spin-resolved ARPES to investigate the surface band structure of TIs.[*39*] Figure 1-8(b) shows the spin-resolved ARPES image of the surface Dirac cone of Bi_2Te_3 in the k_x-k_y plane, revealing a Fermi circle with spin-polarization in the surface Dirac cone. The spin-polarization in the k_y direction can be quantitatively measured along the cut of the $\bar{\Gamma} - \bar{\mathrm{M}}$ direction, and the spin profile can be seen in Figure 1-8(c). At k_x=0 ($\bar{\Gamma}$ point), the spin-polarization is essentially zero. It reaches a maximum of 0.2 at k_x=0.08 (on the Fermi circle), consistent with the spin-momentum locking picture of the surface state Dirac cone.

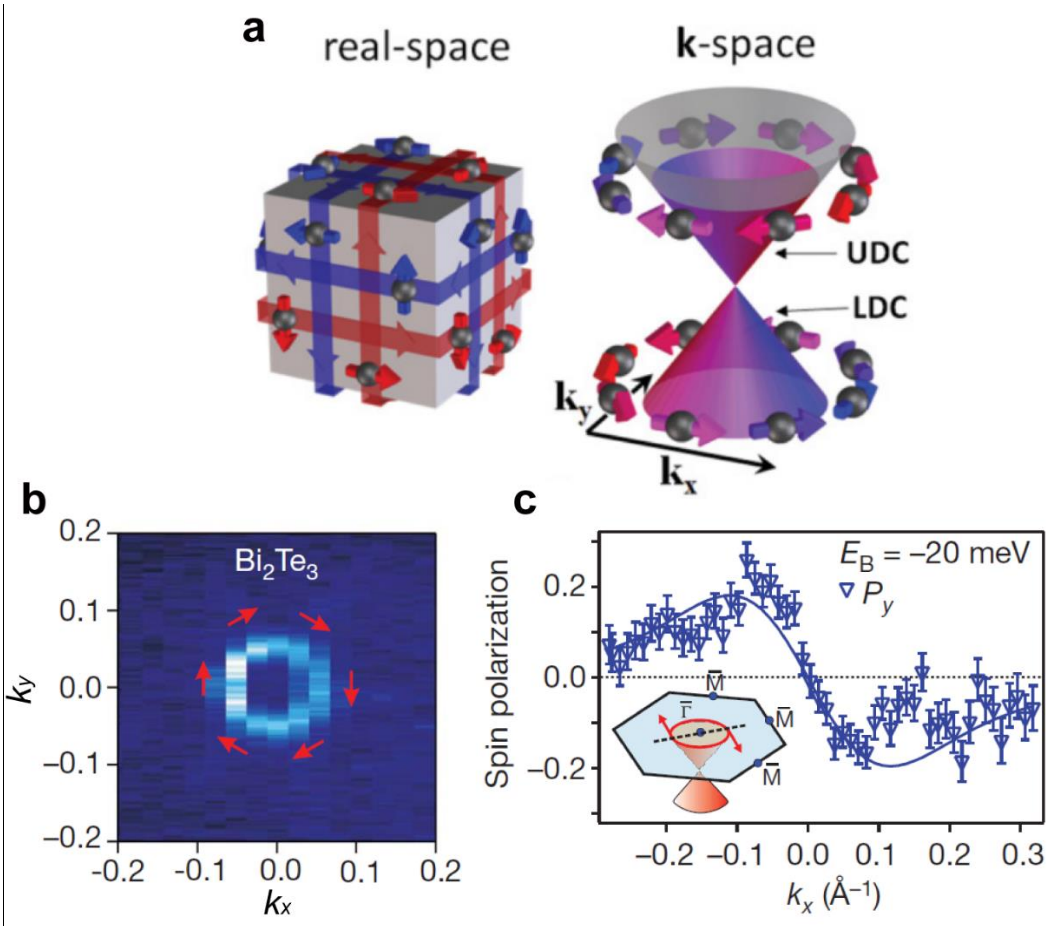

Figure 1-8. Spin-momentum locking of the topological surface states in topological insulators. (a) Spin-momentum locking of the surface states in real-space and in *k*-space. A spin on the Fermi circle in *k*-space is perpendicular to its momentum. Consequently, it is transverse to its propagation direction in real-space. The upper Dirac cone and lower Dirac cone of the surface states have opposite spin-momentum locking chiralities. Figure adapted from Ref. [*41*]. (b) Experimental signature of spin-momentum locking in Bi_2Te_3 using spin-resolved ARPES. (c) Measured spin-polarization transverse to the $\bar{\Gamma} - \bar{\mathrm{M}}$ direction on the surface states by spin-resolved ARPES. The spin-polarization was estimated to be around 0.2 from ARPES. Figure (b) and (c) adapted from Ref. [*39*].

Spin-resolved ARPES can be one viable technique to detect the spin polarization in TSS. However, the instrument setup of such measurement is bulky and is limited to the characterization of the material property only. If we wish to further harness the spin polarization of the TSS for device-level applications, all-electrical spin detection on the TI devices is desired. Consequently, the electrical detection of spin polarization in TIs was demonstrated in Bi_2Se_3 devices with a spin-detection configuration.[*42*] Figure 1-9(a) displays a schematic illustration of the device geometry, where MTJs with a ferromagnetic Fe layer are fabricated on the Bi_2Se_3 bar surface. If a DC current passes through the Bi_2Se_3 film, carriers on the surfaces states become spin-polarized due to the spin-momentum locking and the shift of the Fermi circle. When spins tunnel through the MTJs, the Fe layer will either have a high voltage state or low voltage state depending on whether the spins and the Fe magnetization are parallel aligned or antiparallelly aligned due to the TMR of the MTJs. Through this approach, the spin polarization in the TSS can be electrically detected. Figure 1-9(b) shows the measurement result from a magnetic tunneling junction manifesting as a hysteresis loop. When the magnetic field is swept from negative to positive, the magnetization of the Fe layer switches direction, causing the spin configuration to change from antiparallel to parallel and the detected voltage shifting from high state to low state.

At the same time in DRL at UCLA, we also have achieved the electrical detection of the surface state spin-polarization in our molecular beam epitaxy (MBE)-grown $Bi_xSb_{2-x}Te_3$ (BST) film by adopting a similar device geometry.[*43*] The device schematic is shown in Figure 1-9(c), where a ferromagnetic Co layer and an AlO_x tunneling barrier are deposited on the BST Hall bar to serve as the MTJs. A small AC current superimposed on a DC current is applied through the device such that spin polarization can be induced by the DC current and probed by the AC current. By scanning the in-plane magnetic field to reverse the Co magnetization, the spin polarization is detected through measuring the voltage of the Co layer (Figure 1-9(d)) as a result of the TMR across the MTJs, which manifests as a magnetic hysteresis loop similar to the previous experiment. The above experiments demonstrate that the spin-polarization from spin-momentum locking in the TSS can be electrically detected in device-level. Therefore, it possesses the potential to be further utilized in spintronic device applications.

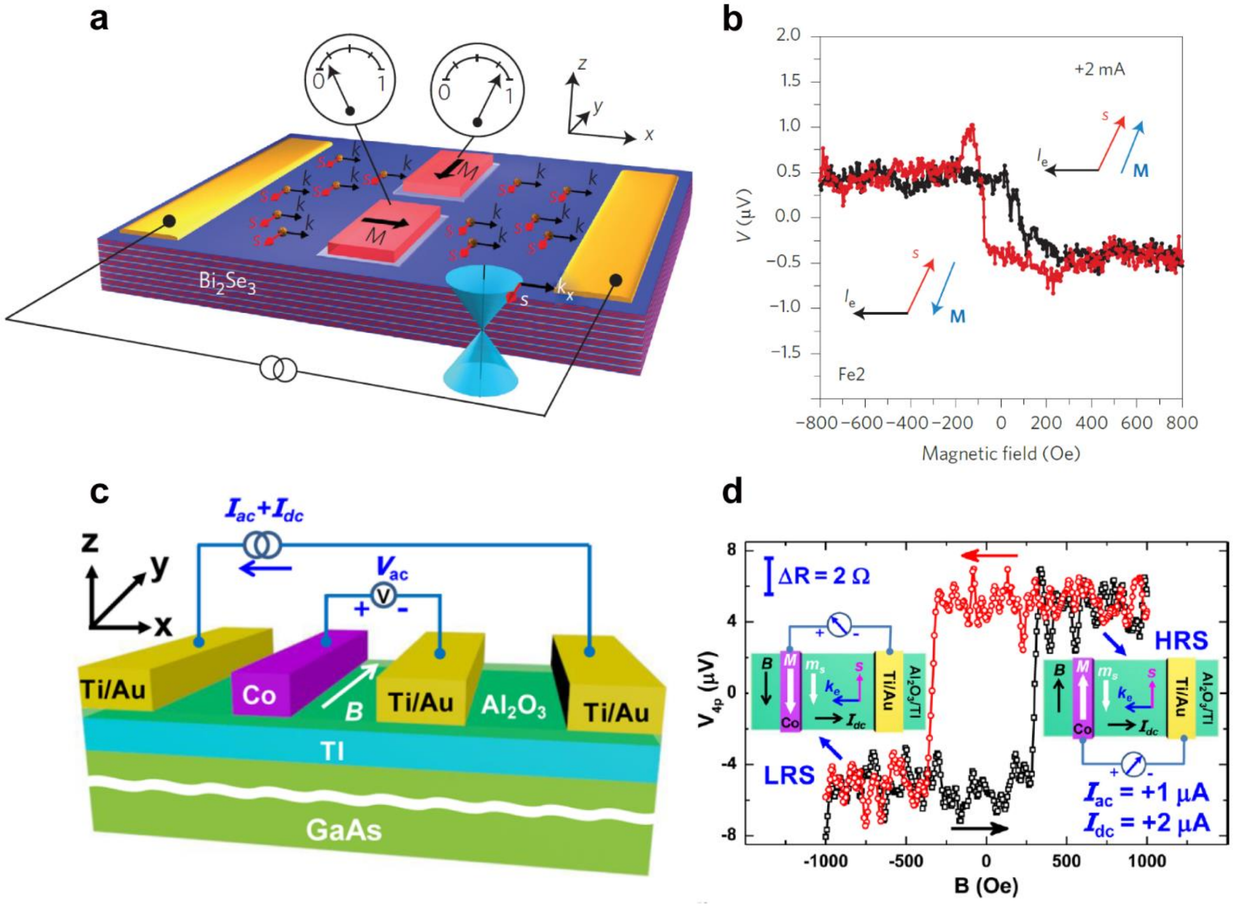

Figure 1-9. Electrical detection of spin-polarization on topological surface states. (a) Schematic illustration of spin detection on Bi_2Se_3 surface via magnetic tunneling junctions. When spins tunnel through the magnetic tunneling junctions, the top ferromagnetic layer will have either high voltage or low voltage

state depending on whether the spins and the magnetization are parallel or antiparallel, as a result of tunneling magnetoresistance. (b) Detected voltage signal on a magnetic tunneling junction. When the negative external magnetic field is increased, the magnetization in the magnetic tunneling junction reverses its direction, causing the alignment of incoming spins and the magnetization changes from antiparallel to parallel. Figure (a) and (b) adapted from Ref. [*42*]. (c) Schematic illustration of spin detection in an MBE-grown $Bi_xSb_{2-x}Te_3$ film by a Co-based magnetic tunneling junction. (d) Detected voltage change on the Co layer due to different tunneling magnetoresistances under a sweeping magnetic field. Figure (c) and (d) adapted from Ref. [*43*].

Since spin polarization from spin Hall effect or Rashba effect can generate SOT on adjacent magnetization, it is natural to consider the possibility that spin-polarized TSS in topological insulators can exert SOT on magnetic moments as well. The experimental demonstration of SOT from TI was firstly reported by Y. Fan *et al.* in DRL, where we also demonstrated SOT by TI in a $Bi_xSb_{2-x}Te_3$/Cr-$Bi_xSb_{2-x}Te_3$ (BST/Cr-BST) heterostructure.[*44*] In this system, magnetization is induced inside TI by doping with Cr, and the bottom surface state directly exerts SOT on the magnetization in the Cr-BST layer as shown in Figure 1-10(a). A measurement technique called second harmonic measurement was adopted to quantify the SOT on the magnetization of the MTI layer from TSS, revealing a giant θ_{SH} of 140-425. Moreover, we also achieved magnetization switching by the SOT in the BST/Cr-BST heterostructure. With the assistance of an in-plane magnetic field to break symmetry, the application of a sufficiently large DC current can switch the magnetization perpendicularly in the Cr-BST layer, and the up/down state of the magnetization can be fully controlled by the applied current direction. In Figure 1-10(b), the anomalous Hall resistance indicating the magnetization direction switches its sign when the applied DC current is higher than 20μA. Although the SOT and current-driven magnetization switching was demonstrated at a low temperature of 1.9 K, it paved a new way of utilizing TIs to implement spintronic devices and magnetic memories. SOT from TI was also reported in a Bi_2Se_3/permalloy heterostructure, where the SOT is measured by an alternative method called spin-torque ferromagnetic resonance (ST-FMR) (Figure 1-10(c)).[*45*] This measurement approach utilizes the FMR of the magnetic layer driven by SOT with radiofrequency, which is induced by feeding in a radiofrequency current with modulated frequency through the bias-tee (Figure 1-10(d)). The FMR can be detected electrically through anisotropic magnetoresistance, and θ_{SH} is quantitatively estimated by fitting to the measured magnetoresistance curve. Here θ_{SH} in TI was measured to be 2.0-3.5 at room temperature, which is more than one order of magnitude higher than θ_{SH} of heavy metals and suggests potentially much stronger SOT originated from TIs.

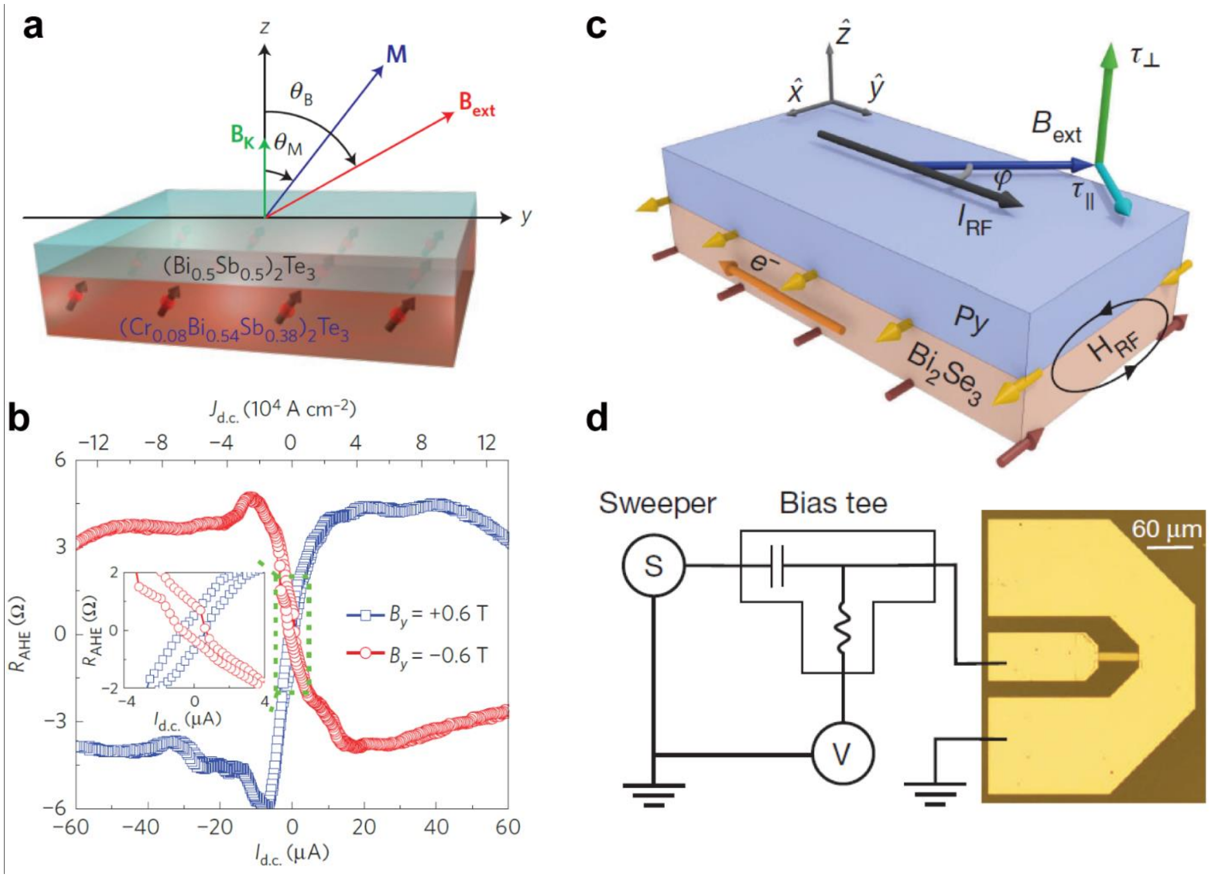

Figure 1-10. Spin-orbit torque from the spin-polarized surface states and magnetization switching in topological insulators driven by the spin-orbit torque. (a) SOT in a $Bi_xSb_{2-x}Te_3$/Cr-$Bi_xSb_{2-x}Te_3$ heterostructure. The bottom surfaces state can exert SOT on the magnetization in the Cr-$Bi_xSb_{2-x}Te_3$ layer, while the SOT from the top surface state is vanishingly small due to the $Bi_xSb_{2-x}Te_3$ spacer layer. (b) Current-driven magnetization switching by SOT in the $Bi_xSb_{2-x}Te_3$/Cr-$Bi_xSb_{2-x}Te_3$ heterostructure. Under a constant in-plane field, an adequate DC current can switch the magnetization between 'up' and 'down' states, which is detected by measuring anomalous Hall resistance. Figure (a) and (b) adapted from Ref. [*44*]. (c) Measurement of SOT in a Bi_2Se_3/Py bilayer structure by ST-FMR. The application of radiofrequency current causes the SOT from surface state to alternate in the same frequency, driving the magnetization to precess in its ferromagnetic resonance. The ferromagnetic resonance can be detected via voltage across the device due to its anisotropic magnetoresistance. (d) Measurement setup of ST-FMR, where radiofrequency

current from the current source passes through the bias tee and the device bar. The voltage across the device can be measured on the contact pads Figure (c) and (d) adapted from Ref. [*45*].

1.5. Dissertation Outline

In this dissertation, we will first discuss the magnetization in topological insulators and the investigation of spin-orbit torque in magnetic topological insulators through transport and optic approaches in Chapter 2. The magnetization in topological insulators can be introduced by both magnetic proximity effect and magnetic doping. The principles of the above techniques and the details of the experiments will be presented. The systematic measurements of SOT accomplished by these two methods offer consistent results, revealing a strong dependence of the spin-orbit torque on topological surface states. We will further explain the correlations among spin-orbit torque, surface state carriers and temperature in this chapter. In Chapter 3, we will discuss magnetization switching driven by spin-orbit torque and field-free magnetization switching by exchange bias-induced symmetry breaking. The investigation on a TI/CrSe bilayer structure will be presented, which demonstrated field-free magnetization switching assisted by exchange-bias. Field-free switching is also realized in a Cr-TI/CrSb heterostructure for operation at elevated temperatures. Lastly, we will summarize the results and give a conclusion of this dissertation in Chapter 4.

Chapter 2

Surface State Carrier Dependent Spin-Orbit Torque in Magnetic Topological Insulators

2.1. Overview

As discussed in Chapter 1.4, the polarized spins on the TSS in TIs can drive strong SOT on neighboring magnetic moments, holding promise for magnetic memory devices with higher efficiency and lower power dissipation. However, so far there are large discrepancies among the reported values of θ_{SH} in TIs, which have been causing a major controversy in this field but the underlying mechanism remains elusive. For instance, in the Bi_2Se_3/Py heterostructure where the SOT is measured by ST-FMR, the spin Hall angle θ_{SH} is determined to be 2.0-3.5 at room temperature. But in the BST/Cr-BST heterostructure in our previous work, the second harmonic measurements revealed $\theta_{SH} = 140 - 425$ at 1.9 K, which is almost two orders of magnitudes larger than the θ_{SH} measured by ST-FMR.[*44, 46*] Several other research groups also reported the measurement of SOT in TI via different approaches, *e.g.*, spin-pumping which estimated $\theta_{SH} = 0.005 - 0.4$ and hysteresis loop shift method which gave $\theta_{SH} = 0.15 - 0.4$.[*47, 48*] Such discrepancies exist even when the same measurement setup is employed for different TI samples.[*48*] Besides, a fundamental difference between TIs and heavy metals is that the spin polarization in TIs arises from the topologically protected TSS other than spin Hall effect. But so far there is little experimental evidence that directly elucidates the true origin of SOT in TI or the correlation between SOT and TSS before this dissertation work. Specifically, TSS is reported to be quite temperature-sensitive[*42, 43, 49*] and can be key issues in the application of TI-based magnetic memory devices, but the temperature dependence of SOT from TSS remains unclear.

In order to resolve the controversy over the size of θ_{SH} in TI and reveal the correlation between TSS and SOT, we comprehensively determined θ_{SH} in TIs by adopting multiple measurement techniques. Since we mainly investigated magnetic TI systems where the magnetization in TIs plays a key role in probing the SOT, the magnetic properties of TIs were firstly investigated. The study was carried out via two approaches, *i.e.*, magnetic proximity effect and magnetic doping with Cr. In the former approach, the proximity coupling between a TI and another ferromagnetic or ferrimagnetic material can give rise to a magnetic order in the TI layer. Specifically, a proximity-induced magnetic order was observed in a wet transferred TI/ferrimagnetic insulator heterostructure from anomalous Hall effect. We found that the magnetic order by proximity effect is very sensitive to the interface quality, where a thin AlO_x layer can block the proximity effect and eliminate the induced magnetization. However, the induced magnetization through this approach is quite weak and it is not a desirable method to measure SOT or magnetization switching. The latter approach is a more conventional method that utilizes Cr dopants to induce long-range ferromagnetic coupling inside TIs and offers more robust ferromagnetism with perpendicular anisotropy, which is suitable for high density memory applications utilizing the SOT from TIs. To quantify the SOT in TIs, we employed both hysteresis loop shift measurement and SOT magnetometer based on the magneto-optic Kerr effect (MOKE), where consistent results are obtained by these two approaches. Moreover, θ_{SH} from hysteresis loop shift measurements exhibits a drastic increase as the temperature decreases when the temperature is below 12 K. The sharp increase of θ_{SH} may be explained by a higher spin polarization ratio in

TSS at lower temperatures, where the electron-phonon scattering is greatly suppressed. Measurement of SOT is also carried out in a uniformly doped Cr-BST film, where devices are fabricated into a field-effect transistor (FET) geometry to tune the top TSS Fermi level (E_F). While the carrier concentration of the top TSS is modulated by electrostatic gating, the current-induced effective field can be effectively manipulated, revealing a competition between the top TSS and bottom TSS in the contribution to SOT. The strongly temperature- and carrier concentration-dependent SOT as well as the competition between the top and bottom TSS may be responsible for the wide discrepancies among the reported θ_{SH}.

2.2. Inducing Magnetic Order in Topological Insulators

2.2.1. Proximity-Induced Magnetic Order

To observe and measure SOT in a TI, first of all a magnetic order needs to be introduced, and an effective approach points to magnetic proximity effect by interfacing a TI thin film with a magnet insulator (MI). Magnetic proximity effect is a phenomenon that at the interface of a magnetic/non-magnetic material heterostructure, the magnetic layer can induce a magnetic order in the non-magnetic layer via orbital hybridization or exchange-coupling.[*50*] In a TI/MI heterostructure, magnetic exchange coupling at the interface can induce a magnetic order in the TI layer without the participation of dopants.[*51-55*] One of the suitable MI candidates points to yttrium iron garnet (YIG, $Y_3Fe_5O_{12}$), which is a ferrimagnetic insulator with a high Curie temperature (T_C) of ~ 550 K, and has been widely used in microwave and magneto-optical applications such as microwave filters and transducers. Figure 2-1(a) shows the magnetic hysteresis loop of a YIG film grown on gadolinium gallium garnet (GGG) substrate measured by MOKE. It manifests a pronounced magnetization at room temperature with a saturation field of ~0.2 T as shown by the hysteresis loop. The saturation magnetization of the YIG film was measured to be $M_s = 142\ emu/cc$ by SQUID, and it has a small coercivity field of $H_c = 5\ Oe$. Using YIG as substrates (lattice constant of a=12.376 Å, which is ~3 times the lattice constant of Bi_2Se_3, a=4.14 Å), our previous study on MBE-grown Bi_2Se_3/YIG heterostructures has demonstrated the signature of a proximity-induced magnetic order in the Bi_2Se_3 coupled to the YIG substrate (Figure 2-1(b)).[*53, 55-59*]. The proximity-induced out-of-plane magnetization breaks the time-reversal symmetry in TI and opens a small exchange-gap in the surface states Dirac cone, while at the domain boundaries the magnetization points to the in-plane direction and the surface states remain gapless.

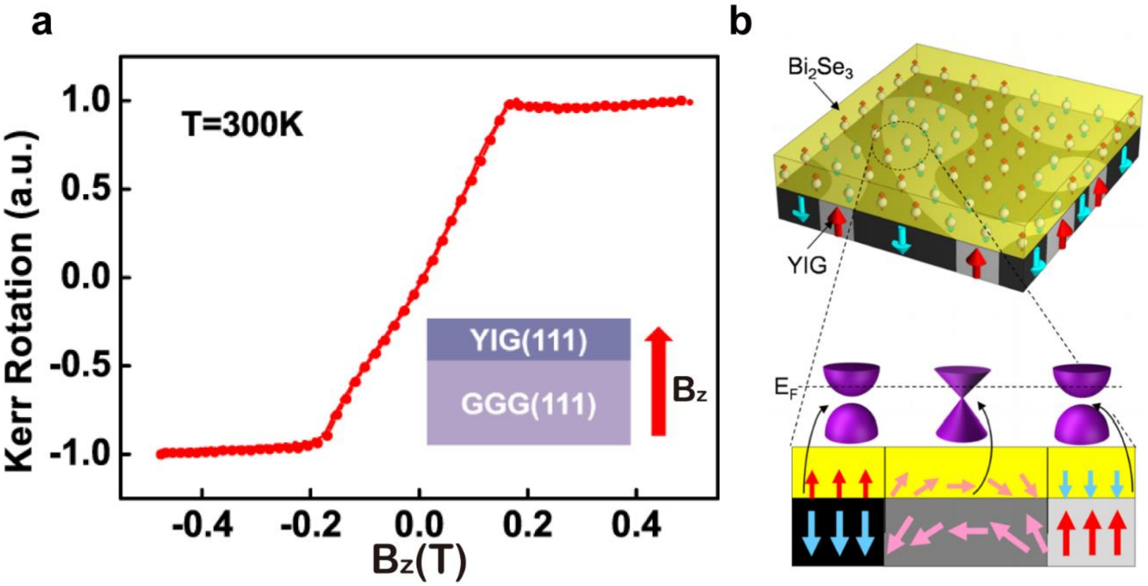

Figure 2-1. Inducing magnetic order in TI by magnetic proximity effect in a Bi_2Se_3/YIG heterostructure. (a) Magnetic hysteresis loop (out-of-plane direction) of a YIG film grown on a GGG substrate measured by SQUID at room temperature. (b) A Bi_2Se_3/YIG heterostructure grown by MBE and magnetization in the Bi_2Se_3 layer induced by the YIG substrate via magnetic proximity effect. Figure (b) adapted from Ref. [*56*].

So far, MBE-growth remains the only approach to preparing high-quality TI/MI heterostructures, but epitaxial growth may introduce a chalcogenide-rich dead layer during the annealing of seed layer under Se/Te fluxes owing to a large lattice mismatch[*60, 61*], which not only jeopardizes the quality of the film but also hinders the magnetic exchange coupling between the MI substrate and the time-reversal symmetry protected TSS above the dead layer. Magnetic impurities are also prone to diffuse into the TI layer from the MI substrate during this procedure. Moreover, MBE-growth of thin films severely relies on the requirement of lattice matching with the substrates, and the flexibility of MI substrates for the epitaxial growth of TIs is very limited. Similar to TIs, two-dimensional van der Waals materials cannot be epitaxially grown on arbitrary substrates, but the wide adoption of transfer techniques has offered many possibilities in engineering device structures. Therefore, we studied a TI/MI heterostructure prepared by transferring an MBE-grown Bi_2Se_3 film onto a YIG substrate via wet-transfer.

Previous studies suggest that Bi_2Se_3 grown on sapphire (0001) substrates by MBE not only is among the best in terms of film quality but also can be transferred onto other substrates with minimal degradation.[*62-67*] Here Bi_2Se_3 films were also grown on sapphire (0001) substrates for transfer. The thickness of the MBE-grown Bi_2Se_3 film was optimized to be 6 quintuple layers (QLs), in order to minimize the bulk conduction and at the same time avoid the hybridization gap opening in the surface Dirac cone.[*63, 68, 69*] The 2.3 μm-thick single-crystalline YIG was grown on a $Gd_3Ga_5O_{12}$ (GGG) (111) substrate by liquid phase epitaxy. The Bi_2Se_3 film was subsequently transferred to the prepared YIG substrate. As illustrated in Figure 2-2(a), the Bi_2Se_3/sapphire sample was firstly spin-coated with a thin polymethyl methacrylate (PMMA) layer once it was taken out of the MBE chamber. Then the whole sample was immersed in a KOH solution to initiate the exfoliation of the Bi_2Se_3 film from the sapphire substrate. When the Bi_2Se_3 film just started to detach from the sapphire substrate, the sample was removed from the KOH solution and left floating on freshly prepared DI water to complete the exfoliation. The partially detached Bi_2Se_3 film on DI water slowly got peeled off from the substrate, probably due to a tensile force exerted by the surface tension of water. After the detachment, the exfoliated Bi_2Se_3 film with PMMA coating was rinsed in DI water for 5 times. Finally, the Bi_2Se_3 film was fished out by the YIG substrate and dried up in N_2 ambient.

Figure 2-2(b) shows a picture of the transferred Bi_2Se_3 film on the YIG substrate. A visually smooth and continuous Bi_2Se_3 film is obtained, upon which the color gradient suggests the PMMA coating layer. The Bi_2Se_3 film remains largely intact after the transfer, as evidenced by the optical microscope image in Figure 2-2(c) after the removal of PMMA. The formation of a sharp interface between Bi_2Se_3 and YIG is further verified by cross-sectional scanning transmission electron microscope (STEM) imaging. As displayed in Figure 2-2(d), the quintuple-layer structure of Bi_2Se_3 with van der Waals gaps in between can be clearly noticed. The Bi_2Se_3/YIG interface is smooth and clean without any dead-layer. Energy-dispersive X-ray spectroscopy (EDX) was also conducted, concluding no signature of intermixing between Bi_2Se_3 and YIG.

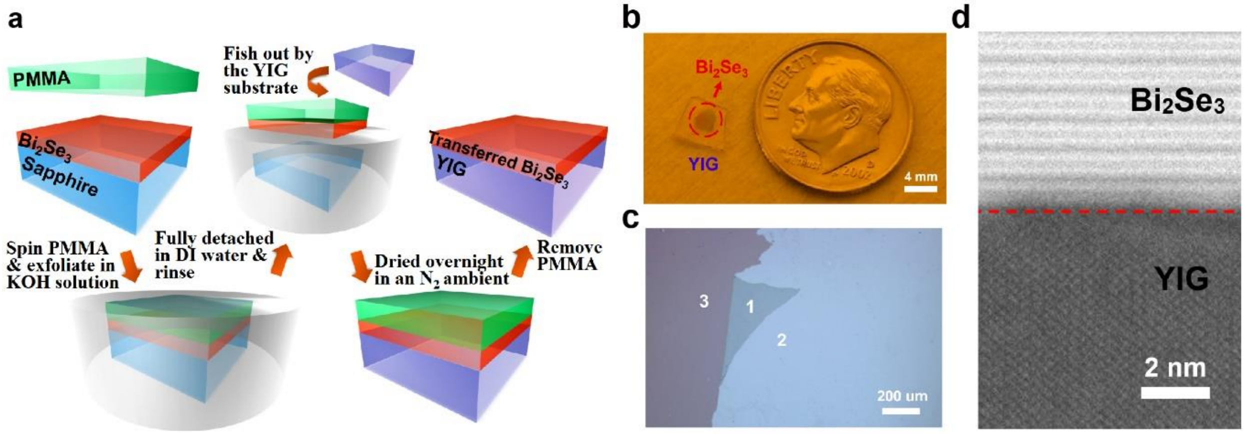

Figure 2-2. Transfer of a MBE-grown Bi_2Se_3 film onto a YIG substrate via wet transfer and characterizations after transfer. (a) Schematic illustration of the procedures in transferring the Bi_2Se_3 film. (b) An image of the TI/YIG before removing PMMA in comparison with a dime. (c) An optical microscope image of the transferred TI film on YIG, showing a smooth and crack-free surface. (d) High-angle annular dark-field scanning transmission electron microscopy (HAADF-STEM) image of the TI/YIG, revealing a high crystallinity and a clean interface. Figure (a)-(d) adapted from Ref. [*70*].

To systematically study the interfacial proximity coupling under different interface conditions as well as to realize a better comparison, three samples were prepared in our experimental design, which are Bi_2Se_3/YIG (BS1), Bi_2Se_3/YIG with a thin AlO_x insertion layer (BS2), and Bi_2Se_3/GaAs (BS3) (see Figure 2-3(a)). All three samples were prepared through the same transfer procedures. Particularly, in BS2 the AlO_x insertion layer was inserted by depositing a 0.7 nm-thick Al on the YIG substrate using electron-beam evaporation, after which it naturally oxidized into AlO_x with a thickness of about 1 nm. In principle, single-crystalline Bi_2Se_3 cannot be epitaxially grown on amorphous AlO_x. But by exfoliation, we avoid heterostructure growth and are able to engineer the trilayer structure despite the amorphous AlO_x layer. Here the Bi_2Se_3 films on all these samples were transferred from the same Bi_2Se_3/sapphire sample (BS0), which offers better quality control among different samples. All samples were patterned into devices with Hall bar geometry through standard photolithography (see the inset of Figure 2-3(b)).

Magneto-transport measurements with perpendicular external magnetic field were subsequently carried out to investigate the magnetic proximity effect. For all three samples, the Hall effect curves display negative slopes due to the n-type nature of Bi_2Se_3 as shown in the inset of Figure 2-3(b). The extracted 2D carrier concentrations n_{2D} of the Bi_2Se_3 layer are $8.7 \times 10^{12} \mathrm{cm}^2$, $8.9 \times 10^{12} \mathrm{cm}^2$, and $3.9 \times 10^{13} \mathrm{cm}^2$ for BS1, BS2, and BS3, respectively. It is interesting that the carrier concentration of the transferred Bi_2Se_3 film is comparable or even lower than the as-grown Bi_2Se_3/sapphire sample ($4.1 \times 10^{13} \mathrm{cm}^2$), suggesting almost no impact from the environmental doping (mostly n-type from oxygen) on the Bi_2Se_3 film during the transfer. A plausible mechanism for the lower carrier concentration in BS1 and BS2 may be due to interfacial charge transfer or neutralization of surface charge defects, which were reported in transferred Bi_2Se_3 films.[*66*] After removing the linear Hall background, it becomes clear that BS1 displays a distinct anomalous Hall curve with a saturation behavior at ~ 0.2 T, while such behavior is not observed for both BS2 and BS3. The anomalous Hall effect in the Bi_2Se_3 may originate from an interfacial proximity-induced magnetic order, which can be further explained as the hybridization between the *p*-orbital of Bi_2Se_3 and the *d*-orbital of Fe in YIG at the interface. Meanwhile, it is noticed that the ~1 nm AlO_x layer separating Bi_2Se_3 and YIG basically obstructs the interfacial proximity coupling as anomalous Hall signal is no observed for BS2. This suggests the crucial role of a sharp Bi_2Se_3/YIG interface in inducing a magnetic order in Bi_2Se_3 through proximity effect.

Figure 2-3(c) shows the temperature-dependent anomalous Hall effect curves in BS1 under perpendicular magnetic field after subtracting the ordinary Hall background. The anomalous Hall resistance reaches its maximum of ~ 2.8 Ω at 1.9 K, slowly decreases as temperature increases, and eventually vanishes ~ 30 K. A natural question may arise that the T_C of the Bi_2Se_3 layer seems to be much lower than that of the YIG substrate (~ 550 K). In fact, both T_C much lower than that of the magnetic substrate and T_C well above room temperature have been reported from the magnetic proximity effect in TI.[*53, 56, 71*] While the underlying mechanism is yet unclear, it is reasonable that the induced magnetic order is not as strong as the exchange interaction in the interior of YIG. Moreover, the induced magnetic order also suffers from finite-size effect, imperfections at the interface, and sample-to-sample variations, which may account for the low T_C in this system. The anomalous Hall signal of the Bi_2Se_3 layer is similar to the magnetic hysteresis of the YIG substrate along the out-of-plane direction measured by the magneto-optical Kerr effect (see the inset of Figure 2-3(c)), again suggesting the proximity coupling between Bi_2Se_3 and YIG. No obvious coercivity is observed in the Bi_2Se_3 layer, since YIG is a soft magnetic material with almost zero coercivity in its magnetic hysteresis.[*50, 72, 73*]

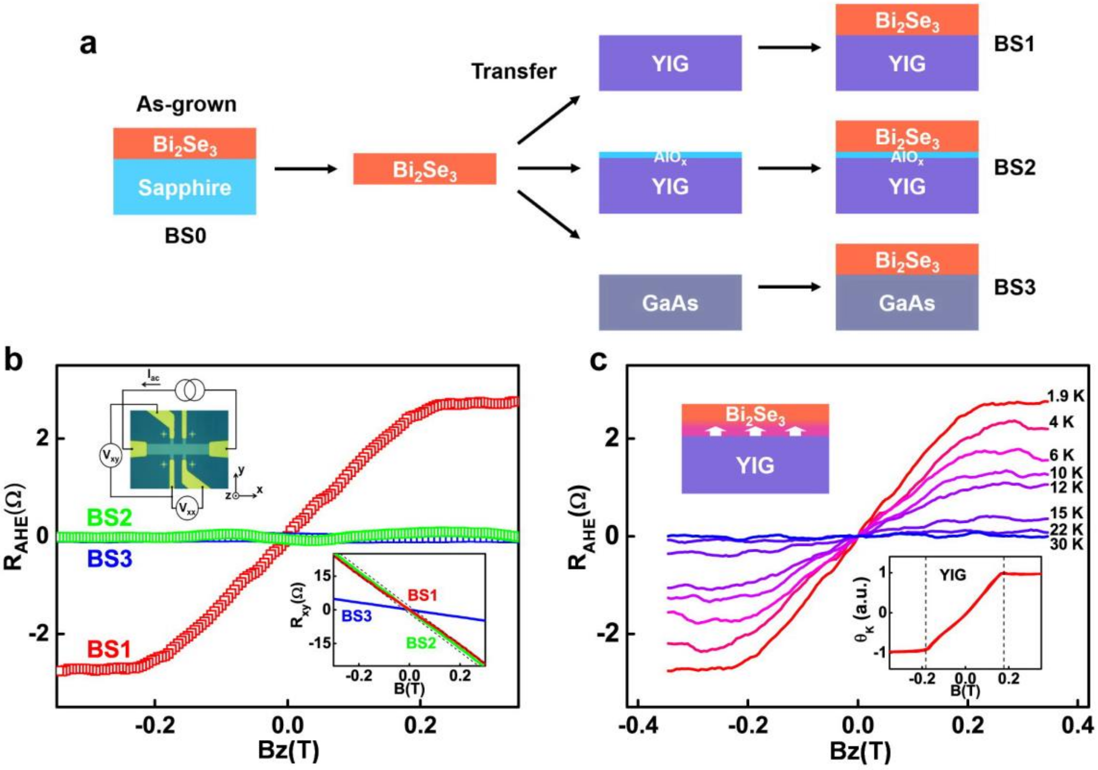

Figure 2-3. A comparative study of the Hall effect in the Bi_2Se_3 samples with different device structures. (a) Three distinct sample structures prepared by the same wet-transfer procedures, named as BS1 (Bi_2Se_3/YIG), BS2 (Bi_2Se_3/AlO_x/YIG) and BS3 (Bi_2Se_3/GaAs), respectively. (b) Hall measurement results of the three samples at 1.9 K after subtracting the linear background. BS1 displays a nonlinear Hall signal with a saturating behavior at ~0.2 T compared to BS2 and BS3. Inset 1: Device geometry for magneto-transport measurements with a schematic of the instrument setup. Inset 2: Hall measurement results of the three samples at 1.9 K before subtracting the linear background (c) Anomalous Hall resistance of BS1 at different temperatures. Inset 1: A schematic illustrating the interfacial magnetic proximity effect in BS1. Inset 2: Normalized out-of-plane magnetic hysteresis loop of YIG measured by MOKE at 300 K. Figure (a)-(c) adapted from Ref. [*70*].

2.2.2. Ferromagnetism Introduced by Cr Doping

For the TI/YIG heterostructure demonstrated in the previous section (2.2.1), it can be noticed from the hysteresis loops that the magnetic order is soft and lacks adequate perpendicular magnetic anisotropy, as there is no obvious coercivity in the out-of-plane hysteresis loops. This can be attributed to the in-plane magnetic anisotropy of the YIG substrate, which is not capable of inducing a robust perpendicular magnetization via magnetic proximity effect. Because of this, the induced magnetization in TI by proximity effect is weak as can be seen from the small anomalous Hall resistance in Hall measurement (~2.5 Ω at 1.9 K). Such weak magnetization will strongly hinder the determination of SOT in TI, since the reorientation of magnetization by SOT can be subtle and the determination of SOT heavily relies on the accurate detection of small magnetic dynamics. It will be challenging to measure SOT by either transport method or optical method with a small proximity-induced magnetization. Besides, the switching of magnetization between 'up' and 'down' states in the out-of-plane direction is preferred for high-density applications. Thus, a perpendicular magnetic anisotropy of the magnetization is required.

A more widely adopted approach to induce magnetic order into TIs is introducing transitional metal elements such as Fe, Co and Cr as magnetic dopants, similar to the approach adopted in the study of diluted magnetic semiconductor.[*74-76*] Among them, Cr has been demonstrated to be an effective dopant to introduce robust long-range ferromagnetism in TIs. Our lab has rich experience in growing Cr-doped BST films by MBE with high quality and pronounced ferromagnetism.[*75*, *77*, *78*] Figure 2-4(a) shows a cross-sectional STEM image of a Cr-doped BST film with high quality grown on a GaAs substrate in our previous study. A clear quintuple-layer structure with van der Waals gaps in between can be observed. Besides, the EDX image reveals a uniform distribution of the Cr atoms throughout the BST film. Ferromagnetism with a large coercivity and perpendicular anisotropy was observed in the Cr-BST film from Hall measurement in Figure 2-4(b). The coercivity decreases as temperature increases and vanishes ~30 K. Such robust ferromagnetism may be measured under SOT to demonstrate magnetization switching devices.

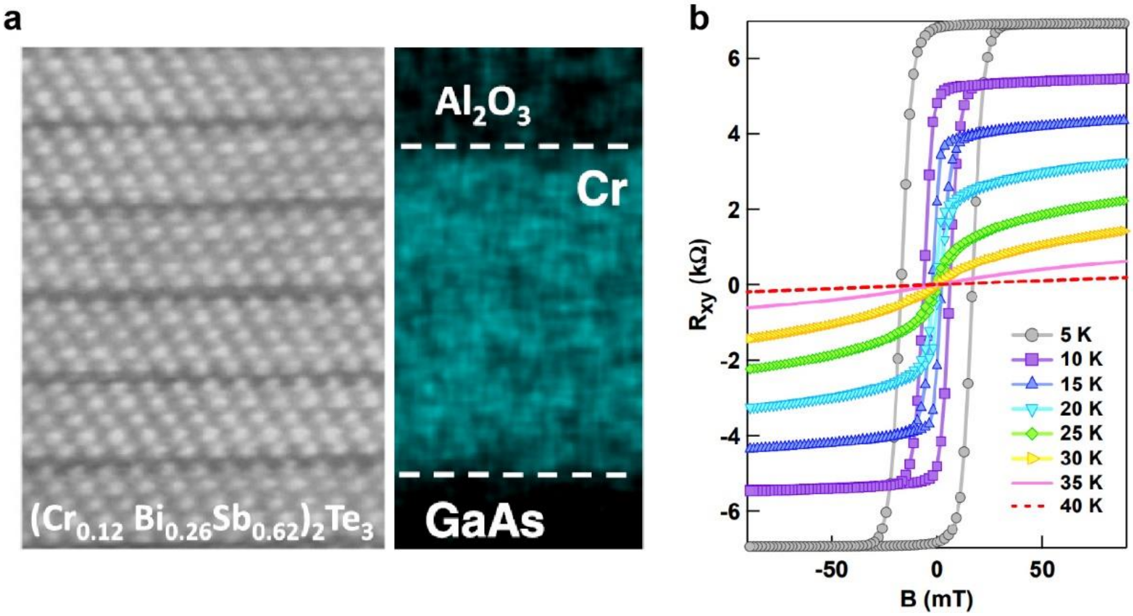

Figure 2-4. Doping TI with Cr in MBE growth and magnetization of a Cr-doped BST film. (a) TEM image of a Cr-doped BST film on GaAs substrate by MBE growth. The Cr-doped BST film shows high quality, and Cr dopant distributed uniformly in the BST film from the EDX image (b) Magnetic hysteresis loop of the Cr-doped BST film at different temperatures from Hall measurements. The Cr-doped BST film exhibits a pronounced ferromagnetism with a large coercivity at 5 K and a Curie temperature T_c of ~30 K. Figure (a) and (b) adapted from Ref. [*77*].

For this thesis, we prepared a modulation-doped Cr-BST/BST bilayer film as illustrated in Figure 2-5(a) to examine its magnetic properties before measuring SOT. The Cr-BST/BST heterostructure was grown on an insulating GaAs (111) B substrate by molecular beam epitaxy (MBE) in an ultra-high vacuum environment (~10^{-9} Torr). The bottom layer of the TI film is not magnetically doped and has a thickness of 2 quintuple layers (QLs), while the top layer is Cr-doped with a thickness of 5 QLs. The bilayer film was then fabricated into devices with a Hall bar geometry by standard photolithography for magneto-transport and magneto-optic measurements. Hall measurements were carried out at different temperatures to check the magnetic property. As shown in Figure 2-5(b), the bilayer film exhibits a robust magnetic order with an obvious coercivity at different temperatures below 17 K. The magnetic order of the Cr-BST develops at a relatively low temperature due to a low T_c of magnetically doped TIs ($T_c \approx 30\ K$).[77] Superconducting quantum interference device (SQUID) measurement was also carried out in vibration sample magnetometry (VSM) mode at different temperatures to investigate the Cr-BST/BST bilayer film. Figure 2-5(c) shows the magnetic hysteresis loop measured by sweeping an out-of-plane magnetic field at 2 K, where it can be noticed that the out-of-plane magnetization of the bilayer film becomes saturated when $H_z = 5\ kOe$. The saturation magnetization M_s was plotted in Figure 2-5(d) for different temperatures. The established magnetization in the Cr-BST/BST bilayer film shows $M_s = 35\ emu/cc$ at 2 K, and M_s weakens as temperature increases and vanishes around 30 K, again indicating its $T_C \approx 30\ K$.

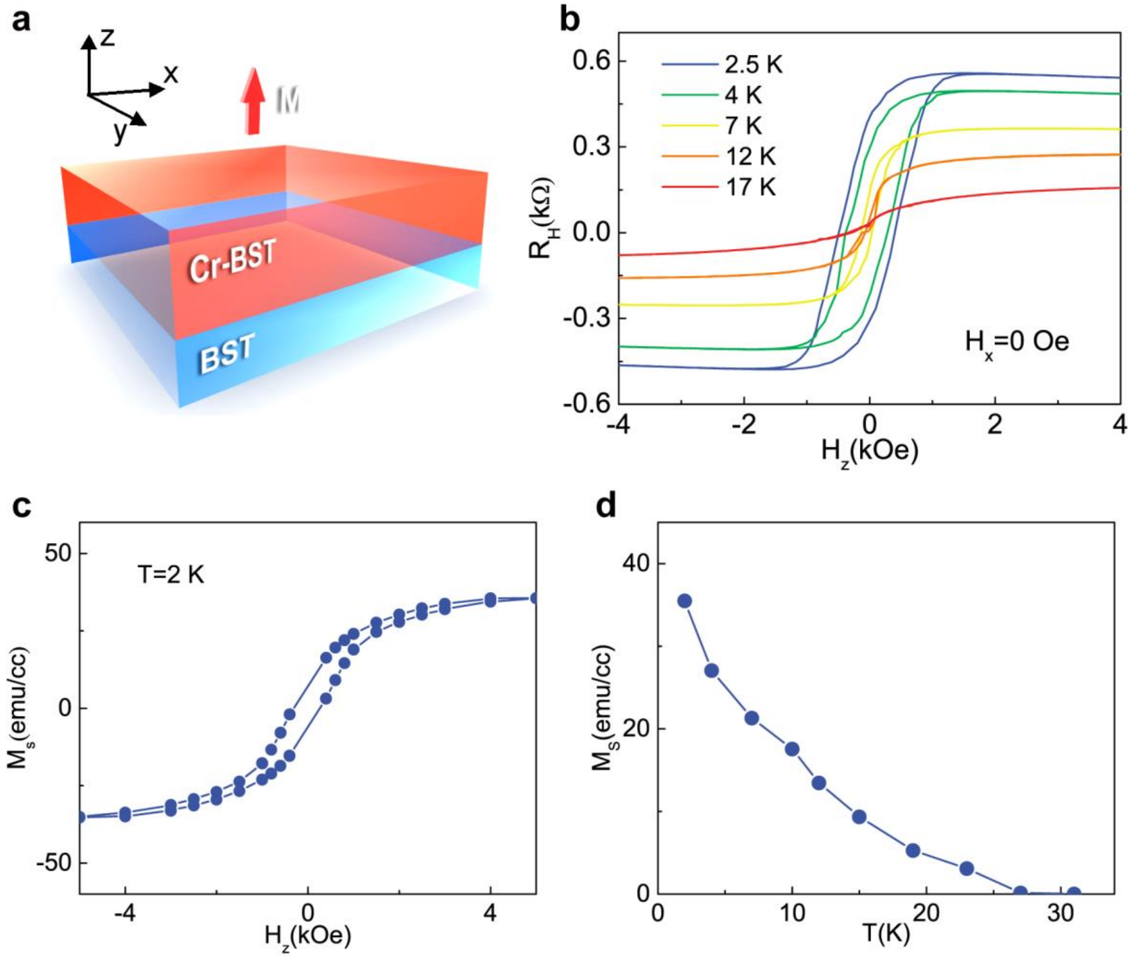

Figure 2-5. Magnetization in a Cr-doped BST/BST heterostructure. (a) Schematic illustration of the Cr-BST/BST bilayer film with perpendicular magnetic anisotropy. (b) Out-of-plane magnetic hysteresis loops of the bilayer sample by Hall measurements at different temperatures. (c) Out-of-plane magnetic hysteresis loop of the Cr-BST/BST bilayer film at 2 K measured by SQUID. (b) Saturation magnetization M_s measured between 2 K and 32 K. M_s reaches the highest value of 35 emu/cc at 2 K and approaches 0 at 30 K. Figure (b)-(d) adapted from Ref. [*79*].

2.3. Experimental Determination of Spin-Orbit Torque

2.3.1. Measuring Spin-Orbit Torque by Hysteresis Loop Shift Method

In the previous section (2.2.2), we have examined the magnetic properties of the Cr-BST/BST bilayer film by both transport and SQUID. It can be confirmed that the Cr-BST/BST bilayer film has a robust ferromagnetism with perpendicular magnetic anisotropy. Therefore, this material system can be suitable for SOT measurement and perpendicular magnetization switching test for potential memory applications. In this section, we determine the SOT in this system with different measurement methods. We first employed the current-induced hysteresis loop shift method to investigate the SOT. This measurement approach utilize the shift of the magnetic hysteresis loop under DC current due to the effective field to quantitatively measure the SOT. Experimental details of this technique are explained below with the schematic illustration in Figure 2-6(a).

In the Cr-BST layer, Néel-type domain walls form during the magnetization reversal process as a result of the interfacial Dzyaloshinskii-Moriya interaction (DMI). Generally, DMI exists in B20-type ferromagnetic materials with a particular crystal symmetry, which is known as bulk DMI. It also exists at the interfaces of HM/FM heterostructures due to the breaking of inversion symmetry and the SOC of the HM layer, known as interfacial DMI.[*80*] Similar to HM/FM heterostructures, in a Cr-BST/BST bilayer film the inversion symmetry is broken at the interface, and the SOC from TI is strong enough to induce interfacial DMI that promotes the stabilization of Néel-type domain walls.[*81, 82*] When a DC current is applied on the device, the top TSS exerts a damping-like SOT $\boldsymbol{\tau}_{\perp}$ proportional to $\boldsymbol{m} \times (\boldsymbol{m} \times \boldsymbol{\sigma})$ on the magnetization in the Cr-BST layer, which is equivalent to a spin-orbit effective field $\boldsymbol{H}_{\boldsymbol{z}}^{\boldsymbol{eff}}$ proportional to $\boldsymbol{m} \times \boldsymbol{\sigma}$. Here

$\boldsymbol{\sigma}$ represents the spin magnetic moments in TSS and $\boldsymbol{m}$ is the unit vector denoting the Cr-BST magnetization direction. The directions of damping-like torque and field-like torque on a magnetic moment have been discussed in Chapter 1.1 (see Figure 1.1b). Here, the damping-like torque can induce the switching of perpendicular magnetization, while the field-like torque primarily contributes to the magnetization reorientation in the in-plane direction. Specifically, in the domain walls $\boldsymbol{m}$ lies in the in-plane direction with the local anisotropy pointing along the *x*-axis characterized by the DMI effective field $\boldsymbol{H_{DMI}}$. In the measurement, an in-plane bias field $\boldsymbol{H_x}$ along the *x*-axis is required to overcome $\boldsymbol{H_{DMI}}$ and align the magnetic moments in different domain walls towards the same direction as shown in Figure 2-6(a). In this scenario, the effective field either facilitates or suppresses the domain wall expansion process and causes a horizontal shift of the hysteresis loop in the anomalous Hall resistance plot. Hence, the effective field can be directly quantified from the shift of the hysteresis loop. It should be noted that in this bilayer system, we presume that the SOT primarily originates from the top TSS since it is much closer to the magnetization in the Cr-BST layer compared to the bottom TSS and overwhelms the SOT from the bottom TSS.[*44*]

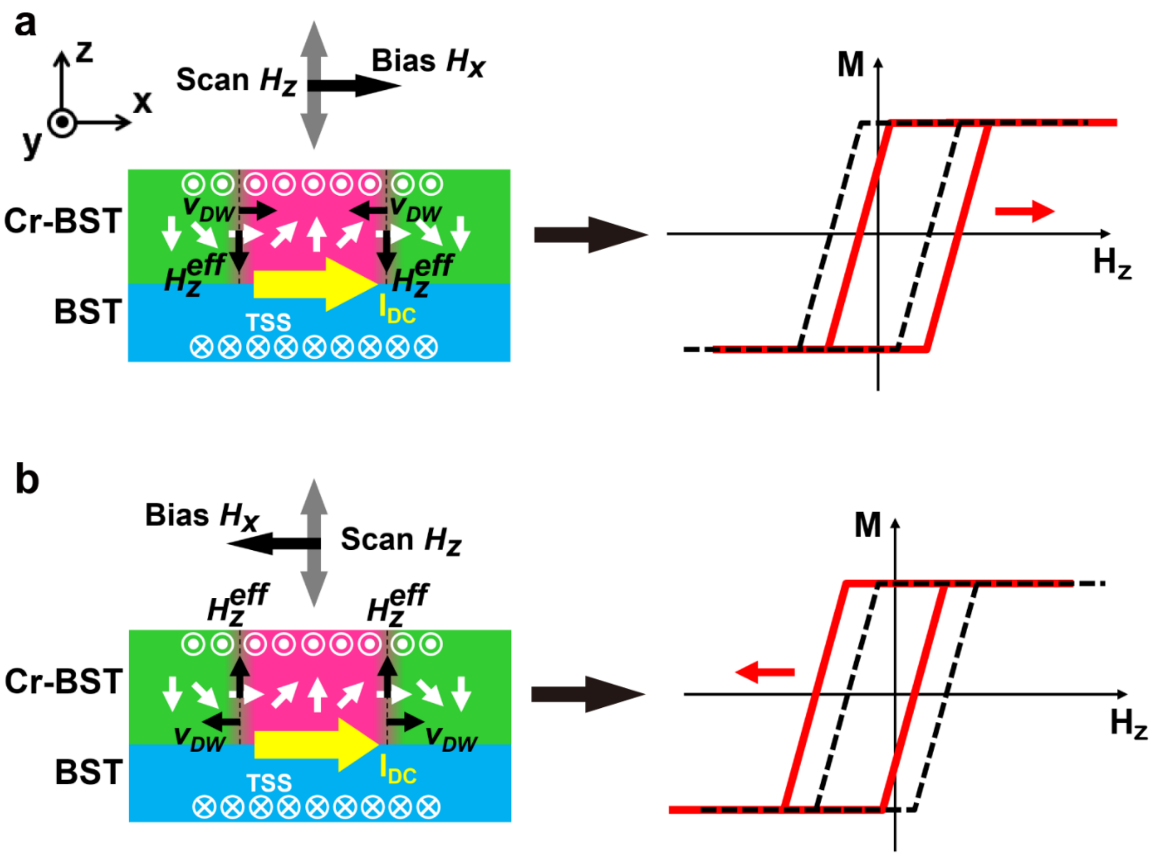

Figure 2-6. Hysteresis loop shift driven by current-induced SOT. (a) Schematic of the domain wall spin texture in the Cr-BST layer under a positive in-plane bias field $\boldsymbol{H_x}$ and a perpendicular scanning field $\boldsymbol{H_z}$. A damping-like effective field $\boldsymbol{H_z^{eff}}$ (see illustration of $\boldsymbol{H_z^{eff}}$ in Figure 1.1b and discussion in Chapter 1.1) proportional to $\boldsymbol{m} \times \boldsymbol{\sigma}$ is exerted on the spins in the domain wall by the damping-like torque from TI, causing the hysteresis loop shift toward the right direction. (b) Schematic of the domain wall spin texture under a negative in-plane bias field $\boldsymbol{H_x}$ and a perpendicular scanning field $\boldsymbol{H_z}$. The damping-like effective field $\boldsymbol{H_z^{eff}}$ points to +z direction and shifts the hysteresis loop toward the left direction.

The hysteresis loop shift method has been demonstrated to be an effective approach in quantifying the SOT efficiency in both HM/FM system and TI/FM system.[*47*, *83*] However, this approach needs an in-plane field and an out-of-plane field that are simultaneously generated. Such requirement poses a limitation in the measurement because in most of the magneto-transport measurement setups there is only one set of magnetic coil in the instrument. In order to circumvent this hardware limitation, we employ an alternative technique to carry out the hysteresis loop shift measurement by utilizing the rotation functionality in our instrument as displayed in Figure 2-7. In the measurement, the total external field $\boldsymbol{H}$ is simply a vector sum of the in-plane field $\boldsymbol{H_x}$ and the out-of-plane field $\boldsymbol{H_z}$ as $\boldsymbol{H} = \boldsymbol{H_x} + \boldsymbol{H_z}$. Consequently, the two separate external magnetic fields can be replaced by one external field while both its magnitude H and its angle to the x-axis θ are modulated simultaneously. Since the key of the hysteresis loop shift method in determining SOT is maintaining a constant H_x to overcome H_{DMI}, the magnitude of the applied magnetic field is set to be $H = H_x/cos(\theta)$ where H_x is a preset constant value. In the meantime, $\boldsymbol{H}$ provides an out-of-plane component of $H_z = H_x tan(\theta)$. Next, we scan H_z to obtain the magnetic hysteresis loop, which is accomplished by taking multiple data points under different combinations of H and θ. These data points constitute a complete hysteresis loop with a saturated anomalous Hall resistance R_{AHE}, equivalent to the hysteresis obtained under a sweeping H_z and a constant H_x.

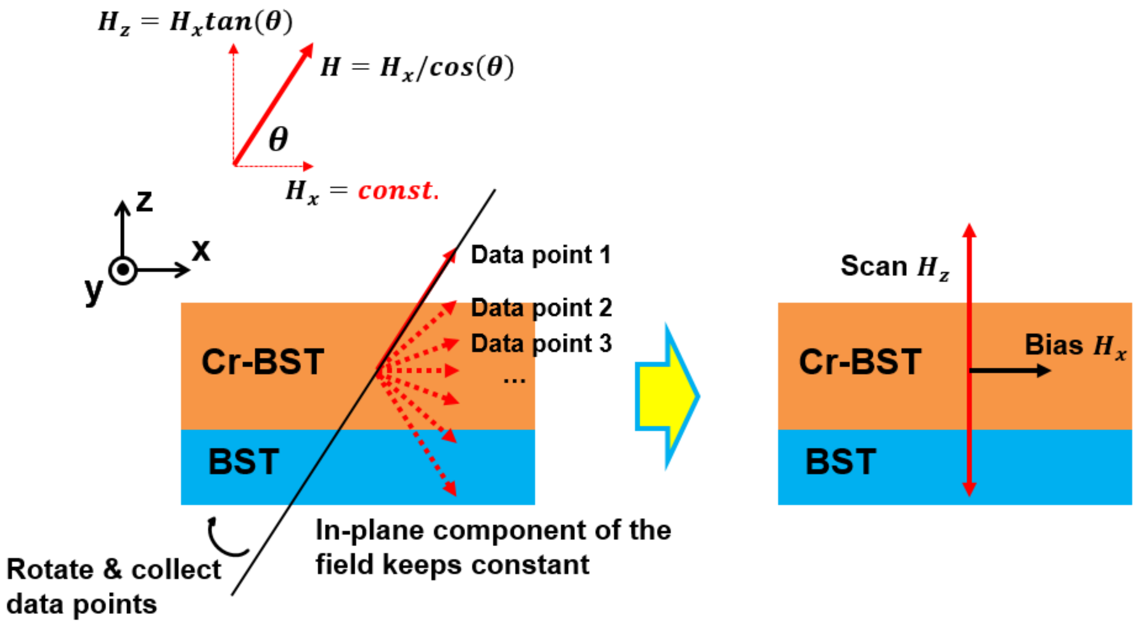

Figure 2-7. An alternative technique to perform the SOT measurement by hysteresis loop shift method without the requirement of two separate external fields. The Cr-BST/BST bilayer sample was rotated in the *xz* plane under an external magnetic field *H*. While the in-plane component of the external field H_x maintains a constant value, the applied total external field can be expressed as $H = H_x/cos(\theta)$ and the out-of-plane component will be $H_z = H_x tan(\theta)$. Data points are collected at different combinations of certain H and angle θ, resembling a changing H_z and a constant in-plane bias H_x. Figure adapted from Ref. [79].

Now that the hysteresis loop shift method is feasible with our experimental setup, the measurement of SOT utilizing this technique was carried out for the Cr-BST/BST sample. The shift of the anomalous Hall hysteresis loop at 7 K as a result of $\boldsymbol{H_z^{eff}}$ is shown in Figure 2-8(a). It can be seen that, under a positive in-plane bias field of $H_x = 5$ kOe, the reversal of the DC current direction causes the hysteresis loop shifting toward the opposite direction owing to a sign change of H_z^{eff}. Furthermore, if $\boldsymbol{H_x}$ is negatively biased while the current direction remains unchanged, the hysteresis will also have a reversed shift direction as a result of an opposite $\boldsymbol{m}$ at the domain walls and a sign change of H_z^{eff} (Figure 2-8(b)). From the hysteresis loop shift, H_z^{eff} can be determined as $H_z^{eff} = -(H_z^{+} + H_z^{-})/2$, where H_z^{+} and H_z^{-} represent the shift of the positive switching field and the negative switching field in the hysteresis loop, respectively. Here an effective field of $H_z^{eff} \approx 143$ Oe is extracted under a current density of $J_c = \pm 2.86 \times 10^4\ A \cdot cm^{-2}$.

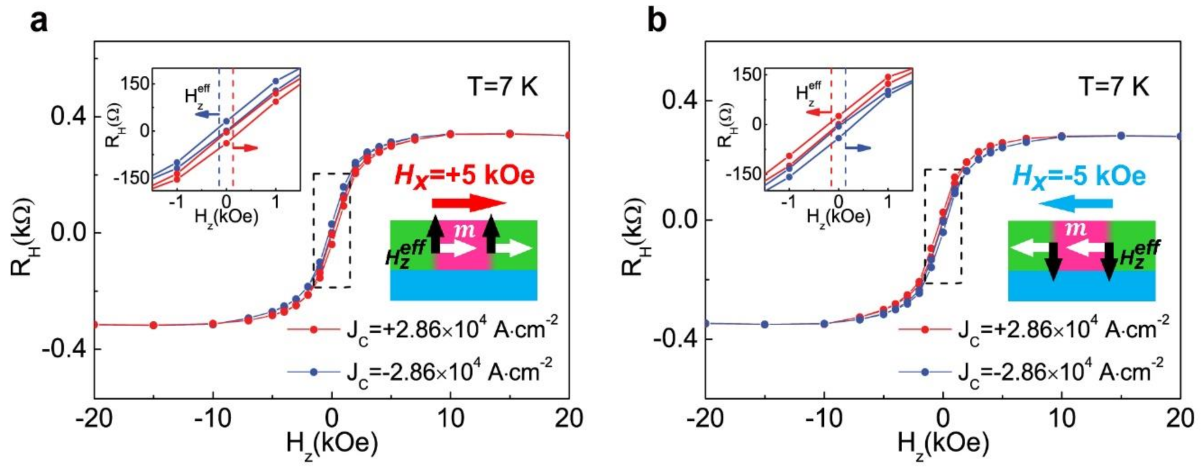

Figure 2-8. Determining SOT in the BST/Cr-BST heterostructure by hysteresis shift measurement. (a) Shift of the out-of-plane magnetic hysteresis loop as a result of $\boldsymbol{H_z^{eff}}$ in the Hall measurement for the bilayer sample. The measurements were carried out at 7 K under a positive in-plane bias field $H_x = +5$ kOe. Insets: zoomed-in images of the hysteresis loops and the current-induced effective field on the domain wall spins when a positive current is applied. (b) Shift of the out-of-plane magnetic hysteresis loop as a result of $\boldsymbol{H_z^{eff}}$ in the Hall measurement for the bilayer sample under a negative in-plane bias field $H_x = -5$ kOe. The hysteresis loop shift has an opposite shift direction comparing to (a) due to the reverse of H_x. Insets:

zoomed-in images of the hysteresis loops and the current-induced effective field on the domain wall spins when a positive current is applied. Figure (a) and (b) adapted from Ref. [*79*].

Here we use a term called SOT efficiency χ to quantify the strength of SOT in a system, defined as $\chi = H_z^{eff}/J_c$. From the above data it is calculated that $\chi \approx 5 \times 10^{-3}\ Oe \cdot A^{-1} \cdot cm^2$ under $H_x = 5\ kOe$ at 7 K. However, the experimentally measured value of χ could be smaller than its real value if the domain wall magnetic moments are not fully aligned in the same direction. It is not physically meaningful until H_x is sufficiently large to overcome the DMI effective field H_{DMI}. Therefore, a series of measurements with different applied H_x were carried out to further determine the intrinsic value of χ, which can be referred to as the saturated value χ^{sat}. The evolution of χ under an increasing in-plane field H_x is shown in Figure 2-9(a). It first increases when $H_x \leq 5\ kOe$ and eventually reaches $\chi^{sat} = (4.5 \pm 0.67) \times 10^{-3}\ Oe \cdot A^{-1} \cdot cm^2$ when $H_x \geq 5\ kOe$. The saturation field in turn reveals $H_{DMI} = 5\ kOe$ for the bilayer TI. The value of H_{DMI} can be of significance in the study of Skyrmions and topological Hall effect in TI systems.[*81, 82, 84*]

The evolution of χ is further investigated to understand the temperature dependence of SOT in TI. As plotted in Figure 2-9(b), χ at different temperatures exhibit a saturation behavior as H_{DMI} is overcome by H_x, and both H_{DMI} and χ^{sat} significantly vary with temperatures, which are further determined in Figure 2-9(c). It can be seen that both H_{DMI} and χ^{sat} increase rapidly as the temperature decreases from 12 K to 2.5 K. Here the diminishing H_{DMI} at elevated temperature can be explained by a less pronounced magnetization in the Cr-BST layer, since the Cr-BST has a relatively low T_c of ~30 K. The small H_{DMI} at elevated temperature also explains why topological

Hall effect in magnetic TI system is only observed at low temperatures.[*81, 82*] More importantly, χ^{sat} shows an increase of almost 2 orders of magnitude to $(2.7 \pm 0.6) \times 10^{-2}\ Oe \cdot A^{-1} \cdot cm^2$ at 2.5 K comparing to $(6.7 \pm 0.7) \times 10^{-4}\ Oe \cdot A^{-1} \cdot cm^2$ at 12 K in Figure 2-9(d). Such a sharp increase of χ^{sat} reveals a significant enhancement of SOT in TI at low temperatures. Because χ^{sat} also depends on M_s and the thickness of the magnetic layer t_{FM}, the dimensionless spin Hall angle θ_{SH} is a better term to quantify the intrinsic SOT in a material system. The relationship between θ_{SH} and χ^{sat} can be described by[*17*]

$$\theta_{SH} = \frac{4e\mu_0 M_s t_{FM} \chi^{sat}}{\hbar\pi} \qquad (2-1)$$

It should be noted that for heavy metal systems, electron transport is usually treated as 3D, while for TI the TSS are actually 2D sheets of carriers. In order to address such difference for better clarity, we use the term θ_{SH}^{3D} for spin Hall angle and we also use the 2D interfacial charge-to-spin conversion efficiency term q_{ICS}^{2D} defined as follows[*85, 86*]

$$\theta_{SH}^{3D} = \frac{J_s^{3D}}{J_c^{3D}} = \frac{J_s^{3D}}{J_c^{2D}} \cdot t_s = q_{ICS}^{2D} \cdot t_s \qquad (2-2)$$

where J_s^{3D} is the spin current density, J_c^{3D} is the charge current density, J_c^{2D} represents the 2D charge current density of the TSS, t_s denotes the effective thickness of TSS or the spin diffusion length. The determination of θ_{SH}^{3D} as well as the correlation between θ_{SH}^{3D} and temperature will be further discussed in the next section.

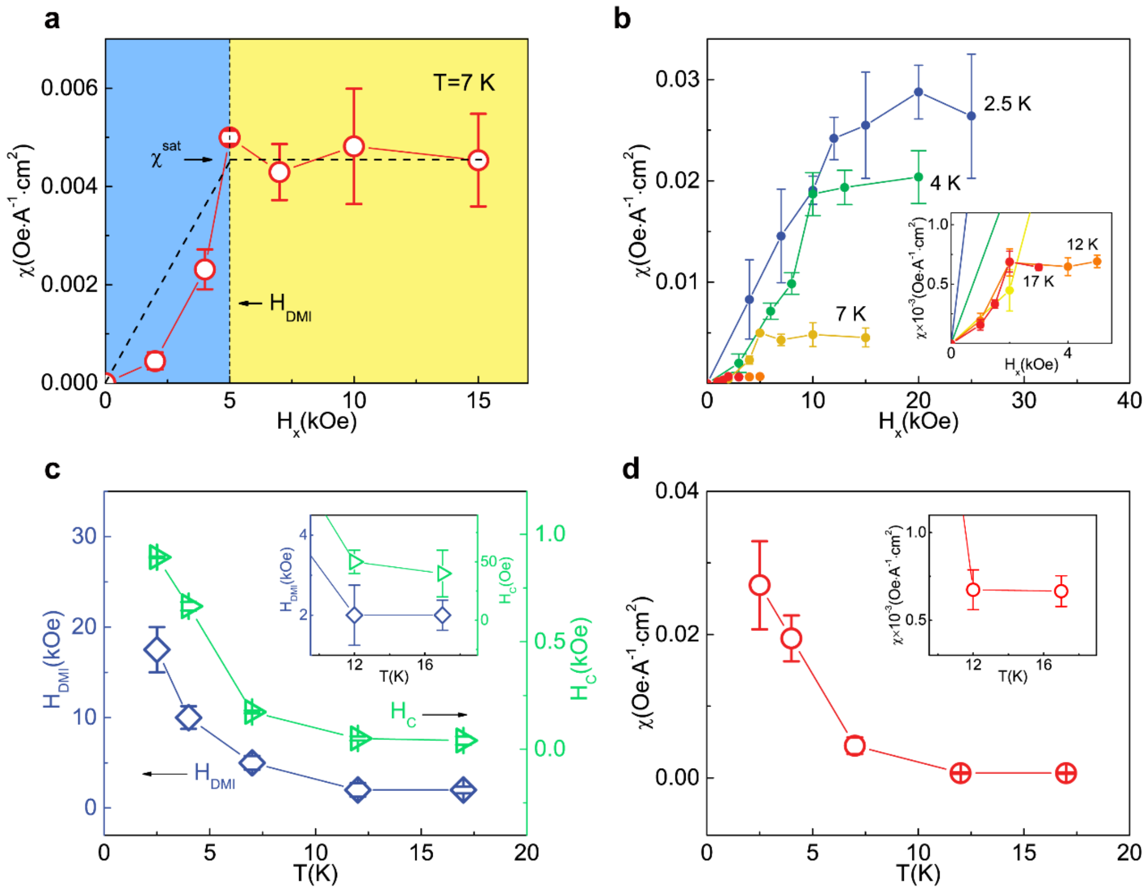

Figure 2-9. Quantifying the SOT efficiency χ and the DMI effective field H_{DMI} in Cr-BST/BST at different temperatures. (a) SOT efficiency χ extracted from the shift of the hysteresis under different bias field $\boldsymbol{H_x}$ at 7 K, where χ reaches its saturation value χ^{sat} when $\boldsymbol{H_x}$ overcomes the DMI effective field $\boldsymbol{H_{DMI}}$. (b) Evolution of χ under an increasing H_x at different temperatures. χ exhibits a saturation behavior at every temperature when adequate $\boldsymbol{H_x}$ is applied. Inset: Zoomed-in figure of the curves at 12 K and 17 K. (c) Temperature dependence of the $\boldsymbol{H_{DMI}}$ in comparison with the coercivity of the out-of-plane hysteresis. Inset: Zoomed-in figure of the data points at 12 K and 17 K. (d) Sharp decrease of the χ^{sat} as the temperature increases from 1.9 K to 16 K. Inset: Zoomed-in figure of the data points at 12 K and 17 K. Figure (a)-(d) adapted from Ref. [*79*].

2.3.2. Measuring Spin-Orbit Torque by Magneto-Optic Kerr Effect

As mentioned at the beginning of this chapter, though the variation of material compositions and sample qualities in TI-based systems may contribute to the large discrepancies among the reported θ_{SH}^{3D}, different experimental approaches could also be accounted for the deviations. Therefore, it is necessary to adopt another independent method to corroborate the measured SOT, and MOKE measurement has been demonstrated to be an effective approach in optically quantifying the strength of SOT in a previous report from our lab (DRL). The details of the experimental setup are demonstrated in Ref [*87*]. In this measurement method, magnetization and its dynamics are captured optically by the polarization of light through the Kerr effect. Figure 2-10(a) shows the mechanism of the Kerr effect, or more specifically, polar MOKE if the surface magnetization of the sample is pointing to the out-of-plane direction. The magnetization of the material gives rise to an anisotropic permittivity $\boldsymbol{\varepsilon}$ due to the off-diagonal components of the dielectric tensor. When light is reflected from the magnetized surface, it will obtain an additional phase after incidence because of the anisotropic permittivity and change its polarization. Thus, magnetization can be quantitatively characterized via the change of the polarization, *i.e.*, Kerr rotation θ_K.

During the measurement of SOT via MOKE, the magnetization of the sample is firstly aligned toward the in-plane direction by an external field H_x. When an AC current is applied, the alternating current amplitude drives a modulated SOT with the same frequency on the magnetization, causing it to oscillate periodically around its equilibrium state (Figure 2-10(b)). The magnetization oscillation in the out-of-plane direction can be approximated as Δm_z.The set-up of our MOKE-based magnetometer adopts a nearly normal incidence and reflection configuration. With a linearly polarized laser beam focused perpendicularly onto the sample surface as shown in Figure 2-10(c) and (d), the magnetization and SOT-related dynamics is captured by the changes in polarization plane of the laser reflected from the sample surface. Since θ_K captures the out-of-plane component, longitudinal component and transverse component of magnetization, it is described by[*87*]

$$\theta_K = f_{\perp} m_z + f_{\parallel} m_t m_l \qquad (2-3)$$

where m_z is defined as the out-of-plane component of $\boldsymbol{m}$, m_t and m_l are the longitudinal and transverse in-plane components of $\boldsymbol{m}$ with respect to the polarization plane of laser; $f_{\perp}$ and $f_{\parallel}$are the first- and second-order dimensionless coefficients that parameterize the coupling between the light and magnetic moments. With this formulation, $f_{\perp}$ is equal to the saturation value of Kerr rotation (θ_S) extracted from the out-of-plane field scan of θ_K. Generally, the first term on the left, which is given rise from polar MOKE, predominates θ_K, while the second term describes the minor contribution from the in-plane component via quadratic MOKE. The separation of these first- and second-order contributions can be done by carefully investigating the dependence of θ_K on the polarization plane of the laser.[*88, 89*]

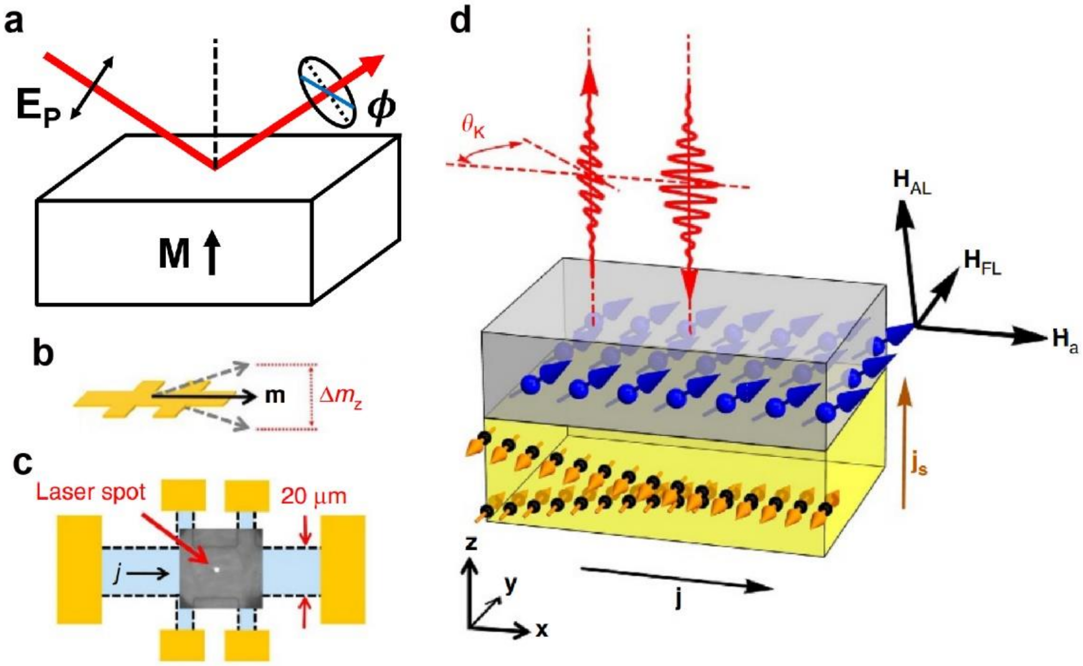

Figure 2-10. MOKE mechanism and capturing magnetization oscillation by Kerr rotation. (a) Schematic of the polar MOKE mechanism. The linearly polarized light obtains a phase and changes its polarization after being reflected from a magnetized surface. (b) SOT-driven magnetization oscillation around its equilibrium with an out-of-plane component Δm_z.(c) Device for MOKE measurement where a linearly polarized laser beam is focused perpendicularly on the sample. (d)A detailed schematic illustration for the MOKE measurement that was adopted to determine SOT in a heavy metal/ferromagnetic metal bilayer structure. Figure (b)-(d) adapted from Ref. [87].

In the MOKE measurement, the change of the Kerr angle ($\Delta\theta_K$) is induced by the oscillation of the magnetic moments around their equilibrium position driven by alternating SOT. Clearly, this current-induced $\Delta\theta_K$ is dominantly sensitive to the out-of-plane magnetization oscillation (Δm_z) in our configuration and quantitatively captures the information about SOTs. Of particular interest in the damping-like SOT, we focus on the case when the H_x is large enough to align all magnetic moments to the in-plane direction. With the magnetic moments polarized by H_x validating the macro-spin approximation, the quantitative relation between $\Delta\theta_K$ and the damping-like SOT is given by the following equation[*87*]

$$\Delta\theta_K = \frac{H_z^{eff} f_\perp}{H_x - H_K} \tag{2-4}$$

where H_K is the effective perpendicular anisotropy field. To extract θ_K and $\Delta\theta_K$, the reflected beam was sequentially passed through a half-wave plane, a Wollaston prism and collected by a balanced amplified photodetector that outputs a voltage signal proportional to $\cos(\omega_1)[\theta_K + \cos(\omega_2)\Delta\theta_K]$, where ω_1 ~ 100 kHz is the modulation frequency of laser intensity and ω_2 ~ 673 Hz is the frequency of the AC current the drives the magnetization oscillation. The output voltage is then fed into 2 consecutive lock-in amplifiers to extract θ_K and $\Delta\theta_K$ (Figure 2-11(a)). Noticeably, the ferromagnetic precession frequency of Cr-BST is on the order of a few GHz which is much higher compared to the frequency of AC current (~673 Hz), and hence, the magnetization oscillation in the Cr-BST layer can be assumed to adiabatically follow the current-induced H_z^{eff}. To ensure the accuracy of temperature, which might be influenced by laser heating effect and thermal radiation through the optical window, the local temperature of the device was carefully calibrated using its longitudinal resistance.

An example of the $\Delta\theta_K$ at 12 K probed with our MOKE-based magnetometer is displayed in Figure 2-11(b). H_z^{eff} can be extracted by fitting the experimental results to Equation 2-4 at the high field region, and the analysis of the linear current dependence of H_z^{eff} yields the SOT efficiency $\chi = 4.91 \times 10^{-4}\ Oe \cdot A^{-1} \cdot cm^2$ at 12 K, consistent with that obtained by hysteresis loop shift measurement. It should be noted that thermal artifacts (~J^2) that usually manifest in transport measurements should appear at higher harmonics and would not contribute to our first-harmonic optical results. MOKE measurements were also carried out at different temperatures from 12 K to 21 K, where fittings to Equation 2-4 at all temperatures confirm that the $\Delta\theta_K$ originates from the current-induced macroscopic magnetization oscillation via SOT. The optical signal became vanishingly small above 21 K because of a small magnetization in the Cr-BST layer.

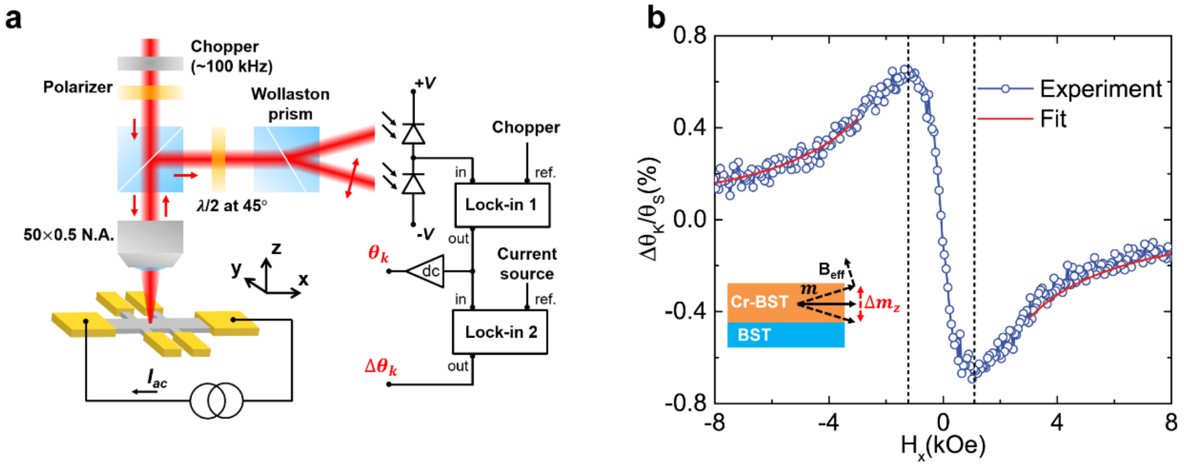

Figure 2-11. θ_{SH}^{3D} in Cr-BST/BST determined by MOKE measurements. (a) Schematic of the MOKE-based magnetometer with normal incidence and reflection geometry of the probe laser beam. The changes in polarization of the reflected laser are analyzed using a Wollaston prism and balanced photodiodes. Two successive lock-in amplifiers are used to extract the Kerr angle θ_K and the modulated Kerr angle $\Delta\theta_K$ induced by the AC current. (b) Differential Kerr rotation signal (blue circles) from the MOKE measurement capturing the magnetization oscillation Δm_z in the *z*-direction. The magnetization oscillation is induced by a periodic modulation of effective field H_z^{eff} from damping-like torque under an AC current. Fitting to the curve is shown by the red curves. Figure (a) and (b) adapted from Ref. [*79*].

2.4. Strong Temperature and Carrier Density Dependence of Spin-Orbit Torque

2.4.1. Temperature Dependence of Spin-Orbit Torque

In Chapter 2.3, H_z^{eff} from the optical method has been extracted from the fitting. Thus, θ_{SH}^{3D} can be determined by Equation 2-2 with the saturation magnetization M_s measured by SQUID at different temperatures. For comparison, θ_{SH}^{3D} is also calculated from χ^{sat} obtained in hysteresis loop shift measurements, and the temperature dependence of θ_{SH}^{3D} determined by both methods is plotted together in Figure 2-12(a). When T > 10 K, the value of θ_{SH}^{3D} from MOKE is very close to the value acquired by hysteresis shift, indicating that the θ_{SH}^{3D} independently measured from the above two essentially different approaches is consistent. When T < 10 K, it is noticed that θ_{SH}^{3D} rapidly increases as temperature decreases. At T = 2.5 K, θ_{SH}^{3D} reaches a maximum value of ~90, which is more than 2 orders of magnitude larger than the value of 0.2 at T = 17 K.

The values of θ_{SH}^{3D} in TI measured by different methods are summarized in Figure 2-12(b), in corresponding to their measurement temperatures (compared to Pt/CoFeB system[*90*]). As mentioned above, large discrepancies among measured θ_{SH}^{3D} can be noticed for the data to date. Although this could be attributed to instrument-related errors, the quality variation of the TI film, or other plausible mechanisms such as unidirectional spin Hall magnetoresistance that cause deviations of the measured values, the temperature-dependent data of the θ_{SH}^{3D} in this work fills in the large gap between the low temperature results and the high temperature results and explains why θ_{SH}^{3D} is much larger at 1.9 K.[*44*] Because TSS is a semi-2D carrier channel confined in the vicinity of TI surface, the charge-to-spin conversion process is primarily an interface phenomenon. Consequently, in TI systems the interfacial charge-to-spin conversion efficiency q_{ICS}^{2D} could be a better term to characterize this process. While in the heavy metal case, carrier transport is treated as 3D and θ_{SH}^{3D} is more commonly used, the term q_{ICS}^{2D} can also be calculated as a phenomenological term for comparison with TI systems. Given θ_{SH}^{3D} and the TI thickness t_s, q_{ICS}^{2D} of the Cr-BST/BST system is calculated to be ~ 5 nm^{-1} at *T*=2.5 K using Equation 2-1. On the other hand, it is found that $q_{ICS}^{2D} < 0.1\ nm^{-1}$ in most of the heavy metal systems at room temperature. Though measured at low temperatures, q_{ICS}^{2D} in the TI system is much larger than that in heavy metal systems and this again suggests a higher interfacial charge-to-spin conversion efficiency in TI, thanks to its spin-polarized TSS. Additionally, at 10 K q_{ICS}^{2D} of the Cr-BST/BST system is estimated to be $\sim 0.5\ nm^{-1}$, consistent with the experimental value in TI/FM structure determined by ST-FMR.[*85*]

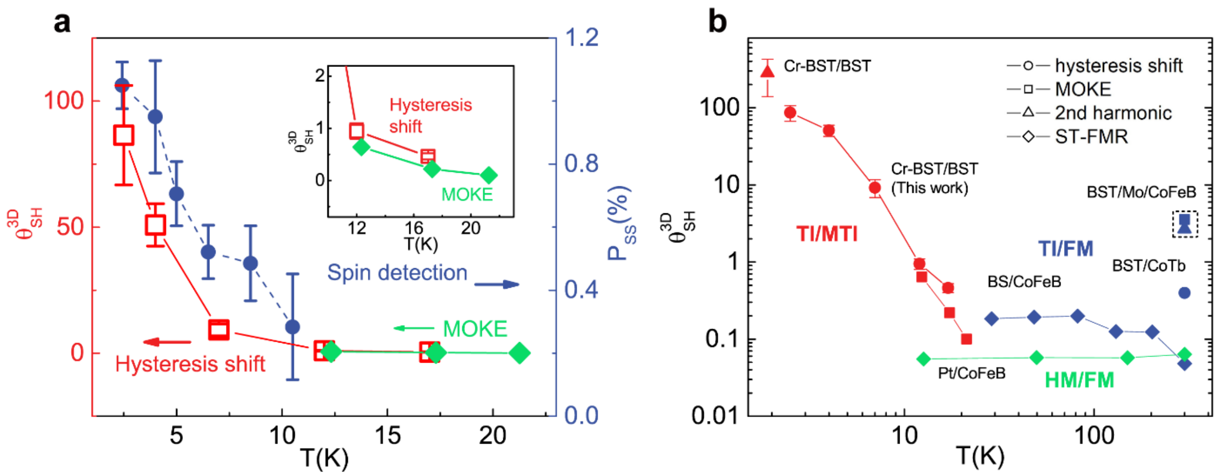

Figure 2-12. Temperature dependence of the spin Hall angle θ_{SH}^{3D} in Cr-BST/BST. (a) Temperature dependence of the spin Hall angle θ_{SH}^{3D} in the bilayer sample, in comparison with the spin polarization ratio P_{ss} in BST. Consistent values in the determination of θ_{SH}^{3D} are obtained by both methods at 12 K and 17 K, whereas below 12 K a dramatic increase of θ_{SH}^{3D} as the temperature further decreases is revealed. The

enhancement of θ_{SH}^{3D} follows the trend of the increasing spin polarization ratio in TI, as the higher spin polarization at low temperature contributes to a stronger damping-like torque. (b) Summary of θ_{SH}^{3D} measured in different material systems and by different measurement approaches. Figure (a) and (b) adapted from Ref. [*79*].

The dramatic increase of θ_{SH}^{3D} indicates a strong correlation between θ_{SH}^{3D} and temperature, and it will be of interest to further explore the underlying physics that accounts for the increase of θ_{SH}^{3D} in TIs. Intuitively, a straightforward explanation is that a larger θ_{SH}^{3D} can be resulted from an enhanced surface state conduction in TI at low temperature, since TIs such as Bi_2Se_3 and Bi_2Te_3 are prone to have additional bulk conduction at high temperatures apart from surface conduction due to a high E_F in the bulk conduction band. However, in our Cr-BST/BST bilayer film E_F is carefully tuned into the bulk bandgap by adjusting the Sb/Te ratio during the MBE growth. The small film thickness of only 7 QLs also minimizes the bulk conduction. To further examine the surface and bulk contributions to conduction, the carrier concentrations from the above two contributions can be quantitatively estimated. The total 2D carrier concentration n_{2D} in the Cr-BST/BST bilayer comes from a combination of the TSS carrier concentration n_{TSS} from two TSS and the bulk carrier concentration n_{bulk} as

$$n_{2D} = 2 \times n_{TSS} + n_{bulk} \qquad (2-5)$$

Here the extra carriers originating from two-dimensional electron gas (2DEG) due to Rashba effect[*15, 16, 18*] is not considered because unlike the HM/FM or the TI/FM heterostructure, inversion symmetry is preserved in the Cr-BST/BST bilayer system and a quantum well that confines interfacial states is unlikely to be present between the Cr-BST and BST layer. Now, n_{TSS} can be estimated by

$$n_{TSS} = \int_{E_{DP}}^{\infty} D(E) f(E) d(E) \tag{2-6}$$

where $f(E) = (1 + e^{E-E_F/k_BT})^{-1}$ is the Fermi-Dirac distribution, $D(E)$ is the TSS density of states, E_F is the Fermi level, k_B is the Boltzmann constant and T is temperature. Due to the Dirac cone dispersion of the TSS, E_F can be expressed as $E_F = \hbar V_F k_F + E_{DP}$, where $V_F \approx 5 \times 10^5 m/s$ is the Fermi velocity in TSS[*40*], $\hbar$ is the reduced Plank constant, k_F is the Fermi wave vector and E_{DP} is the Dirac point energy. The band dispersion of the TSS also gives the density of states as

$$D(E) = \frac{1}{2\pi} \frac{(E - E_{DP})}{(\hbar V_F)^2} \tag{2-7}$$

With Equation 2-6 and 2-7, n_{TSS} can be calculated as

$$n_{TSS} = \int_{E_{DP}}^{\infty} \frac{1}{2\pi} \frac{(E - E_{DP})}{(\hbar V_F)^2} \frac{1}{1 + e^{\frac{E - E_F}{k_B T}}} d(E) \tag{2-8}$$

When it comes to the bulk carrier concentration n_{bulk}, Equation 2-6 becomes

$$n_{bulk} = \int_{E_c}^{\infty} D(E) f(E) d(E) = \frac{8m^{*\frac{3}{2}}}{2\pi^2 \hbar^3} \int_{E_c}^{\infty} \frac{(E - E_c)^{\frac{1}{2}}}{1 + e^{\frac{E - E_F}{k_B T}}} d(E) \tag{2-9}$$

Here $m^* \approx 0.14 m_0$ is the electron effective mass and E_c is the bulk conduction band minimum. At 100 K, from the Hall measurement it can be estimated that $n_{2D} = 6.9 \times 10^{12}\ cm^{-2}$ (Figure 2-13(a)). By numerically solving Equation 2-5, 2-7 and 2-8, E_F, n_{TSS} and n_{bulk} are calculated to be $E_F = 0.216\ eV$, $n_{TSS} = 3.45 \times 10^{12}\ cm^{-2}$, and $n_{bulk} = 1.19 \times 10^7\ cm^{-2}$, respectively. It can be noticed that the bulk carrier concentration is several orders of magnitude smaller than the TSS counterpart, which confirms surface-dominated conduction in the Cr-BST/BST bilayer film after a careful tuning of the Bi:Sb ratio during growth.

It is necessary to investigate the dependence of n_{TSS} and n_{bulk} on temperature as well, since a rather straightforward explanation for the drastic increase of θ_{SH} could be the enhancement of the spin-polarized TSS contribution at low temperature. Here the temperature dependence of n_{TSS} and n_{bulk} can be theoretically estimated from Equation 2-7 and 2-8 as shown in Figure 2-13(b). Interestingly, n_{TSS} almost maintains constant as temperature decreases from 300 K to 2 K and no sign of n_{TSS} increase can be found at low temperatures. On the other hand, the bulk state carriers have been mostly frozen out below 100 K, which cannot result in the dramatic enhancement of the surface conduction ratio. Hence, the possibility of the TSS contribution enhancement at low temperature can be generally excluded, and the increase of θ_{SH} is most likely to be triggered by the intrinsic temperature-dependent behavior of TSS itself.

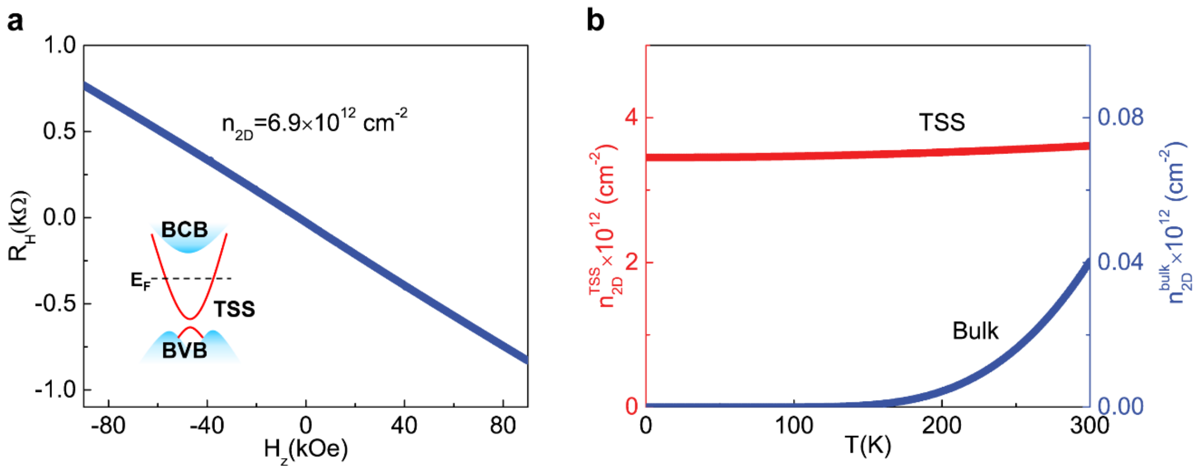

Figure 2-13. Decoupling the surface and bulk contributions to the total carrier concentration. (a) Total 2D carrier concentration n_{2D} calculated from Hall measurement at 100 K. $n_{2D} = 6.9 \times 10^{12}\ cm^{-2}$ can be estimated from the plot, suggesting a Fermi level of $E_F = 0.216\ eV$ above the Dirac point by numerical calculation. (b) Theoretical estimation of the TSS carrier concentration n_{TSS} and the bull carrier concentration n_{bulk} at different temperatures. The TSS contribution is unlikely to be significantly enhanced at low temperature due to an almost constant n_{TSS} and a vanishingly small n_{bulk}. Figure (a) and (b) adapted from Ref. [*79*].

While a more reasonable explanation should consider the intrinsic temperature-dependent properties of the TSS itself, the spin-polarized TSS in TI is considered to be the most critical ingredient in generating SOT, and the temperature-dependent spin polarization ratio should significantly affect θ_{SH}^{3D}. In our previous study, it is found that the spin polarization ratio also exhibits a similar trend in temperature dependence, which is plotted in Figure 2-12(a) for comparison.[*43*] Therefore, it is plausible that θ_{SH}^{3D} is enhanced by a larger spin polarization ratio at low temperature. While it can be calculated via Boltzmann transport that the thermal broadening of the Fermi-Dirac distribution at elevated temperatures cannot lead to a diminished spin polarization, the electron-phonon scattering can possibly suppress the spin polarization.

Given the Boltzmann transport distribution $(f_0 + f_1)$, the effective spin concentration with polarization along k_y direction can be expressed as

$$< \sigma > = \iint \overrightarrow{\sigma_k} \cdot D(E) \cdot (f_0 + f_1) dE d\theta \qquad (2-10)$$

Here $\overrightarrow{\sigma_k}$ is the projection of the spin polarization on k_y direction, $D(E) = \frac{1}{2\pi} \frac{(E - E_{DP})}{(\hbar V_F)^2}$ is the TSS density of states, f_0 is the Fermi-Dirac distribution function in equilibrium and f_1 is the displacement of the distribution function under an electric field Ɛ. Since $< \sigma_0 > = \iint \overrightarrow{\sigma_k} \cdot D(E) \cdot f_0 dE = 0$ in steady-state, $< \sigma >$ can be rewritten as $< \sigma > = < \sigma_1 > = \int \overrightarrow{\sigma_k} \cdot D(E) \cdot f_1 dE$. In the meantime, if a spin has an angle θ to the x-direction in k-space, because of spin-momentum locking its projection on the k_y direction can be represented by $\overrightarrow{\sigma_k} = \binom{-sin\theta}{cos\theta} \cdot cos\theta$ as shown in Figure 2-14(a). Under the relaxation time approximation, the displacement of the distribution function is $f_1 = -e\mathcal{E}\tau \frac{\partial f_0}{\partial E} dE$, and $< \sigma >$ becomes

$$< \sigma > = \frac{e\varepsilon\tau}{(\hbar V_F)^2} \int_0^{+\infty} (E - E_{DP}) \frac{\partial f_0}{\partial E} dE \int_0^{2\pi} \binom{-\sin\theta}{cos\theta} cos\theta d\theta \qquad (2-11)$$

Now if we assume a constant τ, the integration result from numerical calculation reveals the temperature dependence of $< \sigma >$ as shown in Figure 2-14(b). It can be seen that $< \sigma >$ is almost immune to temperature change, indicating that the thermal broadening effect of the distribution function is not the primary reason that explains the drastic temperature dependence of the spin polarization ratio.

Nevertheless, if the electron-phonon scattering effect on the carrier relaxation time is taken into consideration from the Boltzmann transport equation, the relaxation time can be expressed as

$$< \tau >_{ph} = \frac{\int \tau(E) E^{\frac{3}{2}} f_0 (1 - f_0) dE}{\int E^{\frac{3}{2}} f_0 (1 - f_0) dE} \qquad (2 - 12)$$

In metallic systems, it has been studied that the approximation of Equation 2-12 gives a canonical T^5 dependence of $< \tau >_{ph}$ as $< \tau >_{ph} \propto \frac{1}{(T)^5}$ at $T \ll \Theta_D$, and a T dependence as $< \tau >_{ph} \propto \frac{1}{(T)}$ at $T \gg \Theta_D$, where Θ_D is the Debye temperature.[*91*] From Equation 2-11, these temperature dependences of $< \tau >_{ph}$ in turn yields $< \sigma > \propto \frac{1}{(T)^5}$ and $< \sigma > \propto \frac{1}{(T)}$ for the above two temperature ranges, respectively. Now it becomes apparent that the electron-phonon scattering effect has a significant impact on the spin-polarization and is likely the predominant origin that triggers the drastic increase of θ_{SH} at low temperatures. Fitting to the curve in Figure 2-14(c) yield a temperature dependence of $\theta_{SH} \propto \frac{1}{(T)^{2.5}}$, which falls in between the canonical T^5 dependence range and T dependence range. There might be other contributions in the temperature dependence of $< \tau >$ besides the electron-phonon scattering such as electron-electron scattering, which requires future studies to further clarify.

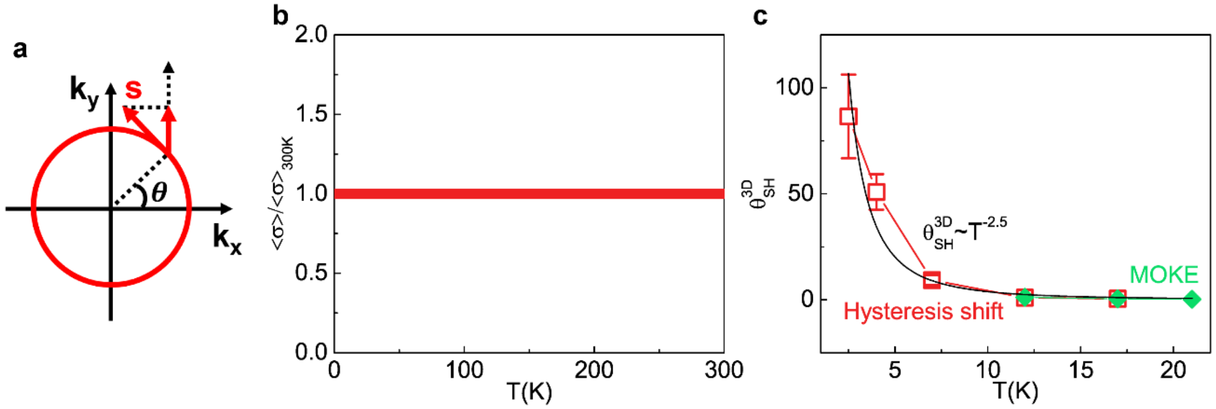

Figure 2-14. Thermal broadening and electron-phonon scattering effect on spin-polarization. (a) Spin polarization direction in the Fermi circle of the TSS if the spin has an angle of θ with the *x*-direction. (b) Theoretically calculated temperature dependence of the effective spin concentration normalized by its value at 300 K, if the relaxation time is presumed to be constant and only thermal broadening is taken into consideration. (c) Power law fitting to the temperature dependence of θ_{SH}, yielding a best fit of $\theta_{SH} \sim T^{-2.5}$.

2.4.2. Carrier Density Dependence of Spin-Orbit Torque

Apart from temperature as discussed in the previous section, another issue that can significantly affect the value of θ_{SH}^{3D} in a TI is the TSS carrier concentration, which is directly associated with the position of E_F. It has been reported that a higher carrier concentration when E_F is away from the Dirac point can give rise to a larger θ_{SH}^{3D} and conversely, θ_{SH}^{3D} diminishes if E_F is in the vicinity of the Dirac point.[*85*] Moreover, in a more complicated scenario, the top and bottom TSS may simultaneously drive opposite SOT on the magnetization and cancel out each other.[*46*] It will be intriguing if the contributions by the top and bottom TSS to the SOT can be decoupled. To investigate the SOT contributed by different TSS, another Cr-BST film with a thickness of 6 nm was grown by MBE. Unlike the Cr-BST/BST bilayer film, here the Cr-BST film is uniformly doped with Cr so that the magnetization can be altered by the torques from both top and bottom TSS. The Cr-BST film was subsequently fabricated into similar Hall bar devices but with a top gate geometry, where the 20 nm AlO_x deposited by atomic layer deposition serves as the gate dielectric, and metallization is completed by electron beam evaporation of Au (see cross-section in Figure 2-15(a)).

After applying a certain gate voltage, the carrier concentration of the top TSS can be effectively manipulated by shifting the top surface E_F. On the other hand, the E_F of the bottom TSS has a very limited change because of the screening effect.[*46*] The modulation of the carrier concentration by gate voltage can be inferred from the longitudinal resistance R_L as well as the Hall resistance R_H at 100 K as displayed in Figure 2-15(b). When V_g>0 V, E_F of both the top and bottom TSS are located in the upper Dirac cone and lead to an n-type behavior with a negative R_H. R_L also reaches a minimum value of 10 kΩ at V_g=15 V because of a high electron concentration. When V_g=-2.5 V, E_F of the top TSS is near the Dirac point (or the exchange gap opened by magnetization), which results in a minimum R_H value since the carriers in the top TSS are close to depletion. As V_g further decreases, E_F moves to the lower Dirac cone and the carriers of the top TSS become p-type. Because the dominant carriers are still electrons from the bottom surface, this gives rise to an increasing but still a negative number of the R_H. The top surface holes almost outnumber the bottom surface electrons at V_g=-17.5 V, leading to a positive R_H and a maximum R_L.

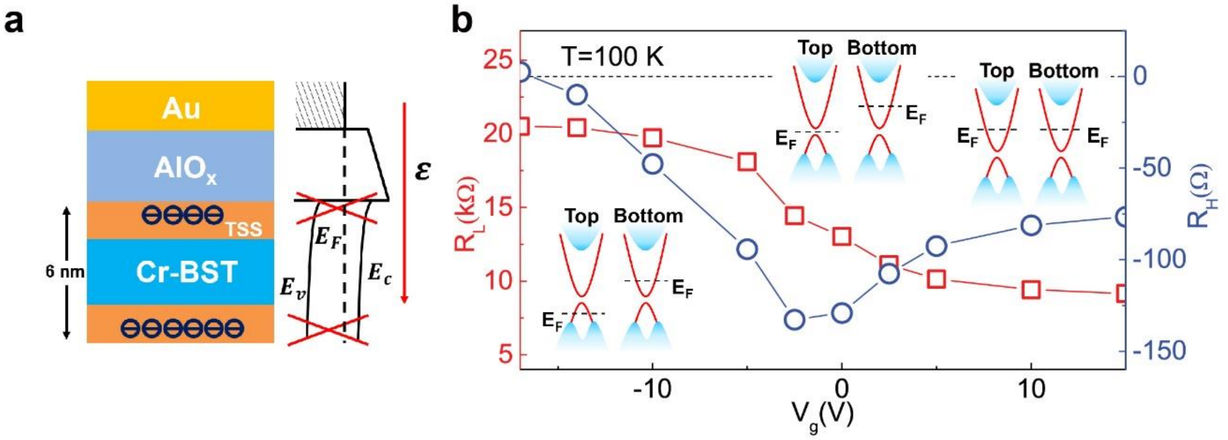

Figure 2-15. A uniformly-doped Cr-BST sample with electrostatic gating. (a) Schematic of the Cr-BST FET device cross-section with a top-gate geometry and its band diagram under a gate bias V_g. (b) Longitudinal and Hall resistance (R_L and R_H) of the device under different V_g at 100 K. While E_F of the bottom TSS locates in the upper Dirac cone, the top TSS E_F can be manipulated by tuning V_g, causing the change of both R_L and R_H. Figure (a) and (b) adapted from Ref. [*79*].

The modulation of the carrier concentration by gate voltage can also be indicated by the coercivity of a magnetic hysteresis loop. Measurements of both longitudinal and Hall resistance of the Cr-BST device were carried out at 2.5 K to further confirm the Fermi level position in the Cr-BST. At 2.5 K, robust ferromagnetism with pronounced anomalous Hall effect in the Cr-BST has already established, and it will be inaccurate to determine the Fermi level position simply by calculating the carrier concentration from the ordinary Hall effect. Nevertheless, the evolution of the carrier concentration under different V_g can be qualitatively inferred from the coercivity of the magnetic hysteresis loop. This is because in a magnetically doped TI, one underlying mechanism that rules the ferromagnetism is the carrier-mediated RKKY exchange interaction. As a result, the coercivity of the hysteresis is strongly dependent of the carrier concentration, e.g., more electrons/holes will lead to a larger coercivity. Such a correlation between coercivity and carrier concentration can be noticed in Figure 2-16a and 2-16b, where the hysteresis loops of both longitudinal and Hall resistance significantly rely on the carrier concentration under gate modulation. When V_g is between 0 V and -5 V, the Fermi level of the top TSS is in the vicinity of the Dirac point and the Cr-BST device has the lowest carrier concentration. As a result, the coercivity of both longitudinal and Hall resistance is the smallest under these gate voltages. When a positive V_g of 5 V and 10 V is applied on the device, the Fermi level is elevated to the upper Dirac cone such that more electrons are present in the top TSS. Thus the coercivity is expanded in this scenario. On the other hand, if a negative V_g of -10 V is applied, the Fermi level will be shifted to the lower Dirac cone and the top TSS will be dominated by holes, which also gives rise to a larger coercivity. It can be found that the estimation of the carrier concentration and Fermi level based on the coercivity at 2.5 K is consistent with the analysis from the ordinary Hall effect at 100 K.

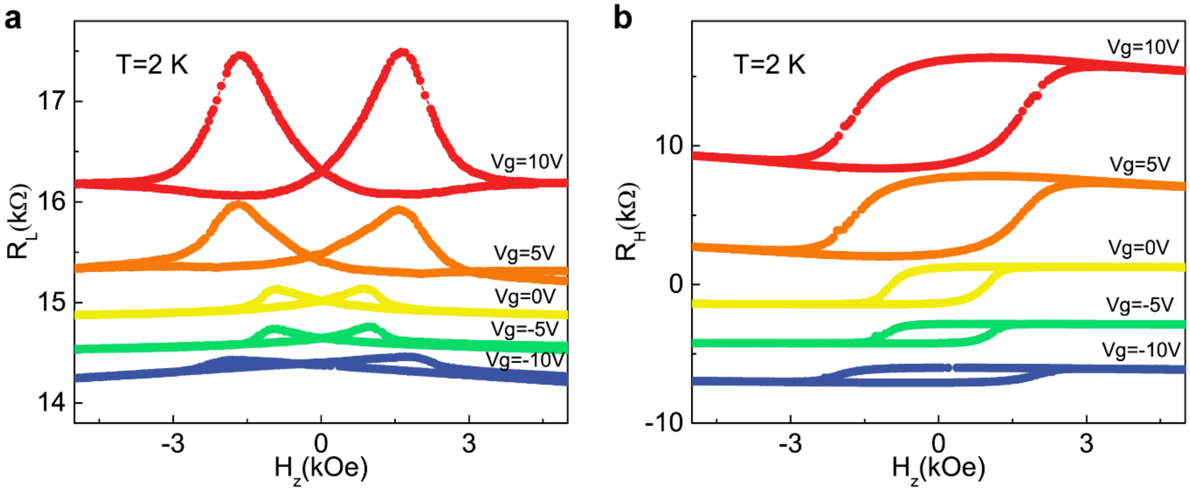

Figure 2-16. Modulating both longitudinal and Hall resistance of the Cr-BST device by the top gate at 2.5 K. (a) Longitudinal resistance of the Cr-BST device under different gate voltages from V_g=-10V to V_g=+10V. (b) Hall resistance of the Cr-BST device under different gate voltages from V_g=-10V to V_g=+10V. The coercivity of both the longitudinal and Hall resistance loops suggests a minimum carrier concentration in the Cr-BST device when V_g is between -5V and 0V.

More importantly, the SOT can be manipulated by gate voltage through the hysteresis shift measurement method that has been demonstrated in Chapter 2.3.1. When V_g=-10 V is applied on the device, the almost identical carrier concentrations in the two TSS but with different carrier types (holes in the top TSS and electrons in the bottom TSS) eventually result in a vanishingly small torque on the magnetization as shown in Figure 2-17(a), since the torques from both TSS almost cancel out each other. However, at V_g=0 V the carrier concentration of the bottom TSS exceeds that of the top TSS and contributes to a net torque on the magnetization in the bulk, hence the hysteresis moves toward the opposite direction when the DC current direction is reversed

(Figure 2-17(b)). It should be noted that H_z^{eff} here is a positive value comparing to the previous Cr-BST/BST bilayer device that has a negative H_z^{eff} (Figure 2-8(a)). Such a sign reversal of H_z^{eff} is caused by the fact that the net torque in the Cr-BST device under V_g=0 V is contributed by the bottom TSS, whereas in the bilayer Cr-BST/BST device the torque originates from the top TSS with an opposite spin polarization direction. If a positive gate bias of V_g=10 V is applied on the device to elevate E_F of the top TSS, the hysteresis shift by torque can barely be observed due to similar electron concentrations in these two TSS (Figure 2-17(c)). The evolution of H_z^{eff} under different gate biases are summarized in Figure 2-17(d), where H_z^{eff} reaches a maximum value of ~130 Oe under zero gate bias but is much weaker when $V_g = \pm 10$ V. At V_g=10 V, the sign reversal of H_z^{eff} can be attributed to a higher top TSS electron concentration that exceeds the bottom TSS electron concentration under a sufficiently large V_g. The gate modulation of SOT confirms the important role of both TSS in generating SOT, and moreover, the strong dependence of SOT on carrier concentration and the competition between two TSS potentially accounts for the wide discrepancies among the measured value of θ_{SH}^{3D} in TI. If a bottom gate geometry that separately tunes the bottom TSS could also be employed at the same time, the Cr-BST FET device may be conceived as a prototypic gate-controlled spin-orbit torque-magnetic random-access memory (SOT-MRAM) devices with even lower energy consumption.

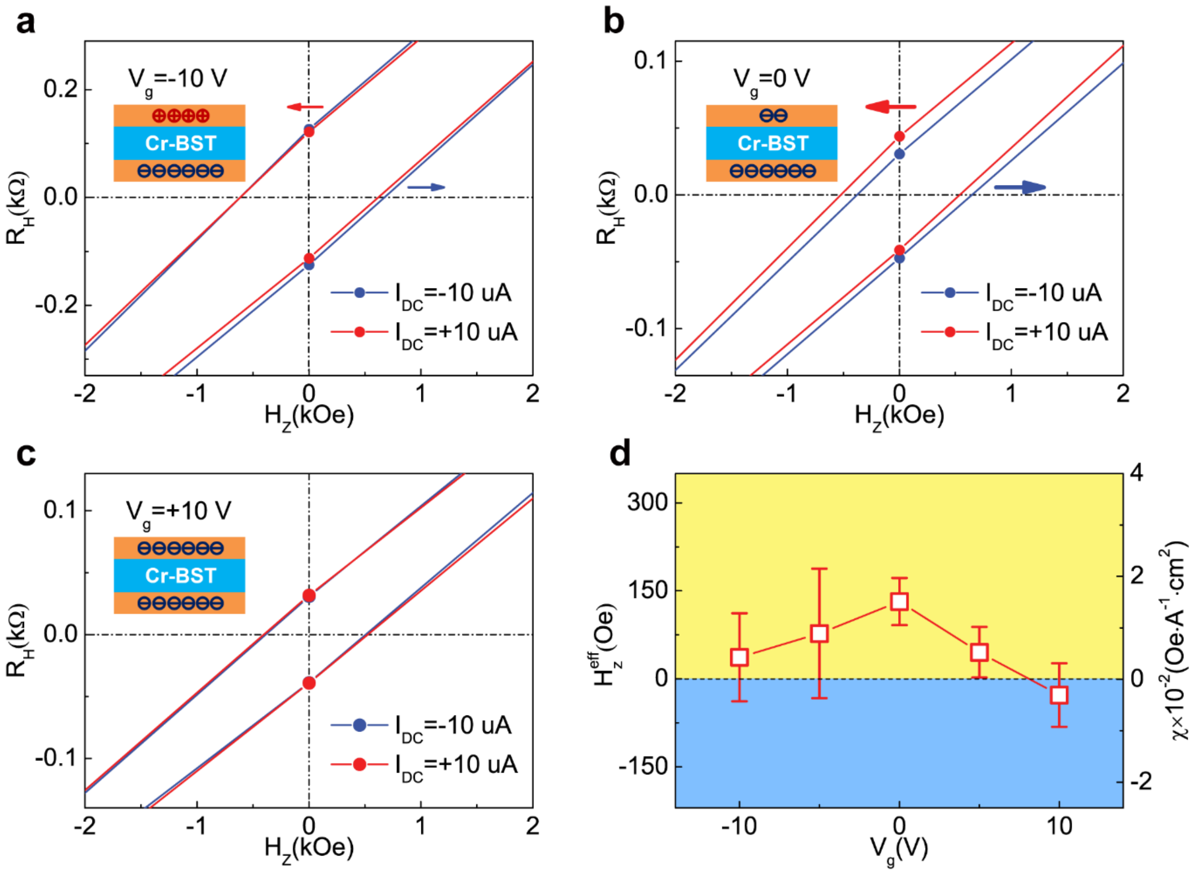

Figure 2-17. Decoupling the top and bottom TSS contributions of the anti-damping-like torque. (a)-(c) Hysteresis shift (zoomed-in) after applying DC current under different gate voltages. Though the top TSS is hole-dominated in Fig. (a) as E_F crosses the lower Dirac cone under a gate bias of V_g=-10 V, the top and bottom TSS have similar carrier concentrations that cancel out the anti-damping like torque from both TSS and lead to a vanishingly small hysteresis shift. (b) Under zero gate bias, E_F of the top TSS is in the vicinity of the Dirac point, whereas the bottom TSS E_F crosses the upper Dirac cone. In this scenario, the carrier concentration in the bottom TSS overwhelms the top TSS and results in an imbalanced anti-damping like torque exerted on the magnetization of Cr-BST. (c) The hysteresis shift becomes less pronounced again when V_g=10 V is applied, due to similar TSS carrier concentrations, noting that the top TSS is now electron-dominated in this case comparing to Fig. (a). On the other hand, the effective field H_z^{eff} exhibit a possible sign reversal, which could result from a slightly higher carrier concentration in the top TSS than the bottom

TSS. (d) Gate voltage dependence of the SOT effective field and SOT efficiency. Figure (a)-(d) adapted from Ref. [*79*].

2.5. Pulsed Current-Driven Magnetization Switching

As the ultimate goal of understanding the physics behind the SOT in TI is to achieve SOT-driven magnetization switching for memory applications, it should be examined whether the SOT is sufficient to switch the magnetization or not. In the Cr-BST/BST heterostructure, the strong SOT from TSS is able to drive efficient magnetization switching as demonstrated in Figure 2-18. The experiment was carried out by applying pulsed current with different amplitudes and a pulse width of 1 ms, after which probe current of 20 μA was applied to detect the magnetization through anomalous Hall effect. Such pulse width and probe current are chosen to minimize the Joule heating effect and at the same time obtain an optimal switching signal. The switching pulses and reading pulses were separated, and the reading pulses were applied Δt=1 s after the switching pulses since the magnetization switching should be non-volatile. A constant in-plane field of $H_x = \pm 200\ \mathrm{Oe}$ was applied during the experiment in order to break symmetry for deterministic switching.

Under an in-plane field of $H_x = +200\ \mathrm{Oe}$, it can be seen from the anomalous Hall resistance that the magnetization switches its direction from ‘up’ state to ‘down ’state when the pulsed current reaches a critical current of $I_{sw} \approx 0.9\ mA$. When negative pulsed current with a similar amplitude is applied, the magnetization switches back to ‘up’ state due to the reversed SOT.

In a similar manner, under an in-plane field of $H_x = -200$ Oe the magnetization switches between 'up' state and 'down' state when a critical current of $I_{sw} \approx 0.9\ mA$ is applied. Here the polarity of the switching loop is opposite compared to the positive in-plane field scenario because the symmetry is broken in the opposite direction. In both scenarios, the critical current for magnetization switching is $I_{sw} \approx 0.9\ mA$, equivalent to a current density of $J_{sw} \approx 6.25 \times 10^5\ A \cdot cm^{-2}$ and is more than 2 orders of magnitude lower than the switching current density in conventional HM/FM systems[*17*, *22*], suggesting a stronger SOT generated by TSS. In addition, we also expect a lower power dissipation in the TI system comparing to HM/FM systems, since J_{sw} is ~2 orders of magnitude lower than HM/FM systems though the sheet resistance R_s of TI ($R_s \approx 7.8k\Omega$ at 2.5 K here) is ~1 order of magnitude larger (typically $R_s \approx 1\ k\Omega$ in HM/FM).

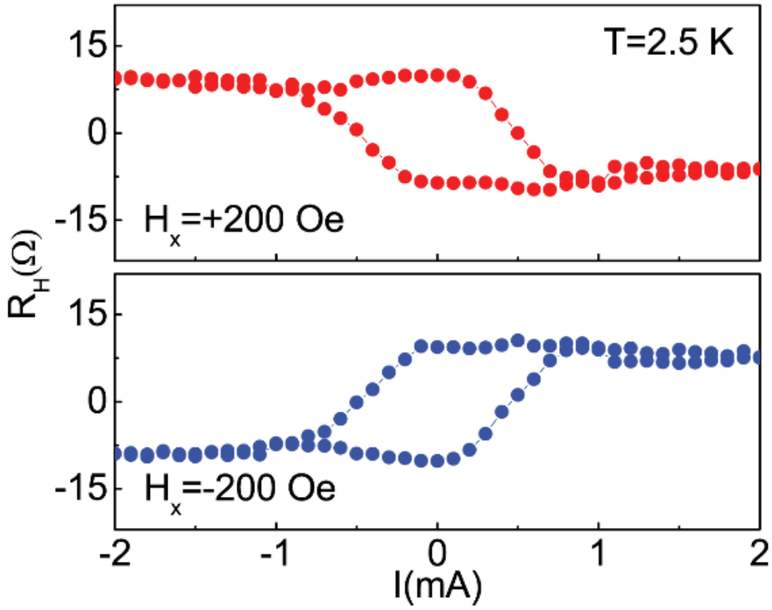

Figure 2-18. Pulse current-driven magnetization switching in the Cr-BST/BST heterostructure. The experiment was carried out at 2.5 K and under an in-plane field of $H_x = \pm 200$ Oe, with a pulse width of 1

ms. The magnetization can be switched when the applied current is larger than 1 mA, and the reverse of either current direction or magnetic field direction can result in an opposite final state of the magnetization. Figure adapted from Ref. [*79*].

While the above experiments were carried out under a fixed external magnetic field, to further investigate the magnetization switching behavior of the Cr-BST/BST heterostructure, additional switching experiments were carried out under different in-plane magnetic field and reading current. A microscope image of the Hall bar device for the switching experiment is shown in Figure 2-19(a), and the switching experiments were carried out at T=2.5K. It is reported that when a large in-plane field is applied during SOT-driven magnetization switching, it could compete with the perpendicular magnetic anisotropy of the magnetization and cant the magnetization toward the in-plane direction. Due to this reason, the observed switching window will drop with a large in-plane field.[*92, 93*] As displayed in Figure 2-19(b), because of the above phenomena the switching behavior is the most pronounced at $H_x = \pm 200\ Oe$ Oe but vanishes at a higher field of ~3000 Oe. The switching experiment was also performed with different applied read current densities (Figure 2-19(c)). When the reading current increases, the switching window reduces due to temperature increase and demagnetization caused by Joule heating. Such Joule heating can be attributed to a relatively high resistance of TI (sheet resistance $\sim 8\ k\Omega$ in our case) and a relatively large device size. On the other hand, the in-plane field applied is much smaller than the DMI effective field would result in partial switching. The Joule heating effect and partial switching could result in the small switching window in the Cr-BST.

From the switching current density obtained in Figure 2-19(b), spin Hall angle θ_{SH} can be subsequently estimated. The relationship between spin Hall angle and the switching current density can be described as[*94-96*]

$$J_{C,perp}^{SH} = \frac{2e}{\hbar}\frac{M_S t_F}{\theta_{SH}}\left(\frac{H_{K,eff}}{2} - \frac{H_x}{\sqrt{2}}\right) \qquad (2-13)$$

where $J_{C,perp}^{SH}$ is the current density to switch perpendicular magnetization, M_S is the saturation magnetization, t_F is the magnetization layer thickness, and $H_{K,eff}$ is the effective perpendicular anisotropy field. From Figure 2-19(b) it can be seen that at $H_x = 3000\ Oe$ the in-plane field overcomes $H_{K,eff}$ and $J_{C,perp}^{SH}$ reduces to zero. Consequently, $H_{K,eff}$ can be estimated to be ~4200 Oe. Using this $H_{K,eff}$, the switching current densities from Figure 2-19(b), and the other parameters extracted before, we are able to estimate θ_{SH} from different switching loops as shown in Figure 2-19(d). The switching current under different fields yields a quite consistent spin Hall angle of $\theta_{SH} \approx 44$. It should be noted that the Joule heating effect could result in an increased temperature and a reduced θ_{SH} in switching experiment. Therefore, θ_{SH} estimated by the switching current density is a bit smaller than the data from the hysteresis loop shift method (~90 at 2.5 K) but still generally agrees with the result.

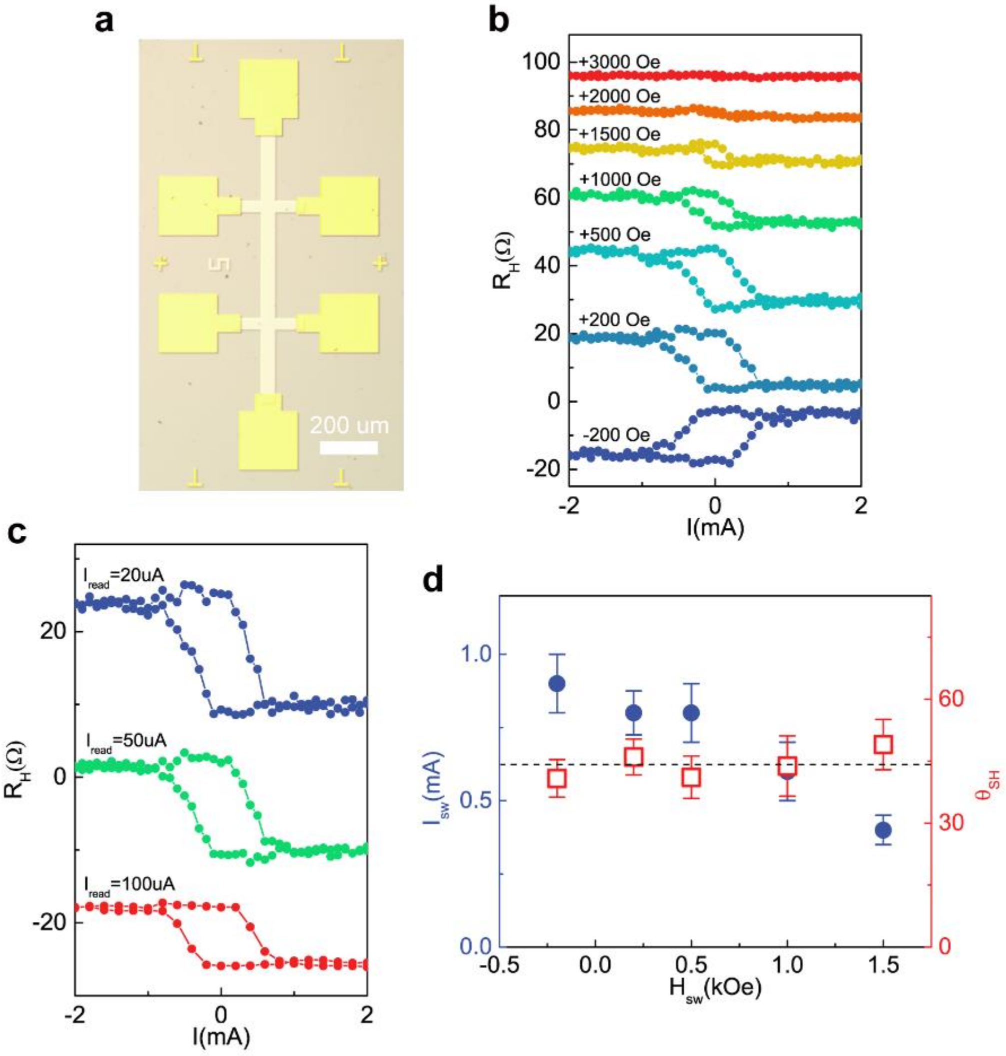

Figure 2-19. Additional magnetization switching results under different conditions. (a) Microscope image of the device for switching experiment. (b) Switching loops under different in-plane magnetic field. (c) Switching loops with different applied read current densities. (d) Switching current under different field density and estimated spin Hall angle. Figure (a)-(d) adapted from Ref. [*79*].

2.6. Summary of Chapter 2

In summary, we demonstrate a quantitative determination of the SOT in a Cr-BST/BST bilayer system by both the hysteresis loop shift method and the MOKE-based magnetometer. The above two approaches give consistent values of the spin Hall angle θ_{SH}^{3D} in the same device. Moreover, the temperature dependence of θ_{SH}^{3D} in TI is investigated and a drastic increase of θ_{SH}^{3D} is observed when the temperature is below 12 K. The enhancement of θ_{SH}^{3D} at low temperatures suggests a strong correlation between the temperature and SOT in TI, which can be further explained by a higher spin polarization ratio in the TSS at low temperatures. By applying a gate voltage on a uniformly doped Cr-BST film, we are able to separate the top and bottom TSS contributions of the SOT and manipulate the effective field, revealing an important role of both TSS in generating SOT. The significantly carrier concentration-dependent SOT as well as the competition between the top and bottom TSS could account for the large discrepancies among the reported value of θ_{SH}^{3D} in TI. Our work furthers the understanding of the unique role of the TSS in generating SOT and takes a step further in realizing TI-based magnetic memory devices.

Chapter 3

Symmetry Breaking and Field-Free Magnetization Switching in Topological Insulator/Antiferromagnet Heterostructures

3.1. Overview

SOT-driven magnetization switching can be an applicable approach to implement magnetic memory prototypes with faster speed, low power consumption and non-volatility. As is demonstrated in Chapter 2, TI as a promising material candidate can exert stronger SOT and accomplish magnetization switching with much lower current density. However, unlike the STT-driven magnetization switching approach, in SOT-driven magnetization switching with perpendicular magnetic anisotropy, a critical issue lies that the magnetization final state is not deterministic due to the mirror symmetry of the perpendicular magnetization and the damping-like SOT. It requires the assistance of an in-plane external field to break the mirror symmetry of the SOT, which is not desirable in practical applications. Several approaches have been reported to break the symmetry, such as particular geometries[*97*], wedged structures[*83*], and interlayer exchange-coupling[*98*]. Another viable method is to introduce an antiferromagnetic (AFM) layer adjacent to the FM layer so that the exchange-bias from the AFM layer can break the mirror symmetry.[*92, 99-101*] In addition, it has been demonstrated that the ferromagnetic order of TI in a TI/AFM heterostructure can exchange-couple with the AFM order in the AFM layer.[*102*] However, the field-free switching in TI-based material system has not yet been demonstrated.

In this chapter, we demonstrate field-free magnetization switching in TI/AFM exchange-biased material systems. A BST/CrSe heterostructure grown by MBE is firstly investigated, where a proximity-induced magnetic order and an exchange-bias both in the out-of-plane direction and in-plane direction is observed in magneto-transport measurements. The SOT generated by the spin-polarized surface states on the proximity-induced magnetization is quantitatively characterized by the hysteresis loop shift method and the spin Hall angle is estimated to be at least 5.3. After that a BST/Cr-BST/CrSe film is synthesized, where the BST layer is doped by Cr at the interface to enhance its perpendicular anisotropy, and robust pulsed current-driven magnetization switching is achieved with a switching current density of $J_{sw} = 5 \times 10^5 A/cm^2$. More importantly, in this system we realize magnetization switching at zero field with the assistance of the in-plane exchange bias from the CrSe layer after in-plane field-cooling (FC). Next, we investigated a Cr-BST/CrSb heterostructure that has an enhanced T_c of ~100 K due to the exchange coupling between the ferromagnetism in Cr-BST and the Neel order in CrSb with T_N of ~700 K. The SOT in the Cr-BST/CrSb heterostructure is quantitatively studied by second harmonic measurement, which reveals a spin Hall angle of ~3 at 10 K and is generally consistent with our previous results. Field-free switching is achieved in this system both at 1.9 K and at an elevated temperature of 100 K, thanks to the enhancement of T_c by the exchange coupling. Such field-free switching at elevated temperatures in TI exchange-biased material systems could be a promising candidate for magnetic memory device prototypes.

3.2. Symmetry Breaking for Deterministic SOT-Driven Magnetization Switching

Generally, in a magnetic system with perpendicular anisotropy and current-induced SOT, mirror symmetry of the damping-like SOT and magnetization preserves.[*83*] Such mirror symmetry causes equal probability for ‘up’ and ‘down’ magnetization when a current of the same direction is applied, resulting in non-deterministic magnetization switching., Figure 3-1(a) shows a prior work of DRL at UCLA that illustrates a typical HM/FM heterostructure, where the current-induced damping-like SOT H_y^{DL} exhibits mirror symmetry for different magnetization states under the same current. As a result, there is no favorable final state for the magnetization after SOT-driven switching. In experiments, magnetization switching behavior with the switching loop will not be observed in such a structure. However, if an in-plane external magnetic field is applied, mirror symmetry will be broken as shown in Figure 3-1(b). In this case, the ‘up’ and ‘down’ magnetization states are no longer equal and the SOT-driven magnetization switching will favor one certain direction for the applied current (‘up’ state is favored for the applied current in this figure). If the current direction is reversed, the favorable magnetization final state will also reverse and lead to an opposite magnetization state after switching.

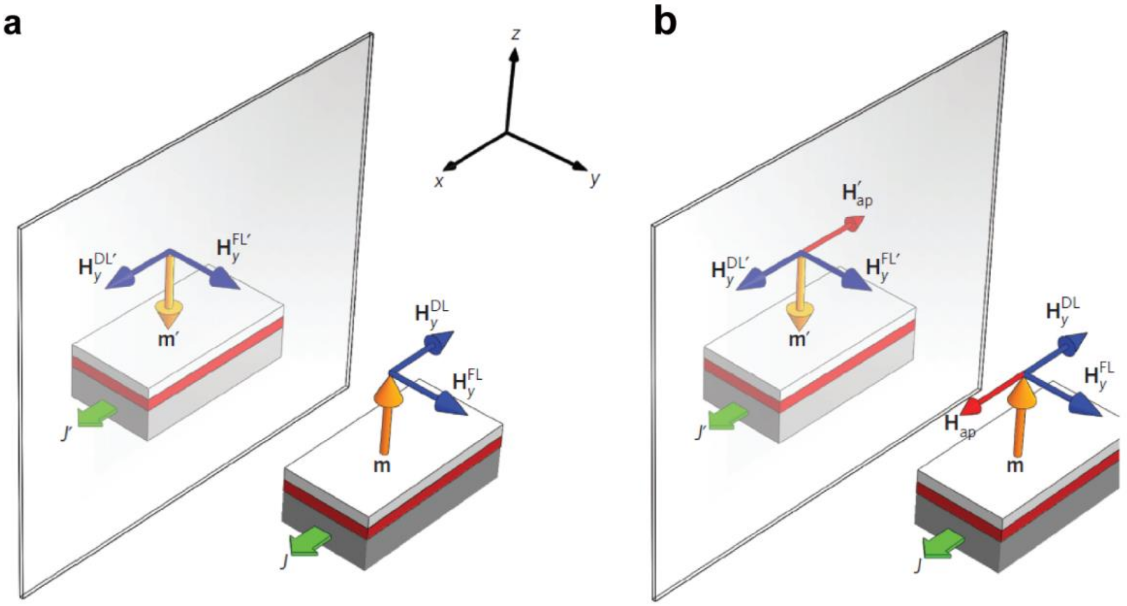

Figure 3-1. Mirror symmetry in current-induced SOT and symmetry breaking by an in-plane external magnetic field. (a) When a current J is applied in an HM/FM heterostructure, the current-induced damping-like SOT H_y^{DL} for the magnetization pointing to 'up' and 'down' directions preserve mirror symmetry. In this scenario, for the same current direction the magnetization is permitted to be in both 'up' and 'down' direction, which results in non-deterministic magnetization switching. (b) By applying an in-plane magnetic field H_{ap}, mirror symmetry is broken by the external field such that 'up' and 'down' magnetization states are not equal for the same current direction and only one state is favored by current-driven switching. Figure (a) and (b) adapted from Ref. [*83*].

Although an in-plane external magnetic field can break mirror symmetry as illustrated in Figure 3-1 and lead to deterministic magnetization switching, such an approach is not desirable in application since it would be rather challenging to introduce a constant magnetic field inside a semiconductor chip. One of the alternative solutions to realize field-free magnetization switching is utilizing exchange-bias to break the symmetry. Exchange-bias is a phenomenon present at the interface of an AFM/FM heterostructure.[*103, 104*] The strong AFM coupling in the AFM layer can exchange-couple with the magnetization in the FM layer and even reorient the direction of the magnetization. As an example, Figure 3-2(a) schematically shows a PtMn/CoNi structure, where the CoNi layer is FM and the PtMn layer is AFM.[*92*] The CoNi layer possesses a magnetization with perpendicular magnetic anisotropy, but here the exchange-bias at the interface is strong enough to tilt the magnetization toward the *x*-direction, which breaks mirror symmetry of the magnetization. The magnetic hysteresis loop of the CoNi layer in *x*, *y* and *z* directions are shown in Figure 3-2(b). While the hysteresis loops in the *y* and *z* directions remain centered, it can be noticed that the hysteresis loop in the *x*-direction (green curve) is shifted due to the exchange-bias in that direction. As a result, field-free magnetization switching can be achieved as demonstrated in Figure 3-2(c) and (d). Without applying an external magnetic field, the magnetization can be switched between ‘up’ and ‘down’ states by pulsed current. The magnetization switching is robust after a series of switching cycles, and the switching polarity can be controlled by manipulating the exchange-bias via different field-cooling. Since field-free magnetization switching has been realized in heavy metal systems but not in TI systems, we focus our work on field-free switching in TI systems that will be discussed in the next section.

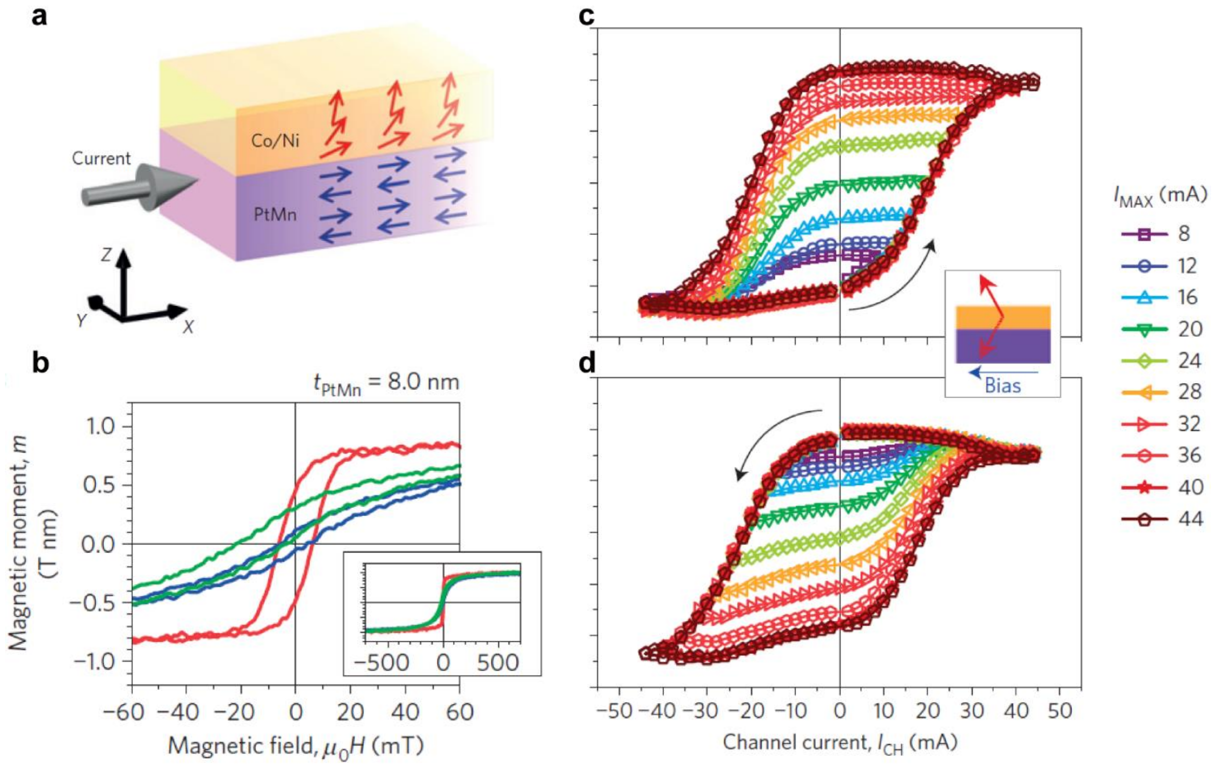

Figure 3-2. Symmetry breaking by exchange-bias in an AFM/FM structure and field-free magnetization switching. (a) In a PtMn/CoNi structure, the exchange-bias from the AFM PtMn layer can tilt the perpendicular magnetization in the CoNi layer toward the in-plane direction, thus breaking the mirror symmetry in this structure. (b) Due to the exchange-bias along the *x*-direction, the magnetic hysteresis loop of the CoNi layer in the *x*-axis is shifted (green curve), while the hysteresis loops in the *y* and *z* direction remain unchanged. (c) and (d) Field-free magnetization switching under different maximum pulsed current. Figure (a)-(d) adapted from Ref. [*92*].

3.3. Exchange-Bias and Field-Free Magnetization Switching in Topological Insulator/CrSe Heterostructures

3.3.1. Magnetic Properties of Topological Insulator/CrSe Heterostructures

In this section, we study the exchange-bias and field-free magnetization switching in TI/AFM structures, and one of the suitable AFM material candidates points to CrSe. Similar to many of the selenides and tellurides in transitional metal compounds, CrSe has a NiAs crystalline structure with a hexagonal close-packed unit cell. It is also known as an AFM material that has a non-collinear magnetic texture.[*105*, *106*] The magnetic moments of the three neighboring Cr atoms in a unit cell point to three different directions from top-view and have certain z-components in the side-view, forming an umbrella-like spin configuration in the unit cell (see Figure 3-3(a)). The BST/CrSe heterostructure film consisting of 8 QL BST (8 nm) in the bottom and 3 nm CrSe on the top was grown on GaAs (111) substrates by MBE. High crystalline quality and a sharp interface of the film are revealed by the cross-sectional STEM image in high-angle annular dark-field (HAADF) mode with atomic resolution (see Figure 3-3(b)). The BST/CrSe film was subsequently fabricated into μm-size devices with Hall bar geometry for magneto-transport measurement as shown in Figure 3-3(c).

To investigate the transport and magnetic properties of the BST/CrSe film, FC preprocessing under different magnetic field from T_N to 1.9 K was firstly performed for the sample, after which magneto-transport measurements were carried out. Figure 3-3(d) displays the Hall measurement results at T=1.9 K after FC of $H_z = \pm 10$ kOe along the z-axis, where magnetic hysteresis loops with pronounced coercivity and an anomalous Hall resistance of $R_{AHE} \approx 15\ \Omega$ were observed after subtracting the ordinary Hall background. It should be noted that the CrSe layer itself cannot give rise to a hysteresis loop with coercivity due to its AFM nature. In addition, our MBE-grown CrSe film is relatively insulating ($\sim 10^6\ \Omega$) compared to the BST/CrSe film ($\sim 10^4\ \Omega$) and its contribution to the transport result is vanishingly small. The magnetization in the BST does not stem from unexpected Cr doping during the growth either. Consequently, the hysteresis loops in Hall measurements mostly capture the magnetic properties of the BST layer, which reveals proximity-induced ferromagnetism in the BST layer through the interfacial exchange interaction with the CrSe layer. Such magnetic proximity effect in TIs has been discussed in Chapter 2.2.1, and is also reported in several FM/TI systems as well as in AFM/TI systems.[*56*, *70*, *71*, *107*]

Apart from the magnetic hysteresis loop, an out-of-plane exchange-bias after FC is also observed in the Hall measurement indicated by a horizontal shift of the hysteresis loop. The exchange-bias originates from the interfacial uncompensated spins at the interface between the CrSe and BST layers, and it is estimated to be $H_z^{EB} = 1.5\ \mathrm{kOe}$ after subtracting the linear Hall background. Since CrSe has a non-collinear magnetic structure and there is a finite projection of the magnetic moments in the *xy*-plane, we expect that exchange-bias can also exist in the in-plane direction. This is similar to an IrMn/CoFeB heterostructure where both out-of-plane and in-plane exchange-bias exist due to a non-collinear AFM structure of IrMn. To examine the in-plane exchange-bias in the BST/CrSe heterostructure, magneto-transport measurements were also performed after different FC with the external field along the *x*-direction. Detecting the in-plane exchange-bias via anomalous Hall effect that only captures the out-of-plane magnetization is challenging, however, the exchange-bias will affect the anisotropic magnetoresistance of the magnetic layer and can be easily measured through magnetoresistance measurements. The magnetoresistance after FC with $H_x = \pm 20\ \mathrm{kOe}$ is shown in Figure 3-3(e), where an in-plane exchange-bias of $H_x^{EB} = 1$ kOe is obtained from the horizontal shift of the magnetoresistance curves.

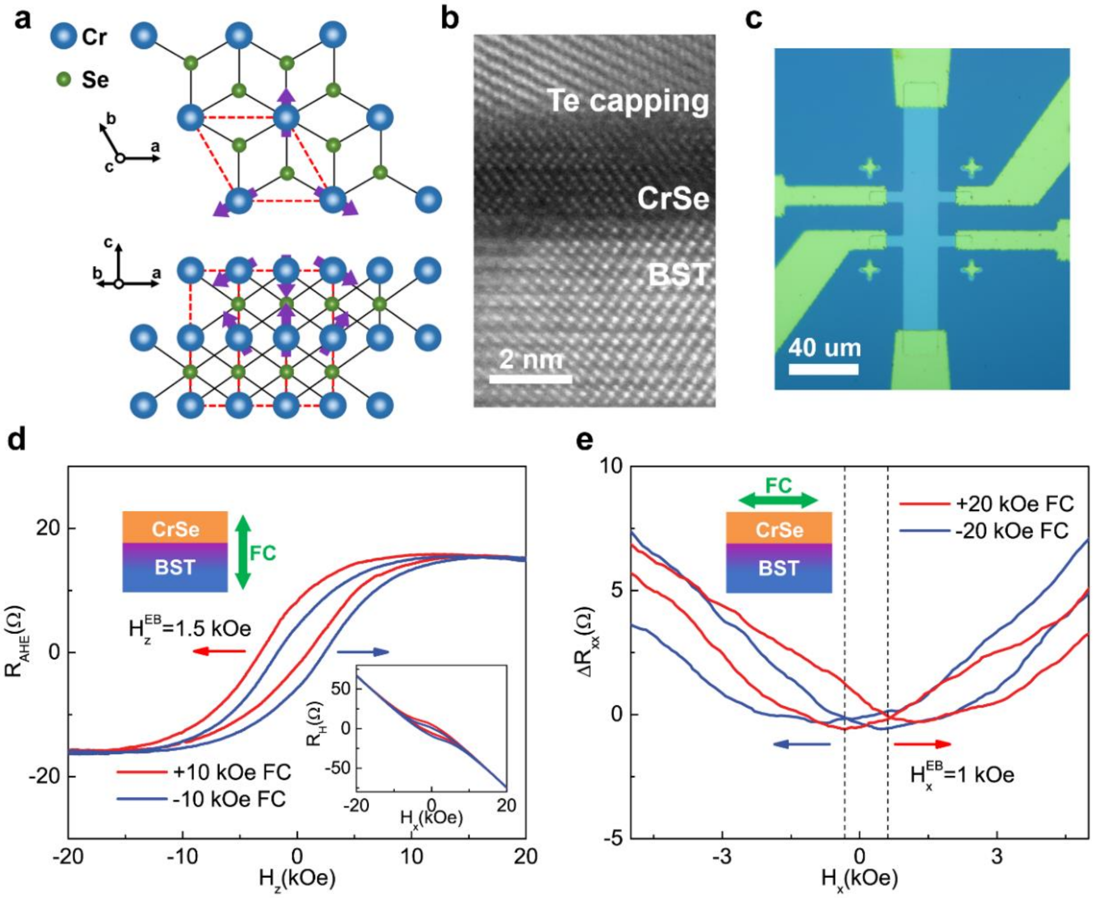

Figure 3-3. BST/CrSe heterostructure film and exchange-bias after fielding cooling. (a) Crystalline and magnetic structure of the non-collinear antiferromagnetic CrSe. Red dash lines denote a unit cell of CrSe. (b) Scanning electron microscope image of the BST/CrSe heterostructure by high-angle annular dark-field detector. (c) Hall bar device of the BST/CrSe heterostructure after fabrication. (d) Proximity-induced magnetic order in the BST layer and an out-of-plane exchange-bias of $H_z^{EB} = 1.5$ kOe in the hysteresis loop after FC of $H_z = \pm 10$ kOe along the z-direction. Inset: Hall resistance before the subtraction of ordinary

Hall background. (e) An in-plane exchange-bias of $H_x^{EB} = 1$ kOe in the longitudinal resistance after FC of $H_x = \pm 20$ kOe along the *x*-direction.

We grew a series of BST/CrSe bilayer films with the same growth parameters but different CrSe thickness, and Hall measurements were carried out to investigate the evolution of magnetization in these samples. While the BST layer is fixed to be 8 nm in all three samples, the thickness of the CrSe layer varies as 1 nm, 3 nm and12 nm. Hall measurements were performed after positive FC and negative FC of 10 kOe in the out-of-plane direction to establish an out-of-plane exchange-bias. When the CrSe thickness is 1 nm, only ordinary Hall effect without any trace of anomalous Hall effect or coercivity is observed as shown in Figure 3-4(a), indicating that the proximity induced magnetization is not present in this sample. This can be attributed to a weak AFM order in CrSe due to a finite thickness, which is insufficient to induce a robust magnetic order in the BST layer. Signature of magnetization appears in the sample with 3 nm-thick CrSe indicated by the hysteresis loops with certain coercivity (Figure 3-4(b)). Besides, an out-of-plane exchange-bias can be observed after positive and negative FC. The proximity-induced magnetization as well as the exchange-bias becomes more pronounced when the CrSe thickness is further increased to 12 nm (Figure 3-4(c)). Here, it is unlikely that the magnetization stems from unexpected Cr-doping into the BST layer, since in this scenario the BST/CrSe sample with 1 nm-thick CrSe would also be magnetized. The enhancement of the proximity-induced magnetic order as well as the exchange-bias by increasing the CrSe thickness can be explained by the establishment of a stronger Néel order in thicker CrSe layer that promotes both the proximity effect and the exchange-bias.[*108*]

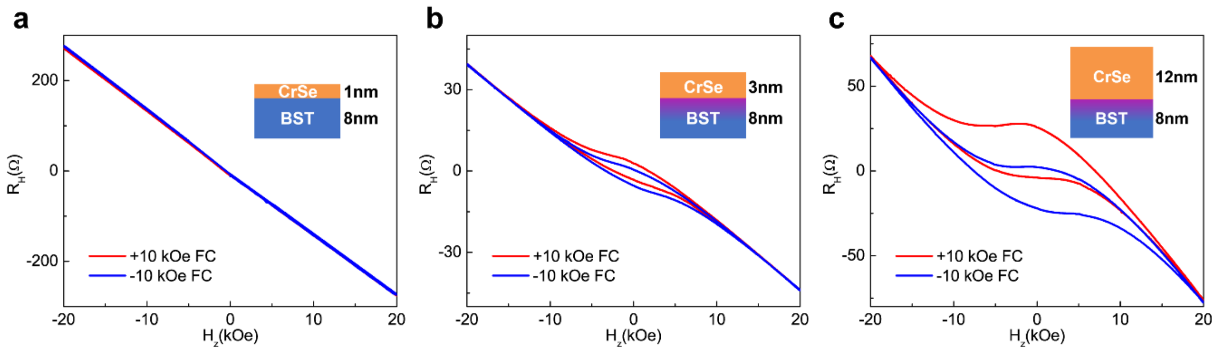

Figure 3-4. Hall measurement results of BST/CrSe bilayer films with different CrSe thickness after positive and negative FC. (a-c) Hall measurement results of BST/CrSe films with CrSe thickness of 1 nm, 3 nm, and 12 nm, respectively. No anomalous Hall effect or coercivity is observed in the sample with 1 nm-thick CrSe. Hysteresis and exchange-bias appear when the CrSe thickness is 3 nm, and become more pronounced in the sample with 12 nm CrSe.

3.3.2. Measuring Spin-Orbit Torque by Hysteresis Loop Shift Method

Since a proximity-induced magnetic order is present in the BST layer at the interface as demonstrated in the previous section, the spin-polarized TSS could drive SOT on the magnetization, and it will be of interest if the strength of the SOT in the BST/CrSe system can be further determined. Here we measure the strength of SOT by hysteresis loop shift measurements discussed in Chapter 2.3.1. Although this measurement technique requires the simultaneous application of a constant in-plane field and a modulating out-of-plane field, in material systems where the FM layer is interfaced with an AFM layer, the exchange-bias from the interfacial uncompensated spins can fulfill the role of an in-plane external field and assist the measurement of the effective field.[*92*] To determine the SOT in the BST/CrSe bilayer film, the sample firstly went through a positive FC with $H_x = +20\,\text{kOe}$ in the *x*-direction that create an in-plane exchange-bias toward –*x*-direction. Hall measurements were carried out after FC at the base temperature of T=1.9 K, and DC current of $I = \pm 20\ \mu A$ with opposite directions are sequentially applied to generate opposite effect field that horizontally shifts the hysteresis loops as shown in Figure 3-5(a). The effective field can be calculated as $H_z^{eff} = -(H_z^{+} + H_z^{-})/2$, where H_z^{+} and H_z^{-} represent the shift of the positive switching field and the negative switching field in the hysteresis loop, respectively. Here the effective field is extracted to be $H_z^{eff} = 200$ Oe from the loop shift. Hall measurements were also carried out after negative FC as displayed in Figure 3-5(b). In this scenario, the magnetic moments at domain boundaries are reoriented toward +*x*-direction by exchange-bias. As a result, the effective field on these magnetic moments is reversed, and the current-driven hysteresis loop shift also becomes opposite comparing to Figure 3-5(a). The effective field is extracted to be $H_z^{eff} = 200$ Oe in this measurement, consistent with the result obtained after positive FC.

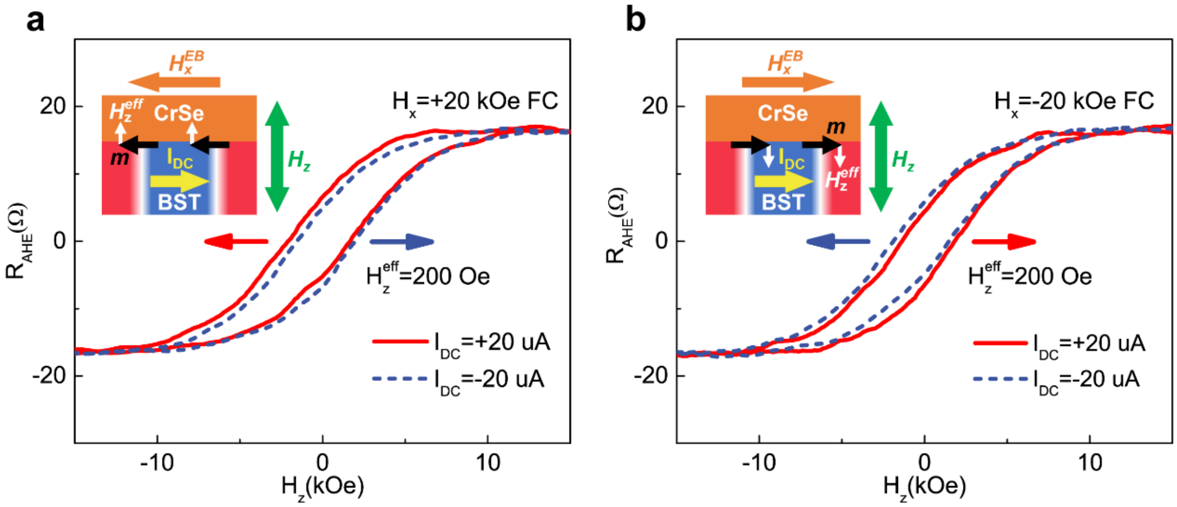

Figure 3-5. Hysteresis loop shift by SOT in the BST/CrSe heterostructure. (a) Hysteresis loops after $+20$ kOe in-plane FC when DC current is applied. The magnetic moments at domain walls are reoriented towards -*x* directions by the exchange coupling after FC, and the current-induced SOT exerted on the magnetic moments generate an out-of-plane effective field (see inset). The hysteresis loop shift toward the opposite direction due to the reversal of the out-of-plane effective field after changing the current direction. (b) Hysteresis loops after -20 kOe in-plane FC when DC currents are applied. For both positive and negative DC current, the hysteresis loop shift direction is opposite compared to (a) because the magnetic moments at domain walls are canted toward +*x* direction in this scenario.

For comparison, the exchange-bias and SOT effective field measurements were also carried out in the 8 nm BST/12 nm CrSe sample that has a stronger proximity-induced magnetization and exchange-bias than the 8 nm BST/3 nm CrSe sample. Figure 3-6(a) shows the hysteresis loops (ordinary Hall background subtracted) after out-of-plane FC of 10 kOe, revealing an out-of-plane exchange-bias of $H_z^{EB} = 3.8$ kOe. The in-plane exchange-bias is measured to be $H_x^{EB} = 1.8$ kOe in magnetoresistance measurement after in-plane FC of 20 kOe as displayed in

Figure 3-6(b). It is noticed that the exchange-bias in the 8 nm BST/12 nm CrSe sample is more pronounced than the 8 nm BST/3 nm CrSe sample both in the out-of-plane and in-plane direction owing to a larger CrSe thickness and a stronger exchange-coupling. The SOT effective field is also measured by hysteresis loop shift measurements, and a consistent result of $H_z^{eff} = 500\ \mathrm{Oe}$ is obtained after positive and negative FC (Figure 3-6(c) and (d)). Because of the larger exchange-bias in the 8 nm BST/12 nm CrSe sample, more magnetic moments at domain boundaries are reoriented by the exchange-bias, leading to a more significant SOT effective field in the 8 nm BST/12 nm CrSe sample than the 8 nm BST/3 nm CrSe sample ($H_z^{eff} = 200\ \mathrm{Oe}$). On the other hand, the larger measured SOT effective field due to an enhanced in-plane exchange-bias also indicates that the exchange-bias is insufficient to overcome the DMI effective field in the 8 nm BST/3 nm CrSe sample, where the measured value of the SOT effective field should be lower than its intrinsic value.[*109*]

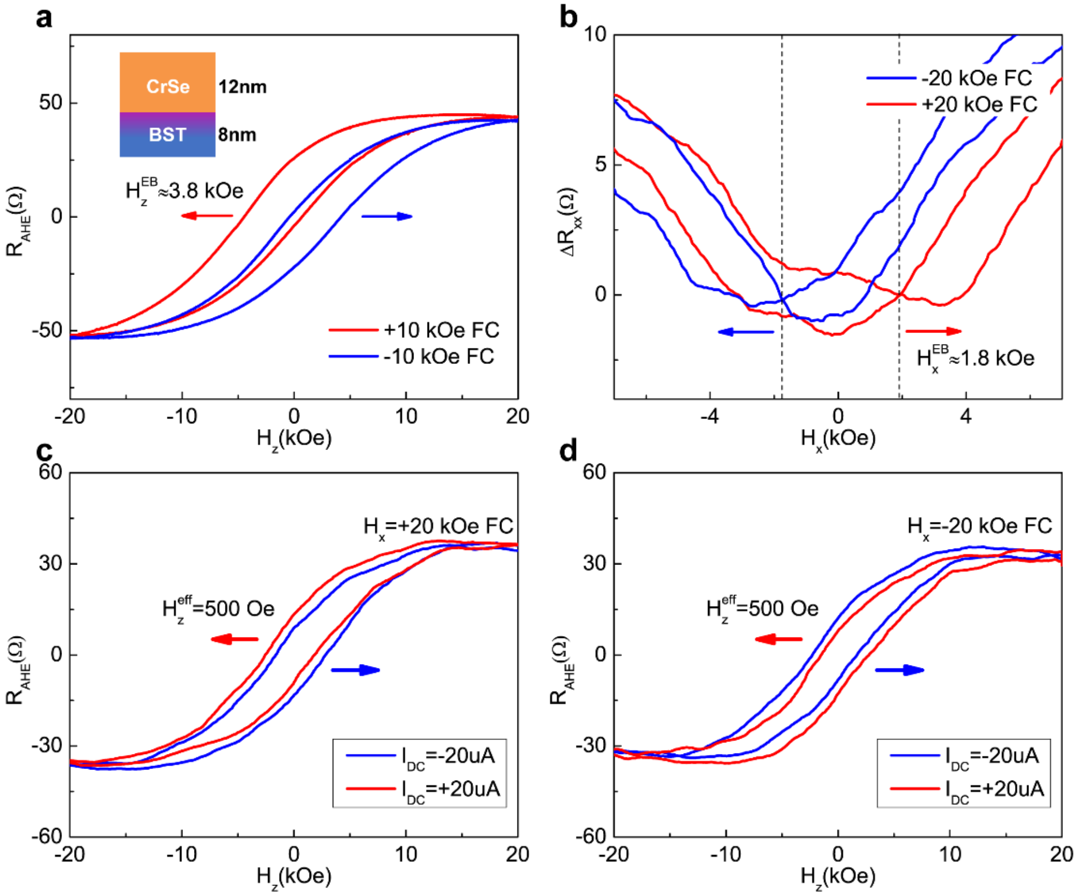

Figure 3-6. Exchange bias and SOT effective field in the 8 nm BST/12 nm CrSe sample. (a) Out-of-plane exchange-bias in the sample after 10 kOe out-of-plane FC. (b) In-plane exchange-bias in the sample after 20 kOe in-plane FC. Both the out-of-plane and in-plane exchange-bias become more pronounced due to a thicker CrSer layer. (c) SOT effective field measured by hysteresis loop shift measurement after positive FC. (d) SOT effective field measured after negative FC. The SOT effective field is consistent in both measurements, and is higher than the results from the 8 nm BST/3 nm CrSe sample due to a stronger exchange-bias.

Through the hysteresis loop shift measurements, the strength of SOT was systematically quantified as a function of DC current densities. Figure 3-7(a) shows the zoomed-in details of the hysteresis loops near the coercive field when DC currents ranging from $10\ \mu A$ to $20\ \mu A$ are applied after $+20$ kOe in-plane FC. Red curves denote the data from the measurement with a positive DC current and blue curves stand for the data from the measurement with a negative DC current. The hysteresis loop exhibits the most pronounced shift under $I = \pm 20\ \mu A$, indicating a stronger SOT driven by higher current density. The shift of the hysteresis loops near the magnetization reversal point ($R_{AHE} = 0\ \Omega$) is summarized in Figure 3-7(b), where the red triangles are the coercive field of the down-to-up slope H_{sw}^{DU}, the blue triangles are the coercive field of the up-to-down slope H_{sw}^{DU}, and the effective field (black circles) can be expressed as $H_z^{eff} = (H_{sw}^{\mathrm{DU}} + H_{sw}^{\mathrm{UD}})/2$. It should be noted that the measured data cannot be artifacts from potential thermal effect such as spin Seebeck effect or anomalous Nernst effect, since the effect of those phenomena on Hall voltage can be expressed as $V_{xy} \propto m \times \nabla T$ and they will only change the anomalous Hall resistance rather than a horizontal shift of the hysteresis loop. In addition, any contributions from Joule heating will manifest as a quadratic behavior since $\nabla T \propto I^2$, but in our measurements the effective field scales linearly with the applied DC current. Therefore, we generally exclude potential artifacts from thermal effects and affirms the reliability of the hysteresis loop shift approach in measuring SOT.

Similarly, the result of hysteresis loop shift measurements after a negative FC of $H_x = -20$ kOe is shown in Figure 3-7(c). As aforementioned, the exchange bias now reverses its direction after the negative FC and the magnetic moments in the domain walls during magnetization reversal are aligned towards +*x* direction, opposite to the scenario in Figure 3-7(a) and 3b. Consequently, the SOT effective field established on the magnetization is also reversed under the same current and we observe a negative sign of the effective field slope. Figure 3-7(d) summarizes the measured effective field after both positive and negative FC. While the data suggest a consistent SOT strength after different FC, the SOT efficiency χ can be calculated by linear fitting to the data points, yielding a result of $\chi = 0.0173\ \mathrm{Oe} \cdot A^{-1} \cdot cm^2$. Since the penetration depth of the proximity-induced magnetic order in TI is approximately $1nm$[55], using the above-calculated χ and a saturation magnetization of $M_s = 16\ emu/cc$ the spin Hall angle of BST can be estimated by Equation 2-1 in Chapter 2.3.1, which gives a spin Hall angle of $\theta_{SH} = 5.3$. Here, it should be noted that the measured value of χ and θ_{SH} only set a lower bound of the actual SOT efficiency and spin Hall angle in this system, since the determination of the actual values requires a sufficient in-plane field to overcome the DMI effective field H_{DMI} and align all the magnetic moments at the domain boundaries to the same direction, but exchange bias from the CrSe layer might not be large enough to overcome H_{DMI}. Nonetheless, this lower bound value of θ_{SH} is still significantly larger than θ_{SH} of the conventional heavy metals in SOT study such as Pt and Ta[109], suggesting that TIs could potentially drive much stronger SOT for magnetic memory device applications.

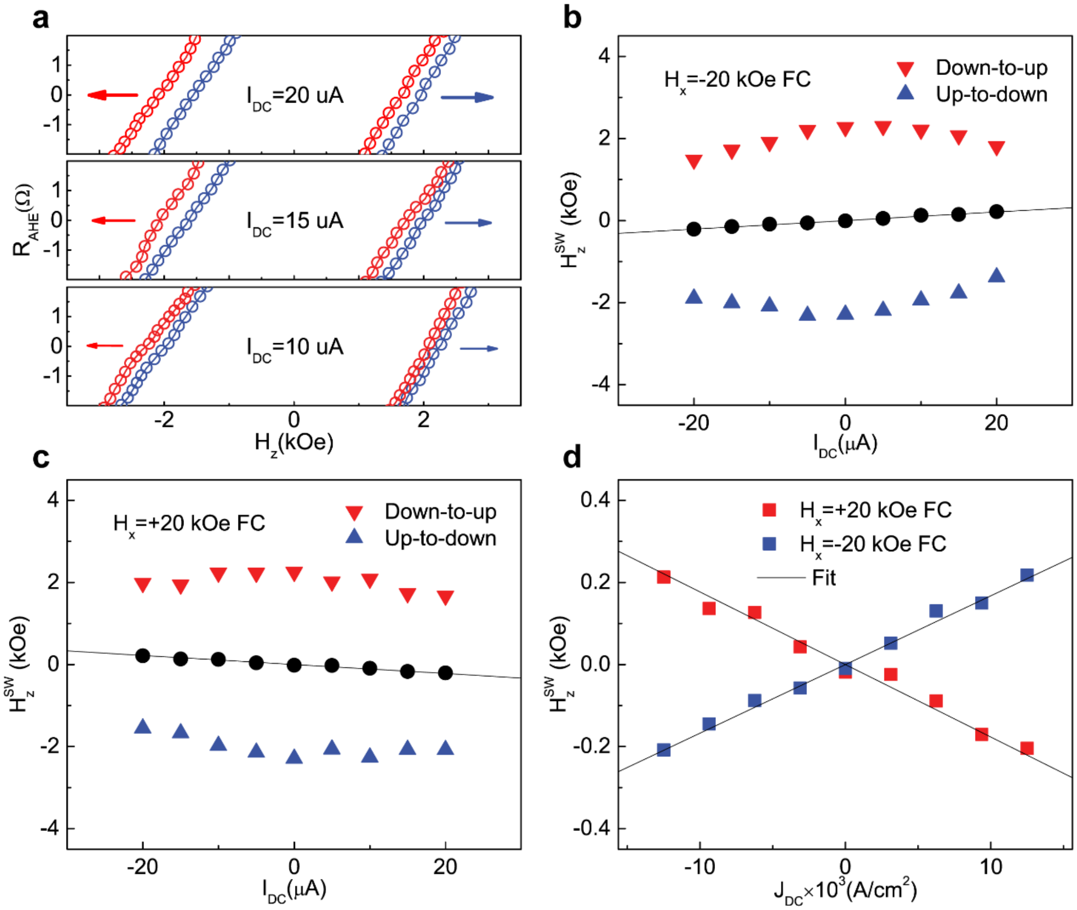

Figure 3-7. Linear scaling of SOT effective field with current density. (a) Hysteresis loop shift when DC currents of 10 µA, 15 µA, and 20 µA are applied. (b) Applied magnetic field when the hysteresis loops in (a) intersect with $R_{AHE} = 0\ \Omega$. Red dots denote the down-to-up edge of the hysteresis loop, blue dots represent the up-to-down edge of the hysteresis loop, and black dots are the average of the above two fields. The data were collected after -20 kOe in-plane FC. (c) The intersection of the hysteresis loops with $R_{AHE} = 0\ \Omega$ after $+20$ kOe in-plane FC. (d) Current dependence of the SOT effective field, which linearly scales with current density and yields a SOT efficiency of $\chi = 0.0173\ \mathrm{Oe} \cdot A^{-1} \cdot cm^2$.

3.3.3. Field-Free Magnetization Switching at 1.9 K

To further explore the TI/AFM exchange-coupled structure and its SOT-driven magnetization switching behavior, we investigated a BST/Cr-BST/CrSe (7 nm/1 nm/3 nm) film with modulated Cr doping in BST, where magnetization can be switched in a non-volatile manner by pulsed current. More importantly, we took advantage of the in-plane exchange bias from the AFM CrSe layer and accomplished magnetization switching without an external magnetic field. Figure 3-8(a) displays the sketch of the device structure. Because perpendicular anisotropy is required for robust pulse-current switching but the proximity-induced magnetization at the interface of the BST/CrSe heterostructure cannot support adequate perpendicular anisotropy, we intentionally doped the BST layer with Cr at the interface during the MBE growth to enhance the perpendicular anisotropy. Magnetization switching driven by pulsed current was firstly examined after ZFC with the application of an in-plane external field at T=1.9 K. The experiment was carried out by applying a switching pulse with a pulse width of 1 ms, after which a reading pulse with much lower current density was applied to probe the magnetization via anomalous Hall resistance, and such procedure was repeated sequentially with modulated pulse amplitude. As shown in Figure 3-8(b), the magnetization in Cr-BST can be successfully switched, and the switching current density is estimated to be $J_{sw} = 5 \times 10^5 A/cm^2$, which is 2 orders of magnitude lower than the typical switching current density reported in heavy metal/ferromagnetic metal structure and almost 1 order of magnitude lower than TI/ferromagnetic metal structure.[*17*, *110*] In this case, the magnetization in the Cr-BST preserves its mirror symmetry at zero field where no obvious switching hysteresis can be observed. However, after a positive in-plane FC of +10 kOe, the mirror symmetry is broken by the exchange bias from the CrSe layer and the magnetization in Cr-BST cants to -*x*-direction. In consequence, the magnetization can be switched at zero field as shown in

Figure 3-8(d) while at $H_x = -100$ Oe the exchange bias is compensated by the external field. Similar field-free switching behavior can be observed after a negative FC of $H_x = -10$ kOe as displayed in Figure 3-8(e) and (f), with a reversed switching polarity due to a negative exchange-bias. The magnetization switching at zero field exhibits less switching ratio than the switching at $H_x = \pm 400$ Oe, which can be explained by the grain effect where AFM grains with different local uncompensated spin directions could lead to incomplete switching at zero field.[*101*]

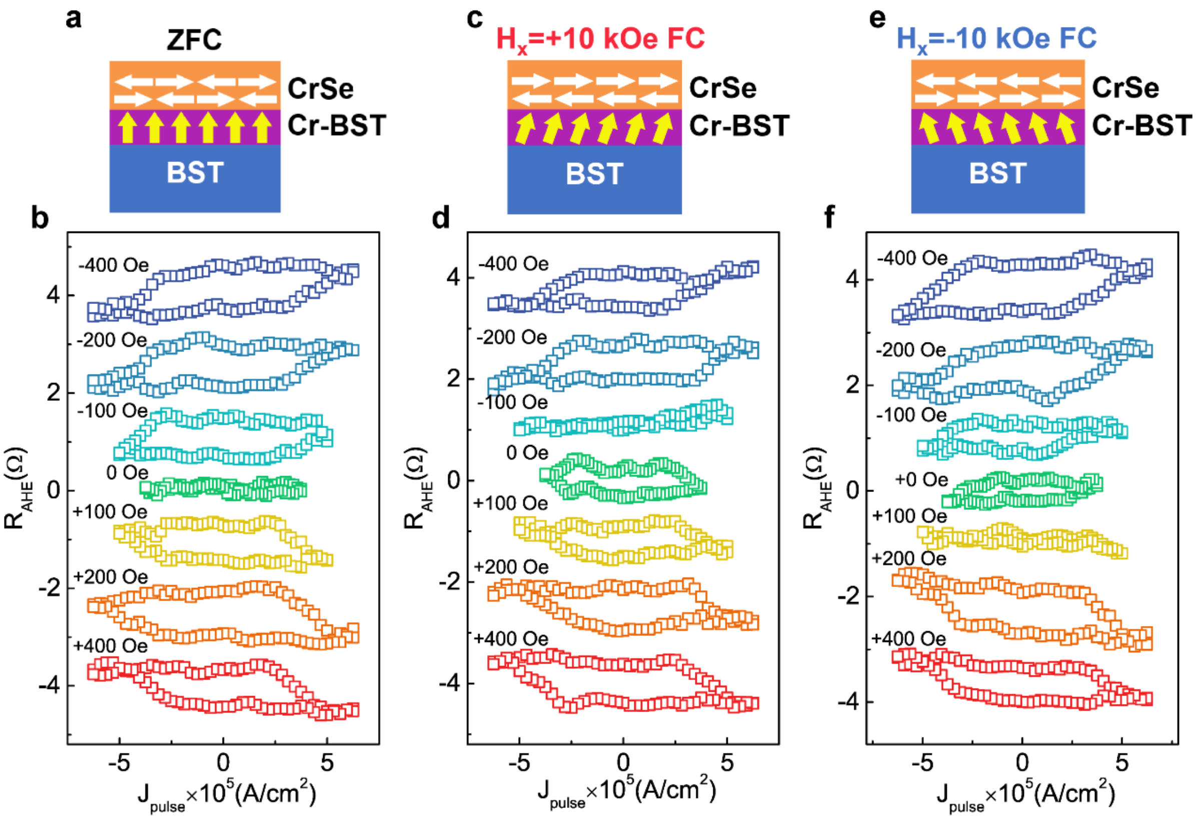

Figure 3-8. Field-free magnetization switching in a BST/Cr-BST/CrSe device after in-plane FC. (a) Pulse-current switching loops of the BST/Cr-BST/CrSe device without FC. The device shows a switching current density of $J_{sw} = 5 \times 10^5 A/cm^2$, and no sign of magnetization switching can be observed at zero field. (b) Pulsed current switching loops after a positive FC of $H_x = +10$ kOe. The positive exchange-bias

breaks symmetry and the magnetization in the Cr-BST layer can be switched without the assistance of an external field. (c) Pulse-current switching loops after negative FC of $H_x = -10\,\mathrm{kOe}$. In this scenario, magnetization is switched with an opposite switching polarity at zero field due to a negative exchange-bias.

3.4. Field-Free Magnetization Switching at Elevated Temperatures in Topological Insulator/CrSb Heterostructures

3.4.1. Enhancement of Curie Temperature in Topological Insulator/CrSb Heterostructures

In Chapter 3.3, the AFM material we use for field-free switching by TI is CrSe. Apart from CrSe, another AFM material candidate that can provide exchange-bias and realize field-free switching is CrSb, which has a high Néel temperature of $T_N \approx 700\ K$.[*102, 111*] Our lab has adequate experience in growing CrSb film as well as related superlattices composed of TI and CrSb by MBE. High quality of the CrSb related structures and a sharp interface between TI and CrSb has been demonstrated in our previous work.[*102, 107*] To further study the SOT and field-free magnetization switching in TI/AFM systems, CrSb/Cr-BST heterostructure films with a thickness of 10 nm/10 nm were investigated. The crystalline and magnetic structure of CrSb as well as the schematic illustration of the CrSb/Cr-BST heterostructure are shown in Figure 3-9(a) and (b). For comparison, we grew another 10 nm-thick single-layer Cr-BST with similar film quality as a control sample. Both the CrSb/Cr-BST heterostructure and the Cr-BST control sample were fabricated into devices with Hall bar geometry (Figure 3-9(c)), and magneto-transport measurements were subsequently carried out to investigate their magnetic properties. Figure 3-9(d) displays the hysteresis loops of the Cr-BST control sample by Hall measurements at different temperatures. The hysteresis loop exhibits a pronounced coercivity of H_c=1.3 kOe at 2 K, which vanishes at ~30 K as the temperature increases. In comparison, the hysteresis loop of the CrSb/Cr-BST heterostructure has an enhanced coercivity that persists up to 100 K as shown in Figure 3-9(d). The coercivities of both samples are plotted as a function of temperature in Figure 3-9(e), where it can be noticed that the CrSb/Cr-BST heterostructure possesses a larger H_c and a T_c enhancement of more than 3 times. The enhancement of H_c and T_c can be attributed to the interfacial exchange-coupling between the CrSb layer and the Cr-BST layer, since the Néel order in the CrSb layer with a high T_N promotes the magnetization in the Cr-BST layer and raise its T_c. On the other hand, it also can be noticed that the hysteresis loop of the CrSb/Cr-BST heterostructure is more 'square-like' comparing to the single-layer Cr-BST film. As aforementioned, the 'squareness' of a hysteresis loop is a good indicator of the magnetic anisotropy of the magnetic material. Such a hysteresis loop suggests an enhancement of the perpendicular magnetic anisotropy in the Cr-BST film due to the perpendicular Néel order in the CrSb film.

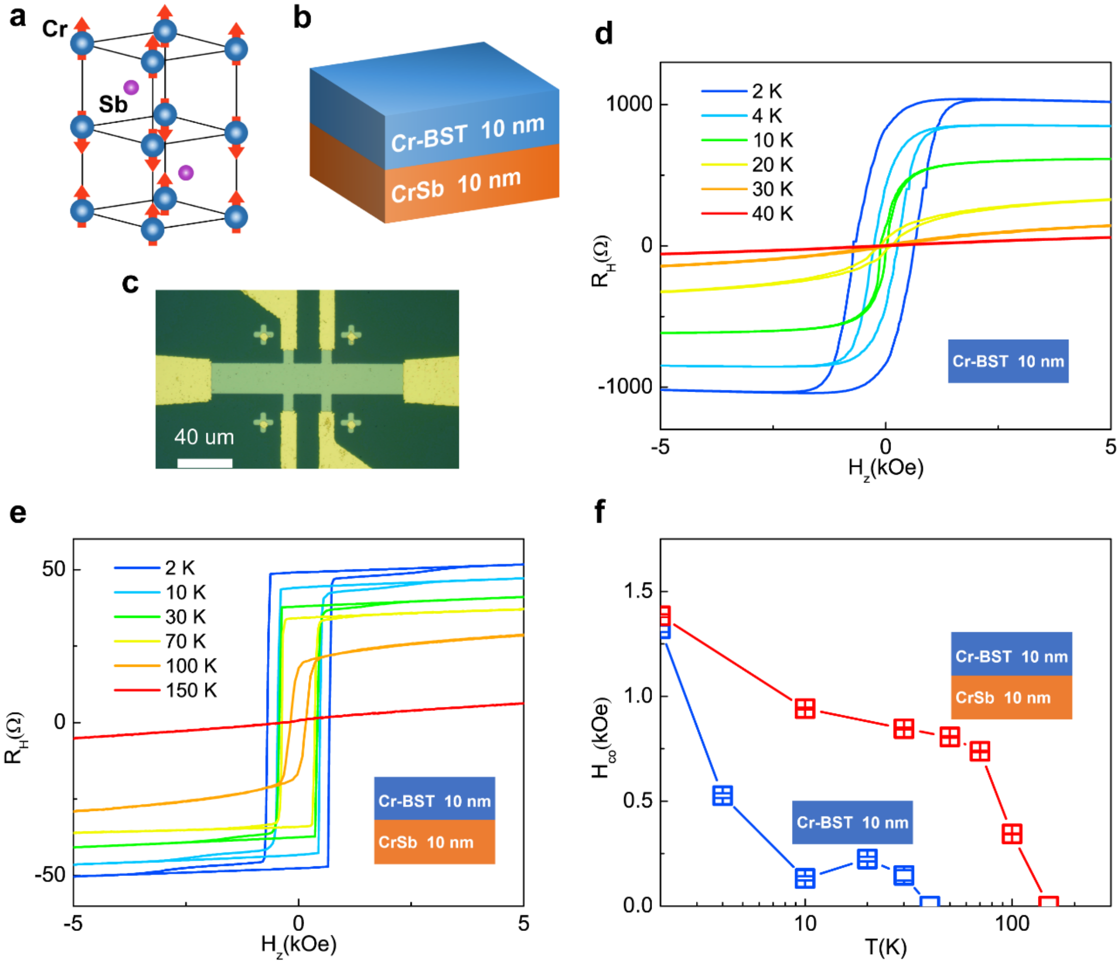

Figure 3-9. Schematic of the CrSb/Cr-BST heterostructure and enhancement of Curie temperature by interfacial exchange coupling. (a) Crystalline and magnetic structure of the CrSb unit cell. (b) Schematic illustration of the MBE-grown CrSb/Cr-BST heterostructure. (c) Hall bar device after fabrication for magneto-transport measurement. (d) Hysteresis loops of a 10 nm Cr-BST film in Hall measurement at different temperatures. (e) Hysteresis loops of the CrSb/Cr-BST heterostructure in Hall measurement at different temperatures. (f) Comparison of the coercivity between the Cr-BST film and the CrSb/Cr-BST heterostructure. The coercivity of the Cr-BST film vanishes ~30 K, while the coercivity of the CrSb/Cr-BST heterostructure persists up to 100 K.

3.4.2. Measuring Spin-Orbit Torque by Second Harmonic Method

To measure the SOT in the CrSb/Cr-BST heterostructure, experiments were subsequently carried out after investigating its magnetic properties. It has been demonstrated that second harmonic measurement is a reliable method to determine SOT, and such a method has been widely adopted in measuring SOT in different material systems.[*44, 112-114*] Here we also use the second harmonic method to quantify the SOT in the CrSb/Cr-BST heterostructure. In such measurement, an adequate in-plane magnetic field H_x needs to be applied to reorient the magnetization $\boldsymbol{m}$ of the sample toward the in-plane direction and achieve a single-domain magnetization configuration as displayed in Figure 3-10(a). An AC current I_{ac} with a frequency of ω is fed through the sample, inducing and alternating SOT and SOT effective field H_{eff} from TSS on the magnetization. The alternating SOT causes periodic oscillation of $\boldsymbol{m}$ around its equilibrium state in the same frequency ω, which is approximately equivalent to a periodic oscillation of its out-of-plane component Δm_z. Since Δm_z can be captured by the anomalous Hall resistance change ΔR_{AHE}, the current-induced voltage change in the Hall channel can be expressed as $V_H(t) = \Delta R_{AHE}(t) \times I(t)$. On the other hand, $I(t) \propto I_{ac}\cos(\omega t)$ and $\Delta R_{AHE}(t) \propto \Delta m_z(t) = \Delta m_z \cos(\omega t)$, $V_H(t) \propto \cos^2(\omega t) \propto \cos(2\omega t) + C$ and it becomes apparent that a second harmonic signal $V_H^{2\omega}$ with a frequency of 2ω manifest in the Hall channel. The relationship between the second harmonic Hall resistance $R_H^{2\omega}$ and SOT effective field H_{eff} can be established as

$$R_H^{2\omega} = -\frac{1}{2}\frac{R_{AHE}H_{eff}}{(|H_x|-K)} \qquad (3-1)$$

While H_{eff} can be extracted by adopting the above equation, the spin Hall angle can be determined by Equation 2-1 in Chapter 2.3.1. Figure 3-10(b) shows the second harmonic Hall resistance $R_H^{2\omega}$

measured under a sweeping in-plane magnetic field H_x and after applying current with different amplitudes at 100 K. It can be noticed that $R_H^{2\omega}$ increases with larger input I_{ac}, since a larger current density induces a stronger SOT on the magnetization and results in a higher second harmonic voltage. The extracted SOT effective field H^{eff} under different current density is summarized in Figure 3-10(c) by fitting to the $R_H^{2\omega}$ data using Equation 3-1, here the SOT effective field scales linearly with the current density, which generally rules out other thermal effects on the measurement result and clarifies the origin of the second harmonic signal since any thermal effect on the measured H^{eff} would scale with T or J^2. The second harmonic measurement was also carried out at 10 K, with the result shown in Figure 3-10(d) in comparison with the result at 100 K. $R_H^{2\omega}$ becomes more pronounced at 10 K, and the extracted spin Hall angle at 10 K is also around an order of magnitude higher than its value at 100 K. Such enhancement of the SOT at a lower temperature is consistent with our results in Chapter 2.4 and again suggests a critical role of TSS, in which the spin-polarization is strongly dependent on temperature.

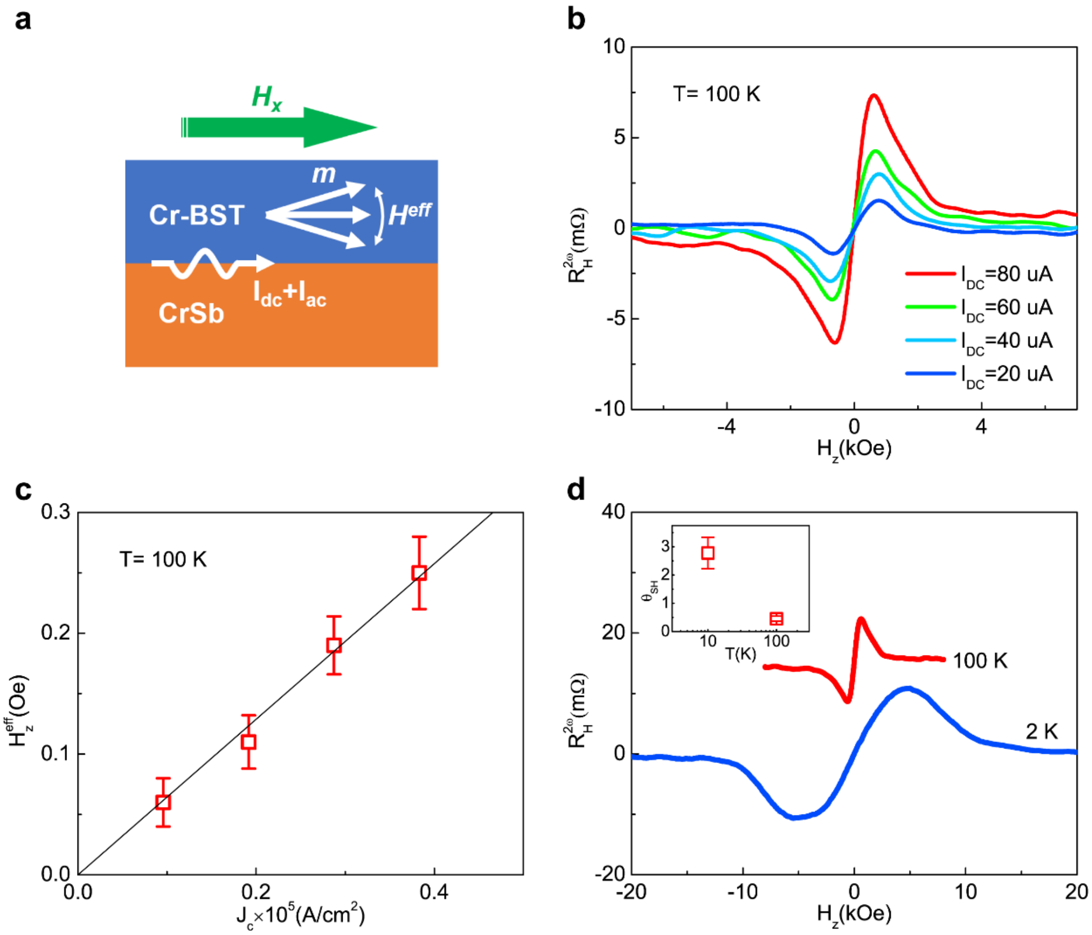

Figure 3-10. Determination of the SOT in the CrSb/Cr-BST heterostructure by second harmonic measurement. (a) Schematic illustration of the measurement principle. The AC current generates an alternating SOT on the magnetization, causing the magnetization to oscillate around its equilibrium state, and the magnetization oscillation is picked up by the second harmonic signal. (b) Second harmonic signal $R_H^{2\omega}$ measured when AC currents with different amplitudes were applied. $R_H^{2\omega}$ becomes more pronounced after increasing the current density due to a stronger SOT. (c) Extracted SOT effective field H_z^{eff} by fitting to the second harmonic measurement result, which scales linearly with current density. (d) Comparison of the second harmonic signal at 10 K and 100 K. Inset: extracted spin Hall angle at 10 K and 100 K, showing a much larger spin Hall angle at 10 K than at 100 K.

3.4.3. Field-Free Magnetization Switching at 100 K

As the goal of harnessing the TI/AFM structure is to realize field-free magnetization switching, pulsed current-driven switching tests were also carried out for the CrSb/Cr-BST heterostructure sample both with and without the assistance of external magnetic field. The switching tests were first carried out at 2 K, with the measurement result shown in Figure 3-11(a). It can be found that the magnetization of the Cr-BST layer can be successfully switched between ‘up’ and ‘down’ states by pulsed current under certain magnetic field. Due to the exchange-bias from the AFM CrSb layer that breaks symmetry, magnetization switching is still noticeable at zero field, and the switching loop vanishes under an in-plane field of -17 Oe where the external field compensates the exchange-bias from CrSb. Nonetheless, the anomalous Hall resistance change during the magnetization switching at zero field is much smaller (~2 Ω) comparing to the switching loop under ± 100 Oe (~7-9 Ω), indicating a low switching ratio at zero field. This can be explained by the fact that the Néel order of CrSb has an out-of-plane spin configuration. As a result, the interfacial uncompensated spins are also aligned in this direction with very little frustration toward other directions, which is not adequate to break symmetry in all the magnetic domains. Since it is possible that the interfacial uncompensated spins are frozen at 2 K and the spin frustration could be lifted at elevated temperature, magnetization switching tests were performed again at 100 K. Remarkably, field-free magnetization switching is observed and the switching ratio is comparable to the switching under positive and negative external field (Figure 3-11(b)). The switching loop vanishes under -300 Oe, which is much larger than the compensation field of -17 Oe at 2 K in

Figure 3-11(a) and suggests a stronger exchange-bias at 100 K potentially due to a larger spin-frustration.

For practical memory application, data retention is one of the most critical issues that are always required to be optimized. Specifically, it is crucial that the device should be able to retrieve the correct data after many read/write cycles. In order to preliminarily investigate the reliability of the CrSb/Cr-BST heterostructure device as a memory prototype, experimental tests of robustness were carried out for the device by repeating the write and read operations, i.e., applying current pulses and measure the magnetization state sequentially. As shown in Figure 3-11(c), the current pulses can switch the magnetization between ‘up’ state and ‘down’ state, and the stored data is still correct after a series of repeated operations. Although the number of cycles are still too small compared to commercial memory products, it shows the promise of TI-based structures as material candidates for fast and energy-efficient memory devices.

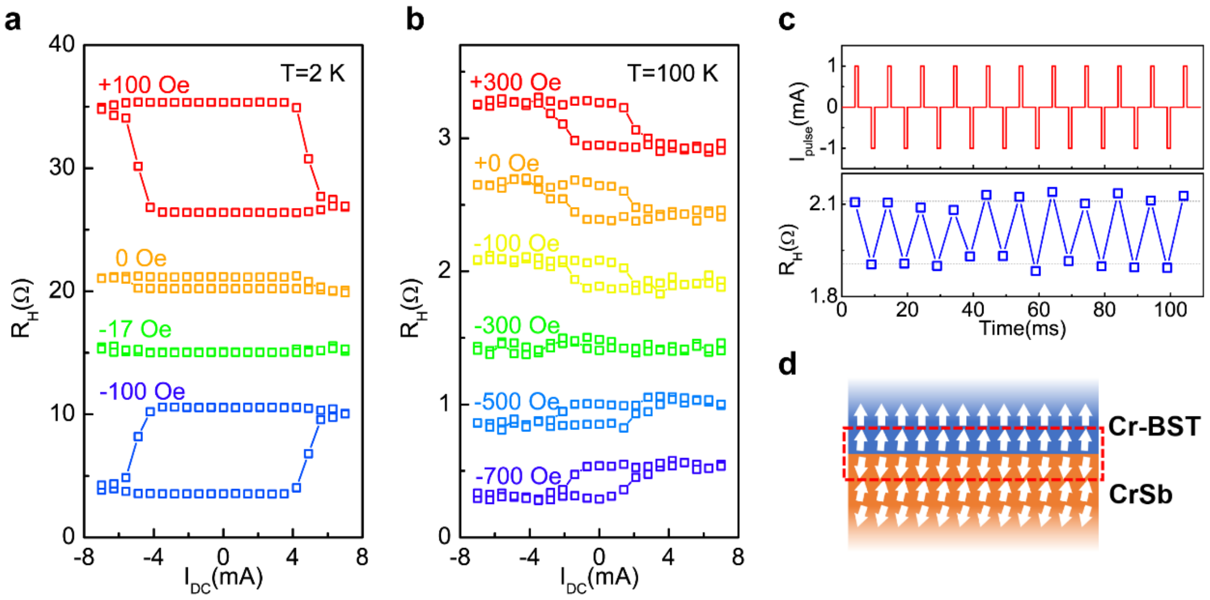

Figure 3-11. Robust field-free magnetization switching of the CrSb/Cr-BST heterostructure by pulse current. (a) Pulse-current driven magnetization switching at T=2 K. The magnetization switching at zero field is not pronounced due to a strong perpendicular AFM order in the CrSb layer at 2 K. (b) Pulse-current driven magnetization switching at T=100 K. The magnetization can be switched at zero field, and the exchange coupling is compensated by an in-plane field of -300 Oe where the switching loop vanishes. (c) Robustness test of the field-free magnetization switching. A series of current pulses were applied to switch the magnetization between ‘up’ state and ‘down’ state sequentially, and the magnetization state is probed by the anomalous Hall resistance after the current pulse. (d) Schematic illustration of the spin configuration in the CrSb/Cr-BST heterostructure.

3.5 Summary of Chapter 3

In summary, this chapter demonstrated SOT and field-free magnetization switching in TI/AFM systems with exchange-bias. A BST/CrSe heterostructure is firstly investigated, and exchange-bias both in the out-of-plane direction and in-plane direction are observed after FC. The spin-polarized surface state carriers can drive strong SOT on the proximity-induced magnetization at the interface. The SOT in this bilayer system is determined by the hysteresis loop shift method utilizing the in-plane exchange-bias from the CrSe layer. Detailed measurements of SOT with different DC current densities reveals a spin Hall angle of at least 5.3 and generally rule out artifact from thermal effect that would possibly disturb the measurement results. In a BST/Cr-BST/CrSe device with modulation-doped Cr near the interface, magnetization switching by pulsed current is achieved with a switching current density as low as $5 \times 10^5 A/cm^2$. Moreover, we realized field-free switching in this system by breaking the mirror symmetry of the magnetization with in-plane exchange-bias after in-plane FC. Apart from BST/CrSe heterostructure, another material system composed of CrSb and Cr-BST is investigated, which exhibits a much higher T_c as a result of the exchange-coupling. SOT efficiency in this system is also quantitatively determined by second harmonic measurements, showing a spin Hall angle of ~3. Moreover, in the CrSb/Cr-BST heterostructure field-free switching is achieved at an elevated temperature of ~100K, and the device is reliable after multiple cycles of read/write operations. The above results demonstrate that TI/AFM structure can be a promising candidate for more practical and energy-efficient magnetic memory devices.

Chapter 4

Summary and Perspective

In this dissertation, we explored the potential of utilizing the SOT in TI to switch magnetization for non-volatile magnetic memory applications. We systematically investigated the SOT in different material systems comprised of TIs via multiple independent approaches. Firstly, we quantitatively determined the strength of SOT in a Cr-BST/BST heterostructure by using the hysteresis loop shift method and a MOKE-based magnetometer, which demonstrated consistent values of the spin Hall angle θ_{SH}^{3D}. Furthermore, we carried out the measurements at different temperatures and studied the temperature dependence of θ_{SH}^{3D} in TI. The SOT measurements revealed a dramatic increase of θ_{SH}^{3D} at low temperature when the temperature is below 12 K, and such enhancement of θ_{SH}^{3D} suggests a strong dependence of the SOT on the temperature in TI systems. The significant increase of θ_{SH}^{3D} at low temperature can be further explained by a higher spin polarization ratio in the TSS owing to the suppression of electron-phonon scattering.

The dependence of SOT on TSS carrier concentrations was also investigated in a uniformly doped Cr-BST FET device with gate control. Through applying a gate voltage, the top TSS carrier concentration can be effectively controlled while the bottom TSS carrier concentration remains unchanged. In this manner, the contributions from both TSS to the SOT can be manipulated, and we observed a significant change of SOT as well as a competition between the top and bottom TSS to the SOT by tuning the gate voltage. The significant temperature dependence, carrier concentration dependence and the competition between the top and bottom TSS reveal an important role of both TSS in generating SOT. These phenomena could account for the large discrepancies among the reported value of θ_{SH}^{3D} in TI, providing an answer to the controversy on TSS-generated SOT in this field.

We also demonstrated SOT-driven magnetization switching in the Cr-BST/BST heterostructure. The magnetization switching is non-volatile and energy-efficient with low switching current density. However, it requires an in-plane magnetic field to break mirror symmetry for deterministic switching. To realize field-free magnetization switching, we further investigated TI/AFM systems where the exchange-bias at the interface can break mirror symmetry. A BST/CrSe heterostructure was firstly studied, where proximity-induced magnetization at the interface by the AFM CrSe layer was observed. Meanwhile, the BST/CrSe heterostructure exhibited exchange-bias after FC both in the out-of-plane and in-plane directions. The TSS spin polarization exert strong SOT on the magnetization at the interface, and the SOT was quantitatively measured by the hysteresis loop shift method. The measurements were performed systematically with different applied DC current densities to rule out artifacts from thermal effect. A spin Hall angle of at least $\theta_{SH} = 5.3$ was estimated, consistent with the previous measurement results in Cr-BST/BST heterostructures. After this, we studied a BST/Cr-BST/CrSe device with Cr doping near the interface to show an enhanced perpendicular anisotropy, and magnetization switching by pulsed current was achieved with a switching current density as low as $5 \times 10^5 A/cm^2$. Moreover, we demonstrated field-free switching in this system at T=1.9 K with the in-plane exchange-bias after FC to break mirror symmetry.

To improve the working temperature of the field-free magnetization switching with AFM, we utilized another AFM material, *i.e.*, CrSb that possesses a higher T_N of ~700 K. A Cr-BST/CrSb heterostructure was synthesized, exhibiting a much higher T_c due to the exchange-coupling between Cr-BST and CrSb at the interface. Second harmonic measurements were carried out to determine the SOT in this system, giving a spin Hall angle of ~3. More importantly, we also achieved field-free switching in the CrSb/Cr-BST heterostructure and at an elevated temperature of ~100K. The device was shown to work reliably after multiple reading/writing cycles.

The above results demonstrated that magnetically doped TI-based material systems could be a promising candidate for fast, non-volatile and energy-efficient magnetic memory devices. Particularly, TI/AFM structures can offer field-free magnetization switching to implement practical magnetic memory prototypes. However, several issues still remain in utilizing TI for memory applications. First of all, the working temperature of magnetization switching in magnetically doped TIs is still in the low-temperature range. Secondly, the switching ratio of the magnetization is quite small implied by the anomalous Hall resistance, and the reliability of the devices in switching/reading needs to be further tested and optimized. Lastly, the material structures we investigated were synthesized by using the MBE technique. For commercialized products, CVD synthesis of materials may be further developed to assure high quality. Future works could focus on tackling these issues by synthesizing TI/FM structures with robust perpendicular magnetization at high temperature for room-temperature application. The device reliability could also be enhanced by adopting magnetic materials with stronger magnetization and faster magnetic dynamics (*e.g.*, ferrimagnetic materials). To achieve compatibility with other semiconductor process procedures and mass production, sputtering deposition of TI and FM layers could be used instead of MBE epitaxial growth. However, the quality of TI films will need to be addressed. In addition, thermal budget among multiple processing steps needs to be carefully considered as well.

The past decades have witnessed the unprecedented prosperity of information technology, communication, productivity, and entertainment brought by tiny semiconductor chips. Now we are fortunate enough again to see another new era of artificial intelligence, internet of things and cloud services, where memories will play an increasingly crucial role in storing the massive data beyond what we can imagine. I am glad to see that magnetic memory based on TI can be a pioneer in the future to offer fast, reliable, high-density, and energy-efficient data storage devices for these applications in the future.

Reference

[1] A. Fert, "Nobel Lecture: Origin, development, and future of spintronics". *Reviews of Modern Physics* **80**, 1517-1530 (2008).

[2] S. Bhatti, R. Sbiaa, A. Hirohata, H. Ohno, S. Fukami, S. N. Piramanayagam, "Spintronics based random access memory: a review". *Materials Today* **20**, 530-548 (2017).

[3] M. N. Baibich, J. M. Broto, A. Fert, F. Nguyen Van Dau, F. Petroff, P. Etienne, G. Creuzet, A. Friederich, J. Chazelas, "Giant magnetoresistance of (001)Fe/(001)Cr magnetic superlattices". *Phys Rev Lett* **61**, 2472-2475 (1988).

[4] G. Binasch, P. Grunberg, F. Saurenbach, W. Zinn, "Enhanced magnetoresistance in layered magnetic structures with antiferromagnetic interlayer exchange". *Phys Rev B Condens Matter* **39**, 4828-4830 (1989).

[5] D. C. Ralph, M. D. Stiles, "Spin transfer torques". *Journal of Magnetism and Magnetic Materials* **320**, 1190-1216 (2008).

[6] A. Brataas, A. D. Kent, H. Ohno, "Current-induced torques in magnetic materials". *Nat Mater* **11**, 372-381 (2012).

[7] J. C. Slonczewski, "Current-driven excitation of magnetic multilayers". *Journal of Magnetism and Magnetic Materials* **159**, L1-L7 (1996).

[8] G. V. Skrotskiĭ, "The Landau-Lifshitz equation revisited". *Soviet Physics Uspekhi* **27**, 977-979 (1984).

[9] K. L. Wang, H. Wu, S. A. Razavi, Q. Shao, "Spintronic devices for low energy dissipation". *2018 Ieee International Electron Devices Meeting (Iedm)*, 36.32.31-36.32.34 (2018).

[10] Y. Huai, "Spin-transfer torque MRAM (STT-MRAM): Challenges and prospects". *AAPPS bulletin* **18**, 33-40 (2008).

[11] M. Z. Hasan, C. L. Kane, "Colloquium: Topological insulators". *Reviews of Modern Physics* **82**, 3045-3067 (2010).

[12] J. E. Hirsch, "Spin Hall Effect". *Physical review letters* **83**, 1834-1837 (1999).

[13] S. Zhang, "Spin hall effect in the presence of spin diffusion". *Phys Rev Lett* **85**, 393-396 (2000).

[14] Y. K. Kato, R. C. Myers, A. C. Gossard, D. D. Awschalom, "Observation of the spin Hall effect in semiconductors". *Science* **306**, 1910-1913 (2004).

[15] Y. A. Bychkov, E. I. Rashba, "Properties of a 2d Electron-Gas with Lifted Spectral Degeneracy". *Jetp Letters* **39**, 78-81 (1984).

[16] V. M. Edelstein, "Spin polarization of conduction electrons induced by electric current in two-dimensional asymmetric electron systems". *Solid State Communications* **73**, 233-235 (1990).

[17] L. Liu, C. F. Pai, Y. Li, H. W. Tseng, D. C. Ralph, R. A. Buhrman, "Spin-torque switching with the giant spin Hall effect of tantalum". *Science* **336**, 555-558 (2012).

[18] I. M. Miron, G. Gaudin, S. Auffret, B. Rodmacq, A. Schuhl, S. Pizzini, J. Vogel, P. Gambardella, "Current-driven spin torque induced by the Rashba effect in a ferromagnetic metal layer". *Nat Mater* **9**, 230-234 (2010).

[19] S. Maekawa, "Magnetism: A flood of spin current". *Nat Mater* **8**, 777-778 (2009).

[20] A. Soumyanarayanan, N. Reyren, A. Fert, C. Panagopoulos, "Emergent phenomena induced by spin-orbit coupling at surfaces and interfaces". *Nature* **539**, 509-517 (2016).

[21] L. Liu, T. Moriyama, D. C. Ralph, R. A. Buhrman, "Spin-torque ferromagnetic resonance induced by the spin Hall effect". *Phys Rev Lett* **106**, 036601 (2011).

[22] I. M. Miron, K. Garello, G. Gaudin, P. J. Zermatten, M. V. Costache, S. Auffret, S. Bandiera, B. Rodmacq, A. Schuhl, P. Gambardella, "Perpendicular switching of a single ferromagnetic layer induced by in-plane current injection". *Nature* **476**, 189-193 (2011).

[23] K. v. Klitzing, G. Dorda, M. Pepper, "New Method for High-Accuracy Determination of the Fine-Structure Constant Based on Quantized Hall Resistance". *Physical review letters* **45**, 494-497 (1980).

[24] R. B. Laughlin, "Quantized Hall conductivity in two dimensions". *Physical Review B* **23**, 5632-5633 (1981).

[25] D. K. Ferry, "The quantum Hall effect". *IOP Publishing Ltd*, (2014).

[26] K. von Klitzing, "Quantum Hall Effect: Discovery and Application". *Annual Review of Condensed Matter Physics* **8**, 13-30 (2017).

[27] C. L. Kane, E. J. Mele, "Quantum spin Hall effect in graphene". *Phys Rev Lett* **95**, 226801 (2005).

[28] C. L. Kane, E. J. Mele, "Z2 topological order and the quantum spin Hall effect". *Phys Rev Lett* **95**, 146802 (2005).

[29] F. D. Haldane, "Model for a quantum Hall effect without Landau levels: Condensed-matter realization of the "parity anomaly"". *Phys Rev Lett* **61**, 2015-2018 (1988).

[30] C. L. Kane, E. J. Mele, "Physics. A new spin on the insulating state". *Science* **314**, 1692-1693 (2006).

[31] B. A. Bernevig, S. C. Zhang, "Quantum spin Hall effect". *Phys Rev Lett* **96**, 106802 (2006).

[32] B. A. Bernevig, T. L. Hughes, S. C. Zhang, "Quantum spin Hall effect and topological phase transition in HgTe quantum wells". *Science* **314**, 1757-1761 (2006).

[33] M. Konig, S. Wiedmann, C. Brune, A. Roth, H. Buhmann, L. W. Molenkamp, X. L. Qi, S. C. Zhang, "Quantum spin hall insulator state in HgTe quantum wells". *Science* **318**, 766-770 (2007).

[34] L. Fu, C. L. Kane, "Topological insulators with inversion symmetry". *Physical Review B* **76**, (2007).

[35] L. Fu, C. L. Kane, E. J. Mele, "Topological insulators in three dimensions". *Phys Rev Lett* **98**, 106803 (2007).

[36] J. E. Moore, "The birth of topological insulators". *Nature* **464**, 194-198 (2010).

[37] H. J. Zhang, C. X. Liu, X. L. Qi, X. Dai, Z. Fang, S. C. Zhang, "Topological insulators in Bi_2Se_3, Bi_2Te_3 and Sb_2Te_3 with a single Dirac cone on the surface". *Nature Physics* **5**, 438-442 (2009).

[38] Y. L. Chen, J. G. Analytis, J. H. Chu, Z. K. Liu, S. K. Mo, X. L. Qi, H. J. Zhang, D. H. Lu, X. Dai, Z. Fang, S. C. Zhang, I. R. Fisher, Z. Hussain, Z. X. Shen, "Experimental realization of a three-dimensional topological insulator, Bi_2Te_3". *Science* **325**, 178-181 (2009).

[39] D. Hsieh, Y. Xia, D. Qian, L. Wray, J. H. Dil, F. Meier, J. Osterwalder, L. Patthey, J. G. Checkelsky, N. P. Ong, A. V. Fedorov, H. Lin, A. Bansil, D. Grauer, Y. S. Hor, R. J. Cava, M. Z. Hasan, "A tunable topological insulator in the spin helical Dirac transport regime". *Nature* **460**, 1101-1105 (2009).

[40] Y. Xia, D. Qian, D. Hsieh, L. Wray, A. Pal, H. Lin, A. Bansil, D. Grauer, Y. S. Hor, R. J. Cava, M. Z. Hasan, "Observation of a large-gap topological-insulator class with a single Dirac cone on the surface". *Nature Physics* **5**, 398-402 (2009).

[41] C. Jozwiak, Y. L. Chen, A. V. Fedorov, J. G. Analytis, C. R. Rotundu, A. K. Schmid, J. D. Denlinger, Y. D. Chuang, D. H. Lee, I. R. Fisher, R. J. Birgeneau, Z. X. Shen, Z. Hussain, A. Lanzara, "Widespread spin polarization effects in photoemission from topological insulators". *Physical Review B* **84**, (2011).

[42] C. H. Li, O. M. van 't Erve, J. T. Robinson, Y. Liu, L. Li, B. T. Jonker, "Electrical detection of charge-current-induced spin polarization due to spin-momentum locking in Bi_2Se_3". *Nat Nanotechnol* **9**, 218-224 (2014).

[43] J. Tang, L. T. Chang, X. Kou, K. Murata, E. S. Choi, M. Lang, Y. Fan, Y. Jiang, M. Montazeri, W. Jiang, Y. Wang, L. He, K. L. Wang, "Electrical detection of spin-polarized surface states conduction in (Bi(0.53)Sb(0.47))2Te3 topological insulator". *Nano Lett* **14**, 5423-5429 (2014).

[44] Y. Fan, P. Upadhyaya, X. Kou, M. Lang, S. Takei, Z. Wang, J. Tang, L. He, L. T. Chang, M. Montazeri, G. Yu, W. Jiang, T. Nie, R. N. Schwartz, Y. Tserkovnyak, K. L. Wang, "Magnetization switching through giant spin-orbit torque in a magnetically doped topological insulator heterostructure". *Nat Mater* **13**, 699-704 (2014).

[45] A. R. Mellnik, J. S. Lee, A. Richardella, J. L. Grab, P. J. Mintun, M. H. Fischer, A. Vaezi, A. Manchon, E. A. Kim, N. Samarth, D. C. Ralph, "Spin-transfer torque generated by a topological insulator". *Nature* **511**, 449-451 (2014).

[46] Y. Fan, X. Kou, P. Upadhyaya, Q. Shao, L. Pan, M. Lang, X. Che, J. Tang, M. Montazeri, K. Murata, L. T. Chang, M. Akyol, G. Yu, T. Nie, K. L. Wong, J. Liu, Y. Wang, Y. Tserkovnyak, K. L. Wang, "Electric-field control of spin-orbit torque in a magnetically doped topological insulator". *Nat Nanotechnol* **11**, 352-359 (2016).

[47] J. Han, A. Richardella, S. A. Siddiqui, J. Finley, N. Samarth, L. Liu, "Room-Temperature Spin-Orbit Torque Switching Induced by a Topological Insulator". *Phys Rev Lett* **119**, 077702 (2017).

[48] M. Jamali, J. S. Lee, J. S. Jeong, F. Mahfouzi, Y. Lv, Z. Zhao, B. K. Nikolic, K. A. Mkhoyan, N. Samarth, J. P. Wang, "Giant Spin Pumping and Inverse Spin Hall Effect in the Presence of Surface and Bulk Spin-Orbit Coupling of Topological Insulator Bi2Se3". *Nano Lett* **15**, 7126-7132 (2015).

[49] J. Tian, I. Childres, H. Cao, T. Shen, I. Miotkowski, Y. P. Chen, "Topological insulator based spin valve devices: Evidence for spin polarized transport of spin-momentum-locked topological surface states". *Solid State Communications* **191**, 1-5 (2014).

[50] Y. Yang, B. Wu, K. Yao, S. Shannigrahi, B. Zong, Y. Wu, "Investigation of magnetic proximity effect in Ta/YIG bilayer Hall bar structure". *Journal of Applied Physics* **115**, 17C509 (2014).

[51] W. D. Luo, X. L. Qi, "Massive Dirac surface states in topological insulator/magnetic insulator heterostructures". *Physical Review B* **87**, (2013).

[52] S. V. Eremeev, V. N. Men'shov, V. V. Tugushev, P. M. Echenique, E. V. Chulkov, "Magnetic proximity effect at the three-dimensional topological insulator/magnetic insulator interface". *Physical Review B* **88**, 144430 (2013).

[53] P. Wei, F. Katmis, B. A. Assaf, H. Steinberg, P. Jarillo-Herrero, D. Heiman, J. S. Moodera, "Exchange-coupling-induced symmetry breaking in topological insulators". *Phys Rev Lett* **110**, 186807 (2013).

[54] G. Xu, J. Wang, C. Felser, X. L. Qi, S. C. Zhang, "Quantum anomalous Hall effect in magnetic insulator heterostructure". *Nano Lett* **15**, 2019-2023 (2015).

[55] F. Katmis, V. Lauter, F. S. Nogueira, B. A. Assaf, M. E. Jamer, P. Wei, B. Satpati, J. W. Freeland, I. Eremin, D. Heiman, P. Jarillo-Herrero, J. S. Moodera, "A high-temperature ferromagnetic topological insulating phase by proximity coupling". *Nature* **533**, 513-516 (2016).

[56] M. Lang, M. Montazeri, M. C. Onbasli, X. Kou, Y. Fan, P. Upadhyaya, K. Yao, F. Liu, Y. Jiang, W. Jiang, K. L. Wong, G. Yu, J. Tang, T. Nie, L. He, R. N. Schwartz, Y. Wang, C. A. Ross, K. L. Wang, "Proximity induced high-temperature magnetic order in topological insulator--ferrimagnetic insulator heterostructure". *Nano Lett* **14**, 3459-3465 (2014).

[57] Z. Jiang, F. Katmis, C. Tang, P. Wei, J. S. Moodera, J. Shi, "A comparative transport study of Bi_2Se_3 and Bi_2Se_3/yttrium iron garnet". *Applied Physics Letters* **104**, 222409 (2014).

[58] Z. Jiang, C. Z. Chang, C. Tang, P. Wei, J. S. Moodera, J. Shi, "Independent Tuning of Electronic Properties and Induced Ferromagnetism in Topological Insulators with Heterostructure Approach". *Nano Lett* **15**, 5835-5840 (2015).

[59] M. Li, C. Z. Chang, B. J. Kirby, M. E. Jamer, W. Cui, L. Wu, P. Wei, Y. Zhu, D. Heiman, J. Li, J. S. Moodera, "Proximity-Driven Enhanced Magnetic Order at Ferromagnetic-Insulator-Magnetic-Topological-Insulator Interface". *Phys Rev Lett* **115**, 087201 (2015).

[60] Y. T. Fanchiang, K. H. M. Chen, C. C. Tseng, C. C. Chen, C. K. Cheng, S. R. Yang, C. N. Wu, S. F. Lee, M. Hong, J. Kwo, "Strongly exchange-coupled and surface-state-modulated magnetization dynamics in Bi_2Se_3/yttrium iron garnet heterostructures". *Nat Commun* **9**, 223 (2018).

[61] H. Wang, J. Kally, J. S. Lee, T. Liu, H. Chang, D. R. Hickey, K. A. Mkhoyan, M. Wu, A. Richardella, N. Samarth, "Surface-State-Dominated Spin-Charge Current Conversion in Topological-Insulator-Ferromagnetic-Insulator Heterostructures". *Phys Rev Lett* **117**, 076601 (2016).

[62] C. Z. Chang, K. He, L. L. Wang, X. C. Ma, M. H. Liu, Z. C. Zhang, X. Chen, Y. Y. Wang, Q. K. Xue, "GROWTH OF QUANTUM WELL FILMS OF TOPOLOGICAL INSULATOR Bi_2Se_3 ON INSULATING SUBSTRATE". *Spin* **1**, 21-25 (2011).

[63] N. Bansal, Y. S. Kim, M. Brahlek, E. Edrey, S. Oh, "Thickness-independent transport channels in topological insulator Bi(2)Se(3) thin films". *Phys Rev Lett* **109**, 116804 (2012).

[64] A. A. Taskin, S. Sasaki, K. Segawa, Y. Ando, "Manifestation of topological protection in transport properties of epitaxial Bi_2Se_3 thin films". *Phys Rev Lett* **109**, 066803 (2012).

[65] Y. Zhao, C. Z. Chang, Y. Jiang, A. DaSilva, Y. Sun, H. Wang, Y. Xing, Y. Wang, K. He, X. Ma, Q. K. Xue, J. Wang, "Demonstration of surface transport in a hybrid Bi_2Se_3/Bi_2Te_3 heterostructure". *Sci Rep* **3**, 3060 (2013).

[66] N. Bansal, M. R. Cho, M. Brahlek, N. Koirala, Y. Horibe, J. Chen, W. Wu, Y. D. Park, S. Oh, "Transferring MBE-grown topological insulator films to arbitrary substrates and metal-insulator transition via Dirac gap". *Nano Lett* **14**, 1343-1348 (2014).

[67] F. Yang, A. A. Taskin, S. Sasaki, K. Segawa, Y. Ohno, K. Matsumoto, Y. Ando, "Dual-gated topological insulator thin-film device for efficient Fermi-level tuning". *ACS Nano* **9**, 4050-4055 (2015).

[68] K. He, Y. Zhang, K. He, C.-Z. Chang, C.-L. Song, L.-L. Wang, X. Chen, J.-F. Jia, Z. Fang, X. Dai, W.-Y. Shan, S.-Q. Shen, Q. Niu, X.-L. Qi, S.-C. Zhang, X.-C. Ma, Q.-K. Xue, "Crossover of the three-dimensional topological insulator Bi_2Se_3 to the two-dimensional limit". *Nature Physics* **6**, 584-588 (2010).

[69] M. Lang, L. He, X. Kou, P. Upadhyaya, Y. Fan, H. Chu, Y. Jiang, J. H. Bardarson, W. Jiang, E. S. Choi, Y. Wang, N. C. Yeh, J. Moore, K. L. Wang, "Competing weak localization and weak antilocalization in ultrathin topological insulators". *Nano Lett* **13**, 48-53 (2013).

[70] X. Che, K. Murata, L. Pan, Q. L. He, G. Yu, Q. Shao, G. Yin, P. Deng, Y. Fan, B. Ma, X. Liang, B. Zhang, X. Han, L. Bi, Q. H. Yang, H. Zhang, K. L. Wang, "Proximity-Induced Magnetic Order in a Transferred Topological Insulator Thin Film on a Magnetic Insulator". *ACS Nano* **12**, 5042-5050 (2018).

[71] C. Tang, C. Z. Chang, G. Zhao, Y. Liu, Z. Jiang, C. X. Liu, M. R. McCartney, D. J. Smith, T. Chen, J. S. Moodera, J. Shi, "Above 400-K robust perpendicular ferromagnetic phase in a topological insulator". *Sci Adv* **3**, e1700307 (2017).

[72] S. Y. Huang, X. Fan, D. Qu, Y. P. Chen, W. G. Wang, J. Wu, T. Y. Chen, J. Q. Xiao, C. L. Chien, "Transport magnetic proximity effects in platinum". *Phys Rev Lett* **109**, 107204 (2012).

[73] Z. Wang, C. Tang, R. Sachs, Y. Barlas, J. Shi, "Proximity-induced ferromagnetism in graphene revealed by the anomalous Hall effect". *Phys Rev Lett* **114**, 016603 (2015).

[74] Y. H. Choi, N. H. Jo, K. J. Lee, J. B. Yoon, C. Y. You, M. H. Jung, "Transport and magnetic properties of Cr-, Fe-, Cu-doped topological insulators". *Journal of Applied Physics* **109**, 07E312 (2011).

[75] X. Kou, L. He, M. Lang, Y. Fan, K. Wong, Y. Jiang, T. Nie, W. Jiang, P. Upadhyaya, Z. Xing, Y. Wang, F. Xiu, R. N. Schwartz, K. L. Wang, "Manipulating surface-related ferromagnetism in modulation-doped topological insulators". *Nano Lett* **13**, 4587-4593 (2013).

[76] P. P. J. Haazen, J. B. Laloe, T. J. Nummy, H. J. M. Swagten, P. Jarillo-Herrero, D. Heiman, J. S. Moodera, "Ferromagnetism in thin-film Cr-doped topological insulator Bi_2Se_3". *Applied Physics Letters* **100**, 082404 (2012).

[77] X. Kou, S. T. Guo, Y. Fan, L. Pan, M. Lang, Y. Jiang, Q. Shao, T. Nie, K. Murata, J. Tang, Y. Wang, L. He, T. K. Lee, W. L. Lee, K. L. Wang, "Scale-invariant quantum anomalous Hall effect in magnetic topological insulators beyond the two-dimensional limit". *Phys Rev Lett* **113**, 137201 (2014).

[78] X. Kou, L. Pan, J. Wang, Y. Fan, E. S. Choi, W. L. Lee, T. Nie, K. Murata, Q. Shao, S. C. Zhang, K. L. Wang, "Metal-to-insulator switching in quantum anomalous Hall states". *Nat Commun* **6**, 8474 (2015).

[79] X. Che, Q. Pan, B. Vareskic, J. Zou, L. Pan, P. Zhang, G. Yin, H. Wu, Q. Shao, P. Deng, K. L. Wang, "Strongly Surface State Carrier-Dependent Spin-Orbit Torque in Magnetic Topological Insulators". *Adv Mater* **32**, e1907661 (2020).

[80] A. Fert, V. Cros, J. Sampaio, "Skyrmions on the track". *Nat Nanotechnol* **8**, 152-156 (2013).

[81] K. Yasuda, R. Wakatsuki, T. Morimoto, R. Yoshimi, A. Tsukazaki, K. S. Takahashi, M. Ezawa, M. Kawasaki, N. Nagaosa, Y. Tokura, "Geometric Hall effects in topological insulator heterostructures". *Nature Physics* **12**, 555-559 (2016).

[82] Q. L. He, G. Yin, A. J. Grutter, L. Pan, X. Che, G. Yu, D. A. Gilbert, S. M. Disseler, Y. Liu, P. Shafer, B. Zhang, Y. Wu, B. J. Kirby, E. Arenholz, R. K. Lake, X. Han, K. L. Wang, "Exchange-biasing topological charges by antiferromagnetism". *Nat Commun* **9**, 2767 (2018).

[83] G. Yu, P. Upadhyaya, Y. Fan, J. G. Alzate, W. Jiang, K. L. Wong, S. Takei, S. A. Bender, L. T. Chang, Y. Jiang, M. Lang, J. Tang, Y. Wang, Y. Tserkovnyak, P. K. Amiri, K. L. Wang, "Switching of perpendicular magnetization by spin-orbit torques in the absence of external magnetic fields". *Nat Nanotechnol* **9**, 548-554 (2014).

[84] C. Liu, Y. Zang, W. Ruan, Y. Gong, K. He, X. Ma, Q. K. Xue, Y. Wang, "Dimensional Crossover-Induced Topological Hall Effect in a Magnetic Topological Insulator". *Phys Rev Lett* **119**, 176809 (2017).

[85] K. Kondou, R. Yoshimi, A. Tsukazaki, Y. Fukuma, J. Matsuno, K. S. Takahashi, M. Kawasaki, Y. Tokura, Y. Otani, "Fermi-level-dependent charge-to-spin current conversion by Dirac surface states of topological insulators". *Nature Physics* **12**, 1027-1031 (2016).

[86] Y. Wang, D. Zhu, Y. Wu, Y. Yang, J. Yu, R. Ramaswamy, R. Mishra, S. Shi, M. Elyasi, K. L. Teo, Y. Wu, H. Yang, "Room temperature magnetization switching in topological insulator-ferromagnet heterostructures by spin-orbit torques". *Nat Commun* **8**, 1364 (2017).

[87] M. Montazeri, P. Upadhyaya, M. C. Onbasli, G. Yu, K. L. Wong, M. Lang, Y. Fan, X. Li, P. Khalili Amiri, R. N. Schwartz, C. A. Ross, K. L. Wang, "Magneto-optical investigation of spin-orbit torques in metallic and insulating magnetic heterostructures". *Nat Commun* **6**, 8958 (2015).

[88] M. Straub, R. Vollmer, J. Kirschner, "Surface Magnetism of Ultrathin gamma -Fe Films Investigated by Nonlinear Magneto-optical Kerr Effect". *Phys Rev Lett* **77**, 743-746 (1996).

[89] J. Hamrle, S. Blomeier, O. Gaier, B. Hillebrands, H. Schneider, G. Jakob, K. Postava, C. Felser, "Huge quadratic magneto-optical Kerr effect and magnetization reversal in the Co2FeSi Heusler compound". *Journal of Physics D: Applied Physics* **40**, 1563-1569 (2007).

[90] Y. Wang, P. Deorani, X. Qiu, J. H. Kwon, H. Yang, "Determination of intrinsic spin Hall angle in Pt". *Applied Physics Letters* **105**, 152412 (2014).

[91] R. L. Liboff, G. K. Schenter, "Electron-phonon scattering contributions to metallic resistivity at 0 K". *Physical Review B* **54**, 16591-16601 (1996).

[92] S. Fukami, C. Zhang, S. DuttaGupta, A. Kurenkov, H. Ohno, "Magnetization switching by spin-orbit torque in an antiferromagnet-ferromagnet bilayer system". *Nat Mater* **15**, 535-541 (2016).

[93] D. Wu, G. Yu, Q. Shao, X. Li, H. Wu, K. L. Wong, Z. Zhang, X. Han, P. Khalili Amiri, K. L. Wang, "In-plane current-driven spin-orbit torque switching in perpendicularly magnetized films with enhanced thermal tolerance". *Applied Physics Letters* **108**, 212406 (2016).

[94] K.-S. Lee, S.-W. Lee, B.-C. Min, K.-J. Lee, "Threshold current for switching of a perpendicular magnetic layer induced by spin Hall effect". *Applied Physics Letters* **102**, 112410 (2013).

[95] S. Fukami, T. Anekawa, C. Zhang, H. Ohno, "A spin-orbit torque switching scheme with collinear magnetic easy axis and current configuration". *Nat Nanotechnol* **11**, 621-625 (2016).

[96] A. Manchon, J. Železný, I. M. Miron, T. Jungwirth, J. Sinova, A. Thiaville, K. Garello, P. Gambardella, "Current-induced spin-orbit torques in ferromagnetic and antiferromagnetic systems". *Reviews of Modern Physics* **91**, (2019).

[97] C. K. Safeer, E. Jue, A. Lopez, L. Buda-Prejbeanu, S. Auffret, S. Pizzini, O. Boulle, I. M. Miron, G. Gaudin, "Spin-orbit torque magnetization switching controlled by geometry". *Nat Nanotechnol* **11**, 143-146 (2016).

[98] Y. C. Lau, D. Betto, K. Rode, J. M. Coey, P. Stamenov, "Spin-orbit torque switching without an external field using interlayer exchange coupling". *Nat Nanotechnol* **11**, 758-762 (2016).

[99] S. A. Razavi, D. Wu, G. Yu, Y.-C. Lau, K. L. Wong, W. Zhu, C. He, Z. Zhang, J. M. D. Coey, P. Stamenov, P. Khalili Amiri, K. L. Wang, "Joule Heating Effect on Field-Free Magnetization Switching by Spin-Orbit Torque in Exchange-Biased Systems". *Physical Review Applied* **7**, (2017).

[100] Y. W. Oh, S. H. Chris Baek, Y. M. Kim, H. Y. Lee, K. D. Lee, C. G. Yang, E. S. Park, K. S. Lee, K. W. Kim, G. Go, J. R. Jeong, B. C. Min, H. W. Lee, K. J. Lee, B. G. Park, "Field-free switching of perpendicular magnetization through spin-orbit torque in antiferromagnet/ferromagnet/oxide structures". *Nat Nanotechnol* **11**, 878-884 (2016).

[101] A. van den Brink, G. Vermijs, A. Solignac, J. Koo, J. T. Kohlhepp, H. J. M. Swagten, B. Koopmans, "Field-free magnetization reversal by spin-Hall effect and exchange bias". *Nat Commun* **7**, 10854 (2016).

[102] Q. L. He, X. Kou, A. J. Grutter, G. Yin, L. Pan, X. Che, Y. Liu, T. Nie, B. Zhang, S. M. Disseler, B. J. Kirby, W. Ratcliff Ii, Q. Shao, K. Murata, X. Zhu, G. Yu, Y. Fan, M. Montazeri, X. Han, J. A. Borchers, K. L. Wang, "Tailoring exchange couplings in magnetic topological-insulator/antiferromagnet heterostructures". *Nat Mater* **16**, 94-100 (2017).

[103] J. Nogués, J. Sort, V. Langlais, V. Skumryev, S. Suriñach, J. S. Muñoz, M. D. Baró, "Exchange bias in nanostructures". *Physics Reports* **422**, 65-117 (2005).

[104] R. L. Stamps, "Mechanisms for exchange bias". *Journal of Physics D: Applied Physics* **33**, R247-R268 (2000).

[105] L. M. Corliss, N. Elliott, J. M. Hastings, R. L. Sass, "Magnetic Structure of Chromium Selenide". *Physical Review* **122**, 1402-1406 (1961).

[106] S. Polesya, S. Mankovsky, D. Benea, H. Ebert, W. Bensch, "Finite-temperature magnetism of CrTe and CrSe". *Journal of physics. Condensed matter : an Institute of Physics journal* **22**, 156002 (2010).

[107] Q. L. He, G. Yin, L. Yu, A. J. Grutter, L. Pan, C. Z. Chen, X. Che, G. Yu, B. Zhang, Q. Shao, A. L. Stern, B. Casas, J. Xia, X. Han, B. J. Kirby, R. K. Lake, K. T. Law, K. L. Wang, "Topological Transitions Induced by Antiferromagnetism in a Thin-Film Topological Insulator". *Phys Rev Lett* **121**, 096802 (2018).

[108] C. Leighton, M. R. Fitzsimmons, A. Hoffmann, J. Dura, C. F. Majkrzak, M. S. Lund, I. K. Schuller, "Thickness-dependent coercive mechanisms in exchange-biased bilayers". *Physical Review B* **65**, (2002).

[109] C.-F. Pai, M. Mann, A. J. Tan, G. S. D. Beach, "Determination of spin torque efficiencies in heterostructures with perpendicular magnetic anisotropy". *Physical Review B* **93**, (2016).

[110] H. Wu, Y. Xu, P. Deng, Q. Pan, S. A. Razavi, K. Wong, L. Huang, B. Dai, Q. Shao, G. Yu, X. Han, J. C. Rojas-Sanchez, S. Mangin, K. L. Wang, "Spin-Orbit Torque Switching of a Nearly Compensated Ferrimagnet by Topological Surface States". *Adv Mater* **31**, e1901681 (2019).

[111] A. I. Snow, "Magnetic Moment Orientation and Thermal Expansion of Antiferromagnetic CrSb". *Reviews of Modern Physics* **25**, 127-127 (1953).

[112] S. Emori, U. Bauer, S. M. Ahn, E. Martinez, G. S. Beach, "Current-driven dynamics of chiral ferromagnetic domain walls". *Nat Mater* **12**, 611-616 (2013).

[113] K. Garello, I. M. Miron, C. O. Avci, F. Freimuth, Y. Mokrousov, S. Blugel, S. Auffret, O. Boulle, G. Gaudin, P. Gambardella, "Symmetry and magnitude of spin-orbit torques in ferromagnetic heterostructures". *Nat Nanotechnol* **8**, 587-593 (2013).

[114] Q. M. Shao, H. Wu, Q. J. Pan, P. Zhang, L. Pan, K. Wong, X. Y. Che, K. L. Wang, "Room Temperature Highly Efficient Topological Insulator/Mo/CoFeB Spin-Orbit Torque Memory with Perpendicular Magnetic Anisotropy". *2018 Ieee International Electron Devices Meeting (Iedm)*, 36.33.31-36.33.34 (2018).